





**ISTANBUL TECHNICAL UNIVERSITY ★ INFORMATICS INSTITUTE**

**COMPUTATIONAL SCREENING OF DUAL CATION  
AMMINE METAL BOROHYDRIDES**

**M.Sc. THESIS**

**Yusuf KIŞLAK**

**Computational Science and Engineering Department**

**Computational Science and Engineering Master Programme**

**JUNE 2015**





**COMPUTATIONAL SCREENING OF DUAL CATION  
AMMINE METAL BOROHYDRIDES**

**M.Sc. THESIS**

**Yusuf KIŞLAK  
(702111018)**

**Computational Science and Engineering Department  
Computational Science and Engineering Master Programme**

**Thesis Advisor: Assoc. Prof. Adem TEKİN**

**JUNE 2015**



**İSTANBUL TEKNİK ÜNİVERSİTESİ ★ BİLİŞİM ENSTİTÜSÜ**

**ÇİFT KATYONLU AMİN METAL BOR HİDRÜRLERİN  
HESAPLAMALI TARAMASI**

**YÜKSEK LİSANS TEZİ**

**Yusuf KIŞLAK  
(702111018)**

**Hesaplamalı Bilim ve Mühendislik Anabilim Dalı**

**Hesaplamalı Bilim ve Mühendislik Yüksek Lisans Programı**

**Tez Danışmanı: Assoc. Prof. Adem TEKİN**

**HAZİRAN 2015**



**Yusuf KIŞLAK**, a M.Sc. student of ITU Informatics Institute 702111018 successfully defended the thesis entitled “**COMPUTATIONAL SCREENING OF DUAL CATION AMMINE METAL BOROHYDRIDES**”, which he/she prepared after fulfilling the requirements specified in the associated legislations, before the jury whose signatures are below.

**Thesis Advisor :**     **Assoc. Prof. Adem TEKİN** .....  
Istanbul Technical University

**Jury Members :**     **Assoc. Prof. Adem TEKİN** .....  
Istanbul Technical University

**Assoc. Prof. Fethiye Aylin Sungur KONUKLAR** .....  
Istanbul Technical University

**Assoc. Prof. Cem SERVANTIE** .....  
Istanbul Technical University

**Date of Submission :**   **4 May 2015**

**Date of Defense :**     **4 June 2015**



*To my family,*





## **FOREWORD**

I would like to express my sincere gratitude to my advisor Assoc. Prof. Adem TEKİN for his concern, advices and encouragement during this study. This work was supported by The Scientific and Technological Research Council of Turkey (TUBITAK- 112T988). Computing resources are provided by the National Center for High Performance Computing of Turkey (UHEM), under the Grant Number 1002132012, TUBITAK ULAKBIM, High Performance and Grid Computing Center (TRUBA resources) and Informatics Institute of Istanbul Technical University.

June 2015

Yusuf KIŞLAK  
(Physicist)



## TABLE OF CONTENTS

|   | <u>Page</u>  |
|---|--------------|
| <b>FOREWORD</b> .....   | <b>ix</b>    |
| <b>TABLE OF CONTENTS</b> .....  | <b>xi</b>    |
| <b>ABBREVIATIONS</b> .....  | <b>xiii</b>  |
| <b>LIST OF TABLES</b> .....   | <b>xv</b>    |
| <b>LIST OF FIGURES</b> .....  | <b>xvii</b>  |
| <b>SUMMARY</b> .....  | <b>xxi</b>   |
| <b>ÖZET</b> .....   | <b>xxiii</b> |
| <b>1. INTRODUCTION</b> .....  | <b>1</b>     |
| 1.1 Purpose of Thesis .....   | 3            |
| 1.2 Literature Review .....   | 4            |
| 1.3 Method.....   | 6            |
| <b>2. THEORETICAL BACKGROUND</b> .....  | <b>11</b>    |
| 2.1 Density Functional Theory .....   | 11           |
| 2.1.1 Density Functional Theory: Physical Picture.....                                | 11           |
| 2.1.2 Density Functional Formalism And Derivation Of The Kohn–Sham<br>Equations ..... | 12           |
| 2.1.3 The Local Density Approximation.....  | 16           |
| 2.1.4 The Adiabatic Theorem And The Normalisation Conditions .....                    | 18           |
| 2.1.5 The Generalised Gradient Approximation .....                                    | 22           |
| 2.2 Crystal Structure Prediction .....  | 23           |
| 2.2.1 USPEX .....   | 23           |
| 2.2.2 CALYPSO .....   | 23           |
| 2.2.3 XtalOpt .....   | 24           |
| 2.2.4 GASP .....  | 24           |
| 2.2.5 CASPESA.....  | 24           |
| 2.3 Simulated Annealing .....   | 24           |
| <b>3. RESULTS AND DISCUSSION</b> .....  | <b>27</b>    |
| 3.1 Finding Model Structures .....  | 27           |
| 3.1.1 Crystal Structure Prediction for $M_1M_2(BH_4)_3(NH_3)_2$ .....                 | 27           |
| 3.1.2 Crystal Structure Prediction for $M_1M_2(BH_4)_3(NH_3)_3$ .....                 | 31           |
| 3.1.3 Crystal Structure Prediction for $M_1M_2(BH_4)_3(NH_3)_4$ .....                 | 35           |
| 3.1.4 Crystal Structure Prediction for $M_1M_2(BH_4)_3(NH_3)_5$ .....                 | 36           |
| 3.1.5 Crystal Structure Prediction for $M_1M_2(BH_4)_3(NH_3)_6$ .....                 | 38           |
| 3.1.6 Crystal Structure Prediction for $M_1M_2(BH_4)_5(NH_3)_2$ .....                 | 40           |
| 3.1.7 Crystal Structure Prediction for $M_1M_2(BH_4)_5(NH_3)_3$ .....                 | 43           |

|  |           |
|--|-----------|
| 3.1.8 Crystal Structure Prediction for $M_1M_2(BH_4)_5(NH_3)_4$ .....  | 45        |
| 3.1.9 Crystal Structure Prediction for $M_1M_2(BH_4)_5(NH_3)_5$ .....  | 47        |
| 3.1.10 Crystal Structure Prediction for $M_1M_2(BH_4)_5(NH_3)_6$ ..... | 50        |
| 3.2 Computational Screening .....                                      | 52        |
| 3.2.1 Screening Results for $M_1M_2(BH_4)_3(NH_3)_y$ .....             | 61        |
| 3.2.2 Screening Results for $M_1M_2(BH_4)_5(NH_3)_y$ .....             | 63        |
| 3.2.3 Conclusions .....  | 68        |
| <b>REFERENCES.....</b>   | <b>71</b> |
| <b>CURRICULUM VITAE.....</b>   | <b>79</b> |

## **ABBREVIATIONS**

|            |                                      |
|------------|--------------------------------------|
| <b>AMB</b> | : Ammine Metal Borohydride           |
| <b>DFT</b> | : Density Functional Theory          |
| <b>CSP</b> | : Crystal Structure Prediction       |
| <b>DOE</b> | : Department of Energy               |
| <b>LDA</b> | : Local Density Approximation        |
| <b>GGA</b> | : Generalised Gradient Approximation |



## LIST OF TABLES

|   | <u>Page</u> |
|---|-------------|
| <b>Table 1.1</b> : Hydrogen capacity, hydrogen purity, decomposition temperature, and main impurity of $\text{Al}(\text{BH}_4)_3(\text{NH}_3)_4$ , $\text{Al}(\text{BH}_4)_3(\text{NH}_3)_3$ and $\text{Al}(\text{BH}_4)_3(\text{NH}_3)_4\text{-LiBH}_4$ [1]..... | 5           |
| <b>Table 3.1</b> : The cell parameters of the structures used in the study.....   | 60          |





## LIST OF FIGURES

|  | <u>Page</u> |
|--|-------------|
| <b>Figure 1.1</b> : Volumes and masses of 8 different materials that store hydrogen reversibly.....  | 2           |
| <b>Figure 1.2</b> : Trigonal bipyramidal structure of $Mg(BH_4)_3(NH_3)_2$ : top view(on left) and side view(on right). Representing colours: Mg: green, B: pink, N: blue, H: white.....     | 7           |
| <b>Figure 1.3</b> : The model used in CASPESA. Li atoms are presented with purple balls.....   | 8           |
| <b>Figure 3.1</b> : Crystal structure of $LiMg(BH_4)_3(NH_3)_2$ found by Sun et. al. [2].....  | 28          |
| <b>Figure 3.2</b> : Two crystal structures found by CASPESA. B3N2_1, B3N2_3 and the coordination around Li atoms are shown at the left and right sides, respectively.....                    | 29          |
| <b>Figure 3.3</b> : On the left crystal structure and Li coordination of B3N2_2 (symmetry no: 174), and on the right crystal structure and Li coordination in B3N2_4 (symmetry no: 176)..... | 30          |
| <b>Figure 3.4</b> : Crystal structure and Li coordination in B3N2_14 (symmetry no: 1) (on the left), and B3N2_18 (symmetry no: 1) (on the right). ....                                       | 32          |
| <b>Figure 3.5</b> : 8 different coordination model for $M_1M_2(BH_4)_3(NH_3)_3$ system. ....   | 33          |
| <b>Figure 3.6</b> : Some template structures for screening $M_1M_2(BH_4)_3(NH_3)_3$ system. ....   | 34          |
| <b>Figure 3.7</b> : Three different coordination geometries for $M_1M_2(BH_4)_3(NH_3)_4$ . .   | 36          |
| <b>Figure 3.8</b> : Different crystal structures of $M_1M_2(BH_4)_3(NH_3)_4$ found by CASPESA. ....  | 37          |
| <b>Figure 3.9</b> : Coordination model for $M_1M_2(BH_4)_3(NH_3)_5$ . ....   | 38          |
| <b>Figure 3.10</b> : Different crystal structures of $M_1M_2(BH_4)_3(NH_3)_5$ found by CASPESA. ....   | 39          |
| <b>Figure 3.11</b> : Coordination model for $M_1M_2(BH_4)_3(NH_3)_6$ . ....  | 40          |
| <b>Figure 3.12</b> : Different crystal structures of $M_1M_2(BH_4)_3(NH_3)_6$ found by CASPESA. ....   | 41          |
| <b>Figure 3.13</b> : Three different coordination geometries for $M_1M_2(BH_4)_5(NH_3)_2$ . .  | 43          |
| <b>Figure 3.14</b> : Different crystal structures of $M_1M_2(BH_4)_5(NH_3)_2$ found by CASPESA. ....   | 44          |
| <b>Figure 3.15</b> : Different coordination models for $M_1M_2(BH_4)_5(NH_3)_3$ . ....   | 45          |
| <b>Figure 3.16</b> : Different crystal structures of $M_1M_2(BH_4)_5(NH_3)_3$ found by CASPESA. ....   | 46          |
| <b>Figure 3.17</b> : Coordination models for $M_1M_2(BH_4)_5(NH_3)_4$ . ....   | 47          |
| <b>Figure 3.18</b> : Different crystal structures of $M_1M_2(BH_4)_5(NH_3)_4$ found by CASPESA. ....   | 48          |

|   |    |
|---|----|
| <b>Figure 3.19:</b> Coordination model for $M_1M_2(BH_4)_5(NH_3)_5$ . .....   | 49 |
| <b>Figure 3.20:</b> Different crystal structures of $M_1M_2(BH_4)_5(NH_3)_5$ found by CASPESA. ....   | 51 |
| <b>Figure 3.21:</b> Coordination model for $M_1M_2(BH_4)_5(NH_3)_6$ . ....  | 52 |
| <b>Figure 3.22:</b> Different crystal structures of $M_1M_2(BH_4)_5(NH_3)_6$ found by CASPESA. ....   | 53 |
| <b>Figure 3.23:</b> Different crystal structures of $Sc(BH_4)_3(NH_3)_2$ found by CASPESA. ....   | 56 |
| <b>Figure 3.24:</b> Different crystal structures of $Zr(BH_4)_4(NH_3)_2$ found by CASPESA. ....   | 57 |
| <b>Figure 3.25:</b> The alloying energies, $\Delta E_{alloy}$ , are plotted against to the decomposition energies, $\Delta E_{decomp}$ for $M_1M_2(BH_4)_3(NH_3)_y$ $y=2,3,4,5,6$ . Representing colours: Li (Red), Na (Blue), K (Green). $NH_3$ content: $x=2$ (circle), $x=3$ (triangle), $x=4$ (square), $x=5$ (diamond) and $x=6$ (pentagon). Experimental observations: $\alpha = NaZn(BH_4)_3(NH_3)_2$ [3], $\delta = LiMg(BH_4)_3(NH_3)_2$ [2]. .... | 62 |
| <b>Figure 3.26:</b> Hydrogen capacity is plotted against to the decomposition energy for $M_1M_2(BH_4)_3(NH_3)_y$ $y=2,3,4,5,6$ . Representing colours: Li (Red), Na (Blue), K (Green). $NH_3$ content: $x=2$ (circle), $x=3$ (triangle), $x=4$ (square), $x=5$ (diamond) and $x=6$ (pentagon). ....  | 63 |
| <b>Figure 3.27:</b> The alloying energies, $\Delta E_{alloy}$ , are plotted against to $M_2$ metal species for $M_1M_2(BH_4)_3(NH_3)_y$ $y=2,3,4,5,6$ . Representing colours: Li (Red), Na (Blue), K (Green). $NH_3$ content: $x=2$ (circle), $x=3$ (triangle), $x=4$ (square), $x=5$ (diamond) and $x=6$ (pentagon). ....  | 64 |
| <b>Figure 3.28:</b> The decomposition energy, $\Delta E_{decomp}$ , is plotted against to the average Pauling electronegativity of cations. Representing colours: Li (Red), Na (Blue), K (Green). $NH_3$ content: $x=2$ (circle), $x=3$ (triangle), $x=4$ (square), $x=5$ (diamond) and $x=6$ (pentagon). ....  | 65 |
| <b>Figure 3.29:</b> The alloying energies, $\Delta E_{alloy}$ , are plotted against to the decomposition energies, $\Delta E_{decomp}$ for $M_1M_2(BH_4)_5(NH_3)_y$ $y=2,3,4,5,6$ . Representing colours: Li (Red), Na (Blue), K (Green). $NH_3$ content: $x=2$ (circle), $x=3$ (triangle), $x=4$ (square), $x=5$ (diamond) and $x=6$ (pentagon). ....  | 66 |
| <b>Figure 3.30:</b> Hydrogen capacity is plotted against to the decomposition energy for $M_1M_2(BH_4)_5(NH_3)_y$ $y=2,3,4,5,6$ . Representing colours: Li (Red), Na (Blue), K (Green). $NH_3$ content: $x=2$ (circle), $x=3$ (triangle), $x=4$ (square), $x=5$ (diamond) and $x=6$ (pentagon). ....  | 67 |
| <b>Figure 3.31:</b> The alloying energies, $\Delta E_{alloy}$ , are plotted against to $M_2$ metal species for $M_1M_2(BH_4)_5(NH_3)_y$ $y=2,3,4,5,6$ . Representing colours: Li (Red), Na (Blue), K (Green). $NH_3$ content: $x=2$ (circle), $x=3$ (triangle), $x=4$ (square), $x=5$ (diamond) and $x=6$ (pentagon). ....  | 68 |

**Figure 3.32:** The decomposition energy,  $\Delta E_{decomp}$ , is plotted against to the average Pauling electronegativity of cations. Representing colours: Li (Red), Na (Blue), K (Green).  $\text{NH}_3$  content:  $x=2$  (circle),  $x=3$  (triangle),  $x=4$  (square),  $x=5$  (diamond) and  $x=6$  (pentagon). ..... 69



## COMPUTATIONAL SCREENING OF DUAL CATION AMMINE METAL BOROHYDRIDES

### SUMMARY

Many researches are conducted to discover new energy sources. Reasons for this interest can be summarized with the accelerating depletion of conventional fossil fuels, instability of fossil fuel prices due to political reasons, harmful effects on environment and human health. Hydrogen is one of the most promising candidate for future energy source due to its high abundance on earth, high gravimetric energy density and its environment friendly nature. However, absence of a safe and efficient hydrogen storage material is one of the barriers that prevent widespread use of hydrogen as an energy carrier. Even hydrogen can be stored as in the form of gas or liquid, these mediums are not practical in everyday use. As an alternative, hydrogen can also be stored in the solid form. For this purpose, both metal borohydrides and amines are proposed due to their high gravimetric and volumetric densities. Metal borohydrides have some severe drawbacks e.g. requirement of a very high temperature for the hydrogen decomposition. Therefore, they can be mixed with amines to form ammine metal borohydrides (AMBs) which have better thermodynamics properties; on the other hand, they lead to undesirable release of harmful by-products. If a second metal is added to ammine metal borohydrides, dual cation AMBs are obtained which have been attracting interest due to their low dehydrogenation temperature, suppressed release of by-product  $\text{NH}_3$  and high gravimetric hydrogen content. However, only a few of them were synthesized up to now [2–4] and hence there is a lack of information about their crystal structures. In this study, we aim to find the most promising dual cation AMBs with the general formula of  $\text{M}_1\text{M}_2(\text{BH}_4)_x(\text{NH}_3)_y$  with  $\text{M}_1 = \text{Li, Na, K}$ ;  $\text{M}_2 = \text{Mg, Ca, Mn, Ni, Sr, Zn}$ ;  $y=2,3,4,5,6$  for  $x = 3$  and  $\text{M}_1 = \text{Li, Na, K}$ ;  $\text{M}_2 = \text{Zr, Ti, Mn, Mo, Co}$ ;  $y=2,3,4,5,6$  for  $x = 5$  using computational techniques in particular density functional theory (DFT) which has been successfully used before for similar screening studies [5]. For a DFT calculation, an input including the crystal structure of the considered system must be prepared. Since there is a little information about the crystal structures of dual cation AMBs, it is wise to apply some crystal structure prediction tools to determine their crystal structures. Here, we employed CrystAl Structure Prediction via Simulated Annealing (CASPEA) algorithm [6–11] to reveal the crystal structures of the systems mentioned above. Even these systems have a very complex alloying and decomposition routes, in our screening we assumed a few simple alloying and decomposition reactions to evaluate the complexes following the study of Hummelshøj et al. [5].



## ÇİFT KATYONLU AMİN METAL BOR HİDRÜRLERİN HESAPLAMALI TARAMASI

### ÖZET

Alternatif enerji kaynaklarının geliştirilmesi üzerine birçok araştırmalar yapılmaktadır. Alternatif enerji kaynaklarını geliştirmeye yönelik bu ilginin başlıca sebepleri şöyle sıralanabilir; fosil yakıt kaynaklarının hızla tükenmekte olması, fosil yakıtlarının çevreye ve insan sağlığına zararları, politik sebeplere bağlı olarak fosil yakıtlarının fiyatlarındaki düzensizlik. Hidrojen, geleceğin en umut vadeden alternatif enerji kaynağıdır. Hidrojen, dünyamızda bol miktarda bulunması, kütlece yüksek enerji yoğunluğu ve tamamen çevre dostu yapısı ile dikkat çekmektedir. Ancak, hidrojenin enerji kaynağı olarak kullanılabilmesi için bazı engellerin aşılması gerekmektedir. Bu engellerden en önemlisi hidrojen depolayacak elverişli bir malzemenin henüz varolmamasıdır. Hidrojen, gaz olarak bir yakıt tankında depolanabilirse de bu yöntem yüksek basınç uygulanması gerektiğinden verimsizdir, ayrıca hidrojen en küçük atom olduğundan dolayı içini doldurduğu tankın atomları arasına sızarak hem tankın malzemesini kırılğanlaştırır ve güvenlik problemi oluşturur hem de kısa sürede tankın boşalmasına neden olur. Hidrojeni sıvı halde depolamak ta mümkündür ama hidrojeni sıvı hale dönüştürebilmek için hidrojenin kritik sıcaklığı olan 30 K altındaki sıcaklıklara soğutmak gerekmektedir ki bu da bu yöntemin pratik olarak ulaşım sektöründe uygulanmasını imkansız hale getirir. Bu yöntemlerin yanında hidrojeni katı halde de depolamak mümkündür. Bu amaçla bir çok farklı malzeme üzerinde araştırmalar yapılmaktadır. Bu malzemelere örnek olarak metal hidritler [12], karbon nanotüpler [13], metal-organik sistemler [14], metal borhidritler [5, 15], amonyum boran [16] ve amid/imid sistemleri [17] verilebilir. Fakat bunların hiçbirisi FreedomCAR 2015 [18] hedeflerine ulaşamamaktadır: yüksek tersinir depolama kapasitesi (3 kWh kg<sup>-1</sup> ya da ağırlıkça % 9 hidrojen), hızlı kinetik (0.02 (g H<sub>2</sub>) s<sup>-1</sup> kW<sup>-1</sup>), iyi tersinirlik (1500 döngü), işlem sıcaklığı (-40 - 60° C), düşük fiyat (\$2 kWh<sup>-1</sup> yada \$67 (kg H<sub>2</sub>)<sup>-1</sup>), yüksek hidrojen saflığı (<1 ppm CO) ve güvenlik. Metal bor hidrürler, MBH<sub>4</sub> genel formülündedirler ve içerdikleri yüksek hidrojen miktarı sebebiyle araştırmacıların ilgisini çekmiştir fakat bu malzemeler hidrojen salınımı için yüksek bir sıcaklığa ihtiyaç duyarlar. Metal borhidrürlerin içeriğine NH<sub>3</sub> molekülü eklenmesiyle amin metal bor hidrürler (AMB) oluşur. AMBler genel olarak M<sub>1</sub>(BH<sub>4</sub>)<sub>x</sub>(NH<sub>3</sub>)<sub>y</sub> formülündedirler ve metal bor hidrürlere nisbeten daha düşük sıcaklıklarda hidrojen salınımı yaparlar fakat bu tepkime neticesinde zehirli yan ürünler olan amonyak ve borazin salınımı da yaparlar. Yakın zamanda yapılan araştırmalar neticesinde, AMBlerin içeriğine ikinci bir metal atomu dahil edildiğinde M<sub>1</sub>M<sub>2</sub>(BH<sub>4</sub>)<sub>x</sub>(NH<sub>3</sub>)<sub>y</sub> genel formülüyle gösterilebilen çift katyonlu AMBler oluşur ve bu malzemelerin hem hidrojen salınımı sıcaklığında düşüş gözlemlenmiştir hem de zehirli yan ürün salınımının önlendiği görülmüştür. Çift katyonlu AMBlere literatürde mevcut olan şu kompleksler örnek olarak verilebilir:

$\text{LiMg}(\text{BH}_4)_3(\text{NH}_3)_2$  [2],  $\text{NaZn}(\text{BH}_4)_3(\text{NH}_3)_2$  [3],  $\text{Li}_2\text{Al}(\text{BH}_4)_5(\text{NH}_3)_6$  [4]. Deneysel olarak sentezlenen bu malzemeler DOE (Department of Energy) hedeflerinin üzerinde bir depolama kapasitesine sahiptir. Çift katyonlu AMBler henüz yeni keşfedildiğinden dolayı bu komplekslerle alakalı teorik ya da deneysel olarak fazla bir bilgiye sahip değiliz. Bu araştırmada, yoğunluk fonksiyonel teori (YFT) ve benzetilmiş tavlama algoritmasına dayalı bir kristal yapı tahmin programı kullanarak çift katyonlu AMBlerin taraması yapılmıştır. Elde edilen bilgiler ile çift katyonlu AMBlerin özelliklerinin keşfedilmesi, deneysel olarak bu malzemeler ile ilgilenen araştırmacılara yol gösterilmesi amaçlanmıştır. Bu araştırmada,  $\text{M}_1\text{M}_2(\text{BH}_4)_x(\text{NH}_3)_y$  ( $\text{M}_1=\text{Li}, \text{Na}, \text{K}$  ;  $\text{M}_2=\text{Mg}, \text{Ca}, \text{Ni}, \text{Mn}, \text{Sr}, \text{Zn}$  ;  $y=2,3,4,5,6$  for  $x=3$  and  $\text{M}_1=\text{Li}, \text{Na}, \text{K}$  ;  $\text{M}_2=\text{Zr}, \text{Ti}, \text{Mn}, \text{Mo}, \text{Co}$  ;  $y=2,3,4,5,6$  for  $x=5$ ) genel formülü ile verilen çift katyonlu AMBlerin alaşım oluşturma ve bozunma enerjileri gözönüne alınarak en uygun kompleksler tespit edilmiştir. Bu araştırmadaki tarama kapsamında bulunan komplekslerin büyük bir kısmının kristal yapısı bilgisi mevcut değildir bu sebeple araştırmanın ilk adımını bu komplekslerin kristal yapılarının tahmin edilmesi oluşturmaktadır. Bir malzeme ile ilgili en önemli bilgilerden birisi o malzemenin kristal yapısıdır çünkü malzemenin neredeyse tüm fiziksel özellikleri o malzemenin kristal yapısı ile ilişkilidir. Eğer bir malzemenin kristal yapısı hakkında detaylı bilgi mevcut ise, henüz sentezlenmemiş olsa bile o malzemenin özellikleri hesaplanılabilmektedir. Bu araştırmada tarama işlemi yapılan 75 farklı kompleksin kristal yapısı tahmini, benzetilmiş tavlama algoritmasına dayalı bir kristal yapı tahmin programı olan CASPESA (CrystAl Structure PrEdiction via Simulated Annealing) kodu kullanılarak yapılmıştır. CASPESA, daha önce metal bor hidrürlerle ilgili yapılan araştırmalarda [19–23] ve metal aminlerle ilgili yapılan araştırmalarda [24,25] başarı ile uygulanmıştır. CASPESA'dan elde edilen tahmini yapılar düzlem dalga YFT ile atom koordinatları ve ağ örgüsü parametreleri eniyilenecektir. Tarama kapsamında çok fazla çeşit kompleks olduğundan ve her bir kompleksin birden fazla muhtemel kristal yapısı olduğundan her biri için CASPESA kodu uygulanmamıştır. Örneğin,  $\text{LiTi}(\text{BH}_4)_5(\text{NH}_3)_2$  için atomların birim hücrede 6 farklı organizasyonda olduğu yapılar şablon olarak kullanıldı. Alaşımlar çok farklı reaksiyonlarla elde edilebilir. Bu araştırmada, literatürde çeşitli tek ve iki metal içeren amin borhidrürlerin sentezlenmesinde kullanılan reaksiyonlar temel alınmıştır [2,26,27]. Alaşım oluşturma enerjisine benzer şekilde AMB'ler çok farklı ürünlerle (örneğin metal boritler, di- ya da dodeka boranlar, amonyak, bor nitür,  $\text{HBN}_2$  ve borazin ( $\text{HNBH}_3$ ) ve birbirinden farklı kompleks yollar izleyerek bozunup hidrojen üretebilirler. Bundan dolayı, bozunma enerjilerinin hesaplanmasında kararlı metal hidritlerin, hidrojen, amonyak ve borun oluşacağı varsayılmıştır. Alaşım oluşturma ve bozunma seçim kriterleri bu en basit hallerinde dahi ekstra kristal yapı tahminlerine ihtiyaç duymaktadır. Mesela, alaşım oluşturma enerjisi hesaplamalarında bazı tek metal içeren AMB'lerin de kristal yapıları bilinmelidir. Bu kristal yapılarından eğer literatürde bir bilgi mevcut ise bu bilgi kullanılmıştır ve literatürde bulunmayan kristal yapıları için kristal yapı tahmin yöntemi kullanılmıştır. Tarama işleminde umut vadeden kompleksler için aranan kriterler olarak alaşım oluşturma enerjisinin negatif olması ve bozunma enerjisinin de formül birim başına  $-0.6$  eV ile  $-0.2$  eV arasında olmasıdır. Tarama kapsamında incelenen çift katyonlu AMBlerden sadece  $\text{LiMg}(\text{BH}_4)_3(\text{NH}_3)_2$  ve  $\text{NaZn}(\text{BH}_4)_3(\text{NH}_3)_2$  sentezlenmiştir. Tarama sonucunda sentezlenmiş bu yapılar hedeflenen bölgede yer almışlardır.  $\text{M}_1\text{M}_2(\text{BH}_4)_3(\text{NH}_3)_y$  sistemi için Ni, Mg



ve Sr içeren alaşımlar da umut vadetmektedir.  $M_1M_2(BH_4)_5(NH_3)_y$  sistemi için tarama sonuçları  $M_1M_2(BH_4)_3(NH_3)_y$  sistemine nazaran daha fazla alaşımı potansiyel kompleks olarak göstermektedir,  $M_1M_2(BH_4)_5(NH_3)_y$  için neredeyse tüm alaşımlar hedeflenen bölgede yer almışlardır. Co metali içeren sistemlerin en düşük alaşım oluşturma enerjisine sahip olduğu görüldü, Co metalini sırasıyla Mo, Ti ve Zr metallerinin takip ettiği görülmüştür. Bu komplekslerin ağırlıkça hidrojen kapasiteleri incelendiğinde hepsinin de DOE 2015 hedefi olan %9'un üzerinde olduğu görülmüştür. Ağırlıkça en yüksek kapasiteye LiTi ( 16.5 wt % H) ve LiCo ( 15.5 wt % H) içeren kompleksler sahiptir. Tüm  $M_2$  metalleri içeren kompleksler için  $NH_3$  içeriği arttıkça bozunma enerjisinin düştüğü görülmüştür. Tarama işleminden geçirilen bu komplekslerden şimdilik pek azı deneysel olarak sentezlendiği gözönüne alındığında deneysel olarak sentezlenebilecek daha pek çok çift katyonlu AMBlerin var olduğu görülmektedir. Ayrıca literatürdeki bilgilere göre [28,29] çift katyonlu bor hidrürlerde,  $M_1M_2(BH_4)_x(NH_3)_y$ , alaşımı oluşturan metallerin ortalama Pauling elektronegativitesi ile bozunma sıcaklığı arasında doğrusal bir ilişkinin olduğu belirtilmiştir. Bu araştırmada hesaplanan bozunma enerjisi ile ortalama Pauling elektronegativitesi arasındaki ilişki incelendiğinde aynı doğrusal ilişkinin çift katyonlu AMBler için de geçerli olduğu görülmüştür.



## 1. INTRODUCTION

Because of the limitation of the fossil fuel reserves (according to British Petroleum's 2007 data; we will be run out of fossil fuels after about 40 years), everybody focuses to find new renewable and ecological energy sources. At this point, it has been revealed that hydrogen can be used as an energy carrier. However, to use hydrogen for this purpose, some fundamental problems in production, storage and fuel cell must be solved. The most environmentally friendly way of producing hydrogen is the electrolyzation of water via solar energy. This can be accomplished by use of tandem cells in a cheap and suitable way [30]. For fuel cell, alkaline or polymer electrolyte membrane can be used. Among them, the most challenging problem is the storage of hydrogen and therefore it is the subject of this thesis. In fact, hydrogen can be stored in gas or liquid state, but this requires very high pressure or cryogenic temperatures. Unfortunately, this hinders the usage possibility especially in transportation sector. Alternatively, hydrogen can be also stored in solid state materials such as metal hydrides [12], carbon nanotubes [13], metal-organic frameworks [14], metal borohydrides [5, 15], ammonia borane [16] and amides/imides [17]. However, none of this materials reaches FreedomCAR 2015 [18] targets: high reversible storage capacity ( $3 \text{ kWh kg}^{-1}$  or wt 9% hydrogen), fast kinetics ( $0.02 \text{ (g H}_2\text{) s}^{-1} \text{ kW}^{-1}$ ), good reversibility (1500 cycle), suitable operation temperature ( $-40 - 60^\circ \text{ C}$ ), low price ( $\$2 \text{ kWh}^{-1}$  or  $\$67 \text{ (kg H}_2\text{)}^{-1}$ ), high hydrogen purity ( $<1 \text{ ppm CO}$ ), and safety. Methane and methanol, which are the most remarkable competitors of hydrogen, have advantageous features in terms of energy capacity and distribution infrastructure but because of the carbon they emit  $\text{CO}_2$ . In addition to hydrogen, ammonia is an alternative energy carrier in transportation sector because of its carbon free content. Ammonia is not a greenhouse gas and its high hydrogen density makes it a favourite competitor of hydrogen. Mostly, ammonia is produced from natural gas but in some countries, such as China, coal has been used for this purpose. Today, a quite developed ammonia infrastructure exists and by suppressing the release of  $\text{CO}_2$ , which is emitted

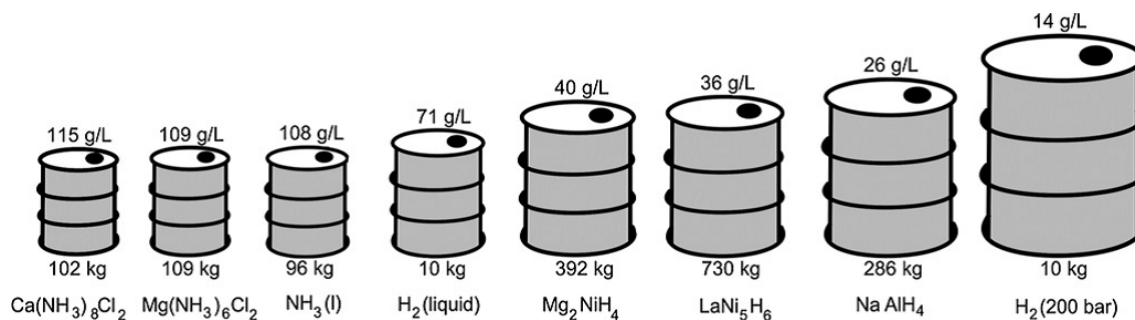


**Figure 1.1:** Volumes and masses of 8 different materials that store hydrogen reversibly.

during ammonia production from coal based plants, ammonia becomes a long term (approximately 200 years [31]), carbon free alternative instead of being a short term solution. Although a general opinion which does not recognise ammonia as a potential energy source in transportation sector because of its high toxicity, recent researches show that when ammonia is stored in metal ammines, such as  $\text{Mg}(\text{NH}_3)_6\text{Cl}_2$  [32] and  $\text{Ca}(\text{NH}_3)_8\text{Cl}_2$  [33], its toxicity becomes less than fuel, in addition to that wt 10% hydrogen capacity, practical and reversible hydrogen storage material becomes available. Before using in polymer electrolyte membrane, ammonia needs to be decomposed to nitrogen and hydrogen above 300 °C with the help of a catalyst. Absence of a suitable catalyst is the most important drawback of ammonia based transportation sector. Ammonia itself also contains wt 17.8% hydrogen and it can be directly used in internal combustion engines or it can be used as fuel in solid oxide fuel cells (SOFC). When ammonia is stored in metal ammines in the solid state, volumetric hydrogen density is higher than liquid ammonia and other metal hydrides as shown in the figure 1.1. Figure 1.1 also compares gravimetric hydrogen storage content of materials and it is clear that metal ammines are quite lighter than metal hydrides [34].

Metal borohydrides, which are composed of metal cation,  $\text{M}^+$ , and borohydride anion,  $\text{BH}_4^-$ , are ionic compounds with the general formula  $\text{M}(\text{BH}_4)_n$ . Because of the high hydrogen content, they are regarded as future hydrogen storage materials. Among these metal borohydrides, alkali metal borohydrides such as  $\text{LiBH}_4$  [35], are thermodynamically too stable, on the other hand, alkaline earth metal borohydrides [36] have very slow kinetics and they have irreversible hydrogen emission reaction in practical terms and transition metal borohydrides are either unstable or irreversible [37]. As a summary, all metal borohydrides have problematic features that prevent

them to be used for hydrogen storage purpose. However, addition of a second metal to the content of this compounds can minimize these problems. This strategy is also widely used in heterogeneous catalysis development applications. Dual cation borohydrides are investigated recently in a computational screening study, and it has been observed that some compounds that is screened in this study were experimentally synthesized before. The lightest and the highest hydrogen storage capacity compound is Ammonia borane ( $\text{NH}_3\text{BH}_3$ ) which contains both ammine and borohydride. Hydrogen capacity of ammonia borane is wt 19.6% and irreversibly released hydrogen molecule is formed from the closest two hydrogens in which one of them belongs to N-H group and the other one belongs to B-H group. Although decomposition of  $\text{NH}_3\text{BH}_3$  starts below 150 °C, to release wt 13% hydrogen,  $\text{NH}_3\text{BH}_3$  needs to be heated to approximately 500 °C to release wt 13% hydrogen [26]. When  $\text{NH}_3\text{BH}_3$  decomposes, volatile compounds such as borazine ( $(\text{HNBH})_3$ ) are also formed and they damage polymer electrolyte membrane fuel cells. These unfavourable characteristics of ammonia borane can be corrected by complexation of ammonia with metal borohydride. The general formula of this new compound is  $\text{M}(\text{BH}_4)_n(\text{NH}_3)_m$  and they are called AMB. The metal type in AMBs affects proximity of two hydrogen atoms in N-H and B-H groups, therefore dehydrogenation temperature is lowered compared to metal borohydrides. Ammonia content in AMBs also affect dehydrogenation temperature. During dehydrogenation of AMBs, ammonia and borazine can be emitted with hydrogen. Both ammonia and borazine cause to poison fuel cell, so that new compounds must be discovered that prevent emission of these toxic gases.

### 1.1 Purpose of Thesis

To add a second metal to AMB content can improve their characteristics. This new kind of materials can be represented as  $\text{M}_1\text{M}_2(\text{BH}_4)_x(\text{NH}_3)_y$ . In this study AMBs,  $\text{M}_1\text{M}_2(\text{BH}_4)_x(\text{NH}_3)_y$  with  $\text{M}_1=\text{Li, Na, K}$ ,  $\text{M}_2=\text{Mg, Ca, Ni, Mn, Sr, Zn}$ ,  $y=2, 3, 4, 5, 6$  for  $x=3$  and  $\text{M}_1=\text{Li, Na, K}$ ,  $\text{M}_2=\text{Mn, Mo, Ti, Co, Zr}$ ,  $y=2, 3, 4, 5, 6$  for  $x=5$  were investigated. AMBs attract researchers' interest not long ago and therefore theoretical and experimental information about AMBs is very limited. In this study, a

computational screening is done by using density functional theory (DFT) calculations to discover new hydrogen storage materials. Crystal structures, which is required for DFT calculations, are obtained by using a crystal structure prediction program, which is based on simulated annealing algorithm. This crystal prediction method was successfully applied for metal borohydrides [19–23] and metal ammines [24, 25]. There are 75 different AMB compounds in the search scope, because of this large quantity, several crystal structures for a certain ammonia content were found and these were used for other systems by exchanging the metal atoms. For example, firstly a few crystal structure was obtained for  $\text{LiTi}(\text{BH}_4)_5(\text{NH}_3)_2$  and then same crystal structures were used as templates for  $\text{LiMn}(\text{BH}_4)_5(\text{NH}_3)_2$  but new crystal structures are required for  $\text{LiMn}(\text{BH}_4)_5(\text{NH}_3)_3$ . After swapping metal atoms in the crystal structure, cell parameters and atom coordinates are optimized via plane wave DFT. There are lots of crystal structure possibilities for one model (e.g.  $\text{LiTi}(\text{BH}_4)_5(\text{NH}_3)_2$ ). Intuitively it is expected so, because for a simple compound like  $\text{LiBH}_4$ , tens of crystal structures were found [20]. Alloys are formed as a result of very diverse range of reactions. In this study, synthesis reactions of single and dual cation AMBs appeared in the literature were used [2, 26, 27]. Similar to alloying reactions, AMBs decompose into various products (e.g. diborane, dodecaborane, ammonia,  $\text{BN}_3$ ,  $\text{HBN}_2$ , borazine ( $\text{HNBH}_3$ )) by following various reaction pathways to emit hydrogen. Therefore, to calculate decomposition energies, it is assumed that metal hydrides, hydrogen, ammonia, BN and boron are formed after dehydrogenation reactions of each dual cation AMBs. Even for these simple assumptions, to calculate alloying and decomposition energies, additional crystal predictions are required. For example, to calculate alloying energies, crystal structures of single cation AMBs are required. For these compounds, if any information about their crystal structures exists in the literature, this information is used, if not the same crystal structure prediction method is applied to these compounds.

## 1.2 Literature Review

AMBs with molecular formula  $\text{M}_1\text{M}_2(\text{BH}_4)_x(\text{NH}_3)_y$  have recently appeared in the literature.  $\text{Al}(\text{BH}_4)_3(\text{NH}_3)_x$  ( $x < 6$ ) and  $\text{Al}(\text{BH}_4)_3(\text{NH}_3)_{x-y}\text{LiBH}_4$  ( $x < 6$  and  $y < 3$ ) were synthesized by Guo et al. [1]. Hydrogen content of these AMBs are

**Table 1.1:** Hydrogen capacity, hydrogen purity, decomposition temperature, and main impurity of  $\text{Al}(\text{BH}_4)_3(\text{NH}_3)_4$ ,  $\text{Al}(\text{BH}_4)_3(\text{NH}_3)_3$  and  $\text{Al}(\text{BH}_4)_3(\text{NH}_3)_4\text{-LiBH}_4$  [1].

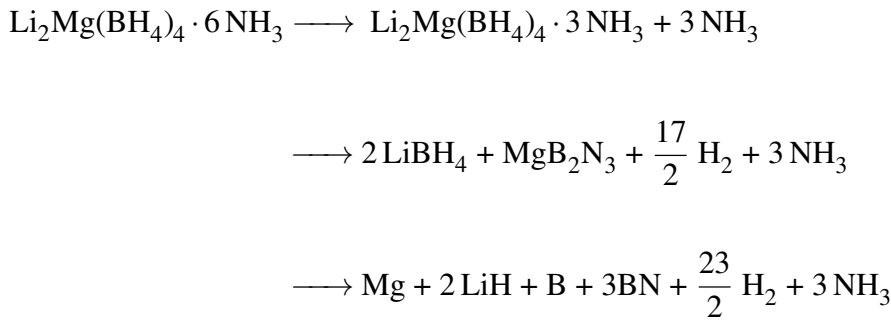
| Sample  | H <sub>2</sub> capacity (wt%) | H <sub>2</sub> purity (%) | Peak T (°C) | Main impurity          |
|---|-------------------------------|---------------------------|-------------|------------------------|
| $\text{Al}(\text{BH}_4)_3 \cdot 6 \text{NH}_3$                        | 11.8                          | 67.4                      | 168         | $\text{NH}_3$          |
| $\text{Al}(\text{BH}_4)_3 \cdot 5 \text{NH}_3$                        | 16.8                          | 90.6                      | 159         | $\text{NH}_3$          |
| $\text{Al}(\text{BH}_4)_3 \cdot 4 \text{NH}_3$                        | 15.5                          | >99                       | 128         | –                      |
| $\text{Al}(\text{BH}_4)_3 \cdot 3 \text{NH}_3$                        | 13.7                          | >99                       | 113         | –                      |
| $\text{Al}(\text{BH}_4)_3 \cdot 2 \text{NH}_3$                        | 13.7                          | 66.6                      | 108         | $\text{B}_2\text{H}_6$ |
| $\text{Al}(\text{BH}_4)_3$  | 15.5                          | 79                        | 138         | $\text{NH}_3$          |
| $6 \text{NH}_3\text{-}2 \text{LiBH}_4$                                |                               |                           |             |                        |
| $\text{Al}(\text{BH}_4)_3 \cdot 5 \text{NH}_3\text{-LiBH}_4$          | 15.4                          | 81                        | 145         | $\text{NH}_3$          |
| $\text{Al}(\text{BH}_4)_3 \cdot 5 \text{NH}_3\text{-}2 \text{LiBH}_4$ | 15.8                          | 92.4                      | 142         | $\text{NH}_3$          |
| $\text{Al}(\text{BH}_4)_3 \cdot 4 \text{NH}_3\text{-LiBH}_4$          | 16.1                          | >99                       | 109, 128    | –                      |
| $\text{Al}(\text{BH}_4)_3 \cdot 4 \text{NH}_3\text{-}2 \text{LiBH}_4$ | 14.2                          | 96.6                      | 121         | $\text{B}_2\text{H}_6$ |

between 11.8% and 16.1%, and their hydrogen purity, dehydrogenation temperatures, main impurities are shown in table 1.1. According to this table,  $\text{Al}(\text{BH}_4)_3(\text{NH}_3)_4$ ,  $\text{Al}(\text{BH}_4)_3(\text{NH}_3)_3$  and  $\text{Al}(\text{BH}_4)_3(\text{NH}_3)_4\text{-LiBH}_4$  only emit hydrogen and their maximum decomposition temperature is 128°C.

In another experimental study,  $\text{LiMg}(\text{BH}_4)_3(\text{NH}_3)_2/\text{LiBH}_4$  composite was synthesized by Sun et al. [2]. This new AMB can release wt 8% hydrogen below 200 °C. There are also hydrogen emission peaks at 388.5 °C. Emission at this temperature can be occurred due to the decomposition of  $\text{LiBH}_4$ . In fact, this temperature is below 480 °C, which is decomposition temperature of pure  $\text{LiBH}_4$ , therefore it can be considered that the synergy between  $\text{LiMg}(\text{BH}_4)_3(\text{NH}_3)_2$  and  $\text{LiBH}_4$  causes this decrease in decomposition temperature. Chu et al. [38] recently synthesized a single cation AMB  $\text{Ca}(\text{BH}_4)_2(\text{NH}_3)_2$ , and it was observed that this material releases wt 11.3% hydrogen below 250 °C. This is a good achievement when compared with 500 °C, which is the decomposition temperature of  $\text{Ca}(\text{BH}_4)_2$  to release wt 9% hydrogen. Similarly, a single cation AMB,  $\text{Mg}(\text{BH}_4)_2(\text{NH}_3)_2$  was synthesized by Soloveichik et al. [26] in 2008. This AMB contains wt 16% hydrogen. Hydrogen release starts approximately at 120 °C, and at 250 °C wt 10% hydrogen is released. This quantity is pretty good when compared with that of  $\text{Mg}(\text{BH}_4)_2$ . In fact,  $\text{Mg}(\text{BH}_4)_2$  starts hydrogen emission at 250 °C and release wt 12% hydrogen only at 400 °C. Another synthesized single cation AMB is  $\text{Y}(\text{BH}_4)_3(\text{NH}_3)_4$  which was synthesized by Yuan et al. [39]. This

AMB releases wt 8.7% hydrogen at 250 °C. At the same temperature, Y(BH<sub>4</sub>)<sub>3</sub> can release only wt 3.2% hydrogen. In 2012 Xia et al. [3] synthesized a dual cation AMB, NaZn(BH<sub>4</sub>)<sub>3</sub>(NH<sub>3</sub>)<sub>2</sub>, and it is observed that wt 7.9% hydrogen is released at 110 °C, in addition to that ammonia or diborane gases were not emitted. Li<sub>2</sub>Al(BH<sub>4</sub>)<sub>5</sub>(NH<sub>3</sub>)<sub>6</sub> was synthesized by Guo et al. [4] and it is observed that wt 10% hydrogen emitted below 120 °C with high purity (> 99%).

AMBs follow a wide variety of decomposition reaction pathways. For example, Yang et al. [27] investigated the decomposition of Li<sub>2</sub>Mg(BH<sub>4</sub>)<sub>4</sub>(NH<sub>3</sub>)<sub>6</sub> and found that the following reactions occur:



All of the experimental studies above show that single or dual cation AMBs decrease hydrogen emission temperature when compared with metal borohydrides and therefore AMBs are very suitable materials especially for automotive industry. The AMBs presented in this studies are only a few members of the AMB class and hundreds of them are waiting to be synthesized. This study aims to find out new AMBs for hydrogen storage purpose by a computational screening, which has not been done before to model them.

### 1.3 Method

The main subject of this project is to screen dual cation AMBs with the help of DFT and to find out the most suitable AMBs for hydrogen storage purpose. These AMBs are presented with a general formula of M<sub>1</sub>M<sub>2</sub>(BH<sub>4</sub>)<sub>x</sub>(NH<sub>3</sub>)<sub>y</sub> with M<sub>1</sub>=Li, Na, K, M<sub>2</sub>=Mg, Ca, Ni, Mn, Sr, Zn, y=2, 3, 4, 5, 6 for x=3 and M<sub>1</sub>=Li, Na, K, M<sub>2</sub>=Mn, Mo, Ti, Co, Zr, y=2, 3, 4, 5, 6 for x=5. Since there is very limited knowledge about crystal structures



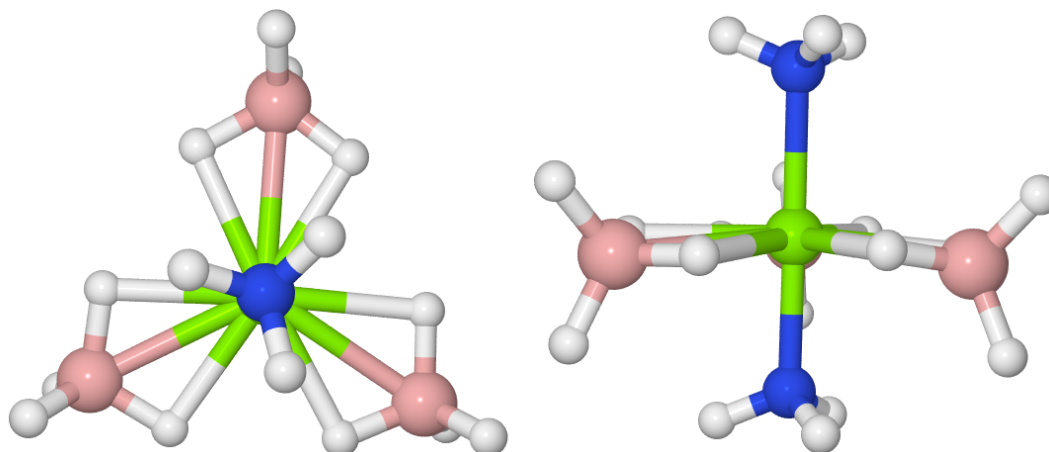


**Figure 1.2:** Trigonal bipyramidal structure of  $\text{Mg}(\text{BH}_4)_3(\text{NH}_3)_2$ : top view (on left) and side view (on right). Representing colours: Mg: green, B: pink, N: blue, H: white.

of these AMBs it is required to improve our knowledge about crystal structures before applying computational modelling. Therefore, a crystal structure prediction program, which is called CASPESA (CrystAl Structure PrEdiction via Simulated Annealing), is used. CASPESA is developed in our research group and it is successfully used before for metal amines [24, 25] and metal borohydrides [19–23]. To show how this method works, crystal structure prediction of  $\text{LiMg}(\text{BH}_4)_3(\text{NH}_3)_2$  is explained below in details. It is necessary to change model when  $\text{BH}_4$  and  $\text{NH}_3$  contents are different. Basically, CASPESA uses various bond constraints and it tries to increase the structural arrangements that makes system more stable. At this point the first thing to do is to find out factors which make AMBs more stable. Previous studies in the literature [2, 3] show that alkali metals in AMBs tend to bond with  $\text{BH}_4$  groups and alkaline earth metals or transition metals tend to bond with both of  $\text{NH}_3$  and  $\text{BH}_4$  groups. Furthermore, dihydrogen bonds between two hydrogen atoms, one from N-H group and the other one from B-H group, have an effect on the stability of the system. By considering these facts,  $\text{Mg}(\text{BH}_4)_3(\text{NH}_3)_2$  group was treated as a separate group during the CASPESA run. As seen in figure 1.2, in this trigonal bipyramidal structure, Mg atom shares a plane with three  $\text{BH}_4$  groups which are at 120 degree angles to each other (equatorial positions), and two  $\text{NH}_3$  groups are positioned above and below the plane (apical or axial positions).

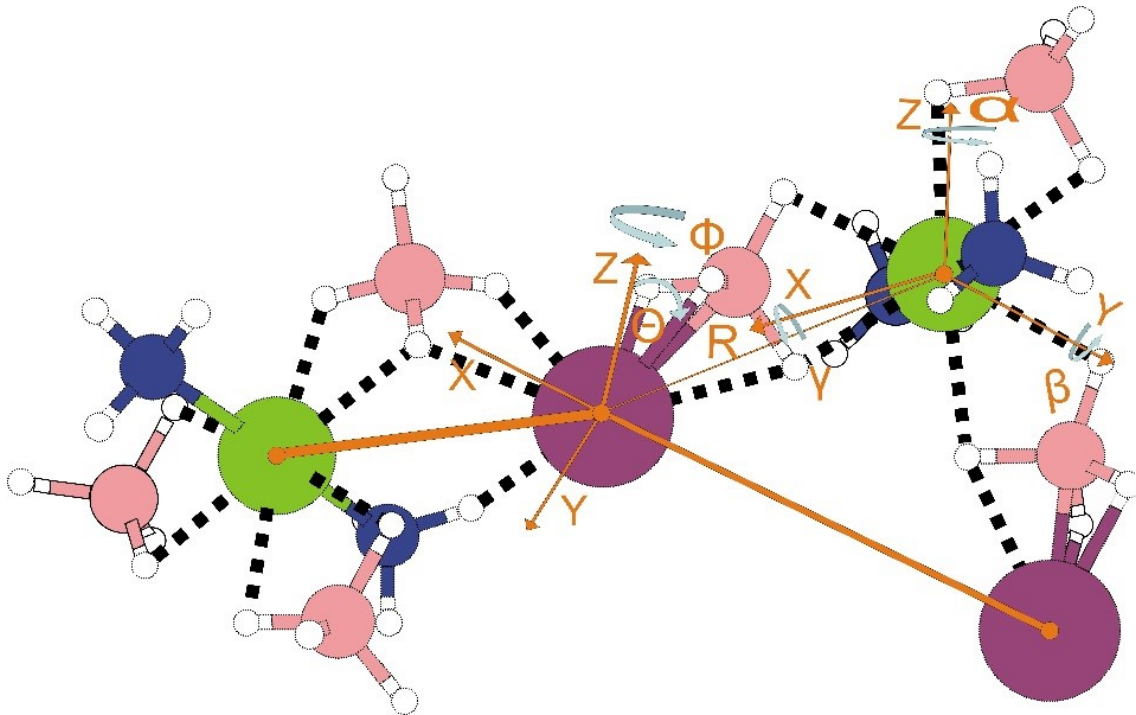


**Figure 1.3:** The model used in CASPESA. Li atoms are presented with purple balls.

In figure 1.3, unit cell which is used in CASPESA, is shown with two formula units of  $\text{LiMg}(\text{BH}_4)_3(\text{NH}_3)_2$ . In this unit cell, one of the Li atoms resides at the origin and its position is constant. Other Li atom and two  $\text{Mg}(\text{BH}_4)_3(\text{NH}_3)_2$  groups are able to change their position with the help of spherical coordinates. At the same time, two  $\text{Mg}(\text{BH}_4)_3(\text{NH}_3)_2$  groups can rotate around their own centers by using three euler angles. After the parametrization of the position of atoms in the unitcell, additional parameters are defined to describe to unit cell type (cubic, tetragonal, monoclinic, orthorhombic, rhombohedral, hexagonal, and triclinic). Without unit cell type parameters, 15 more parameters are needed, 9 of them are for positioning of Li atom and  $\text{Mg}(\text{BH}_4)_3(\text{NH}_3)_2$  groups and 6 of them are used for the rotation of  $\text{Mg}(\text{BH}_4)_3(\text{NH}_3)_2$  groups around the center atom, Mg. To define unit cell type minimum 1 parameter (for cubic) and maximum 9 parameters (for triclinic) are required. Therefore, in total there are 16-24 number of parameters to be optimized by simulated annealing method. In fact, simulated annealing is generally used for global minimization problems but in this study it is used for maximization problem and the objective function to be maximized is the structural arrangements which makes the structure more stable. As mentioned before, the interaction between Li atoms and  $\text{BH}_4$  groups causes more stable structures. Therefore, in the optimization,

number of Li-B interactions (inter-atomic distance is between 2.85 Å and 3.31 Å ) is maximized. Since any quantum mechanical calculation or any force field is not used in CASPESA, atoms can be located too close to each other leading to nonphysical situations. To prevent this situation, some minimum interatomic distances must be defined in CASPESA beforehand. Thus, Li-Li, Li-B, H-H, Li-N, and N-N minimum interatomic distances were defined respectively as follows 4.0, 2.0, 1.6, 3.0 and 4.2 Å. All these limits were set based on  $\text{LiMg}(\text{BH}_4)_3(\text{NH}_3)_2$  crystal structure found by Sun et. al. [2]. For compounds, which have higher ammonia or borohydride content, there is not any experimental information about crystal structures so DFT calculations were used to define the minimum interatomic distances. Lastly, structures produced by CASPESA were compared via DFT calculations. In the study, number of structures were 75 (3 types of alkali metal x 5 types of transition metal x 5 different ammonia content ) and for all these structures, one or more (4 in average) models were created similar to the model described above. In addition, seven unit cell types were tried for each model. If CASPESA runs 300 times for each setup, approximately 630000 crystal structures generated by CASPESA. Because of this huge number, a script was implemented for screening CASPESA outputs. Finally, DFT calculations were applied for the best CASPESA structures. We used Quantum Espresso software package for DFT calculations. The GGA exchange-correlation approximation of Perdew, Burke, Ernzerhof (PBE) [40] has been used for norm conserving pseudo potentials of all atoms. The kinetic energy and density cutoffs are set to 80 and 320 Ry, respectively. The electronic Brioullin zones were sampled with (2 x 2 x 2) k-points. The energy and force thresholds were set to  $10^{-5}$  and  $10^{-4}$  a.u, respectively.



## 2. THEORETICAL BACKGROUND

### 2.1 Density Functional Theory

Most electronic structure calculations for solids are based on density functional theory (DFT), which results from the work of Hohenberg, Kohn and Sham [41, 42]. This approach has also become popular for atoms and molecules. In the density functional theory, the electronic orbitals are solutions to a Schrödinger equation which depends on the electron density rather than on the individual electron orbitals. However, the dependence of the one-particle Hamiltonian on this density is in principle nonlocal. Often, this Hamiltonian is taken to depend on the local value of the density only – this is the local density approximation (LDA). In the vast majority of DFT electronic structure calculations for solids, this approximation is adopted. It is, however, also applied to atomic and molecular systems [43, 44].

#### 2.1.1 Density Functional Theory: Physical Picture

In density functional theory, an effective independent-particle Hamiltonian is arrived at, leading to the following Schrödinger equation for one-electron spin-orbitals:

$$\left[ -\frac{1}{2}\nabla^2 - \sum_n \frac{Z_n}{|\mathbf{r} - \mathbf{R}_n|} + \int d^3r' n(\mathbf{r}') \frac{1}{|\mathbf{r} - \mathbf{r}'|} + V_{xc}[n](\mathbf{r}) \right] \psi_k(\mathbf{r}) = \varepsilon_k \psi_k(\mathbf{r}) \quad (2.1)$$

The first three terms in the left hand side of this equation are the kinetic energy, the electrostatic interaction between the electrons and the nuclei, and the electrostatic energy of the electron in the field generated by the total electron density  $n(\mathbf{r})$ . The fourth term contains the many-body effects, lumped together in an exchange-correlation potential. The main result of density functional theory is that there exists a form of this potential, depending only on the electron density  $n(\mathbf{r})$ , that yields the exact ground state energy and density. Unfortunately, this exact form is not known, but there exist several approximations to it. The solutions of Eq.(2.1) must be

self-consistent in the density, which is given by [44]

$$\sum_{k=1}^N |\psi_k(\mathbf{r})|^2 \quad (2.2)$$

where the sum is over the  $N$  spin-orbitals  $\psi_k$  having the lowest eigenvalues  $\epsilon_k$  in (2.1), and  $N$  is the number of electrons in the system.

The total energy of the many-electron system is given by

$$E = \sum_{k=1}^N \epsilon_k - \frac{1}{2} \int d^3r d^3r' n(\mathbf{r}) \frac{1}{|\mathbf{r}-\mathbf{r}'|} n(\mathbf{r}') + E_{xc}[n] - \int d^3r V_{xc}[n](\mathbf{r}) n(\mathbf{r}) \quad (2.3)$$

where the parameters  $\epsilon_k$  are the eigenvalues occurring in Eq.(2.1) and  $E_{xc}$  is the exchange correlation energy. The exchange correlation potential  $V_{xc}[n]$  which occurs in (2.1) is the functional derivative of this energy with respect to the density:

$$V_{xc}[n](\mathbf{r}) = \frac{\delta}{\delta n(\mathbf{r})} E_{xc}[n] \quad (2.4)$$

Although the energy parameters  $\epsilon_k$  are not, strictly speaking, one-electron energies they are often treated as such for comparison with spectroscopy experiments according to an extended version of Koopman's theorem. The wave functions  $\psi_k$  also have no individual meaning but are used to construct the total charge density. This again contrasts with Hartree–Fock where the one-electron spin-orbitals have a definite interpretation: they are the constituents of the many-electron wave function [44].

Equations (2.1) and (2.2) are solved in an iterative self-consistency loop, which is started by choosing an initial density  $n(\mathbf{r})$ , constructing the Schrödinger equation (2.1) from it, solving the latter and calculating the resulting density from (2.2). Then a new Schrödinger equation is constructed and so on, until the density does not change appreciably any more [44].

### 2.1.2 Density Functional Formalism And Derivation Of The Kohn–Sham Equations

For a many-electron system, the Hamiltonian is given by

$$H = \sum_i \left[ \frac{-1}{2} \nabla_i^2 + V_{ext}(\mathbf{r}_i) \right] + \frac{1}{2} \sum_{i \neq j} \frac{1}{|\mathbf{r}_i - \mathbf{r}_j|} \quad (2.5)$$

$V_{ext}$  is an external potential which, in the systems of interest to us, is the Coulomb attraction by the static nuclei.

The ground state can be found by varying the energy-functional with respect to the wave function. Now consider carrying out this variational procedure in two stages: first – for a given electron density – minimise with respect to the wave functions consistent with this density, and then minimise with respect to the density. Denoting by  $\min_{\Psi|n}$  a minimisation with respect to the density. Denoting by  $\min_{\Psi|n}$  minimisation with respect to the wave functions  $\Psi$  which are consistent with the density  $n(\mathbf{r})$ , it can be written [44]

$$E[n] = \min_{\Psi|n} \langle \Psi | H | \Psi \rangle \quad (2.6)$$

and it will be clear that the ground state of the many-electron Hamiltonian can be found by minimising the functional  $E[n]$  with respect to the density, subject to the constraint

$$\int d^3r n(\mathbf{r}) = N \quad (2.7)$$

where  $N$  is the total number of electrons.

Now consider a separation of the Hamiltonian into the Hamiltonian  $H_0$  of the homogeneous electron gas (with external potential  $V_{ext} \equiv 0$ ), and the external potential:

$$H = H_0 + V_{ext}(\mathbf{r}) \quad (2.8)$$

In this case  $E[n]$  can be written as

$$E[n] = \min_{\Psi|n} \left[ \langle \Psi | H_0 | \Psi \rangle + \int d^3r V_{ext}(\mathbf{r}) n(\mathbf{r}) \right] \quad (2.9)$$

If the term in square brackets is minimised for a given density  $n(\mathbf{r})$ , the second term is a constant so that it does not have to be included in the minimisation:

$$E[n] = \min_{\Psi|n} [\langle \Psi | H_0 | \Psi \rangle] + \int d^3r V_{ext}(\mathbf{r}) n(\mathbf{r}) \quad (2.10)$$

writing

$$F[n] = \min_{\Psi|n} [\langle \Psi | H_0 | \Psi \rangle] \quad (2.11)$$

it is seen that  $E[n]$  can be written as

$$E[n] = F[n] + \int d^3r V_{ext}(\mathbf{r}) n(\mathbf{r}) \quad (2.12)$$

and  $F[n]$  obviously does not depend on the external potential. Now, these general statements are utilized to treat our problem of interacting electrons in an external potential. Summarising the results obtained so far, it is seen that:

- The ground state density can be obtained by minimising the energy-functional (2.6).
- If the Hamiltonian  $H$  is split into a homogeneous one,  $H_0$ , and the external potential, the energy-functional can be split into a part  $F[n]$ , which is defined in (2.11) and which is independent of the external potential, and the functional  $\int d^3r V_{ext}(\mathbf{r}) n(\mathbf{r})$

The problem with treating the many-electron system lies in the electron–electron interaction. In fact, for both interacting and noninteracting electron systems the form of the functional  $E[n]$  is unknown, but the ground state energy for noninteracting electrons can be solved for trivially, and this can be used to tackle the problem of interacting electrons. In the noninteracting case,  $E[n]$  has a kinetic contribution and a contribution from the external potential  $V_{ext}$ :

$$E[n] = T[n] + \int d^3r V_{ext}(\mathbf{r}) n(\mathbf{r}) \quad (2.13)$$

Variation of  $E$  with respect to the density leads to the following equation:

$$\frac{\delta T[n]}{\delta n(\mathbf{r})} + V_{ext}(\mathbf{r}) = \lambda n(\mathbf{r}) \quad (2.14)$$

where  $\lambda$  is the Lagrange parameter associated with the restriction of the density to yield the correct total number of electrons,  $N$ . The form of  $T[n]$  is unknown, but it is known that the ground state of the system can be written as a Slater determinant with spin-orbitals satisfying the single-particle Schrödinger equation:

$$\left[ -\frac{1}{2}\nabla^2 + V_{ext}(\mathbf{r}) \right] \psi_k(\mathbf{r}) = \epsilon_k \psi_k(\mathbf{r}) \quad (2.15)$$

The ground state density is then given by

$$n(\mathbf{r}) = \sum_{k=1}^N |\psi_k(\mathbf{r})|^2 \quad (2.16)$$

where the spin-orbitals  $\psi_k$  are supposed to be normalised so that the density satisfies the correct normalisation to the number of particles  $N$ . Using the above analysis, and taking  $T[n]$  for the functional  $F[n]$ , it is seen that the kinetic energy-functional  $T$  is independent of the potential  $V_{ext}$ . Summarising:

- The energy-functional of a noninteracting electron gas can be split into a kinetic functional  $T[n]$ , and a functional representing the interaction with the external potential,  $\int d^3r V_{ext}(\mathbf{r}) n(\mathbf{r})$ . The kinetic functional does not depend on the external potential.



- The exact solution of the noninteracting electron gas is given in terms of the eigenfunction solutions of the independent-particle Hamiltonian; see Eq. (2.15).

The energy-functional for a many-electron system with electronic interactions included can be written in the form

$$E[n] = T[n] + \int d^3r V_{ext}(\mathbf{r}) n(\mathbf{r}) + \frac{1}{2} \int d^3r \int d^3r' n(\mathbf{r}') \frac{1}{|\mathbf{r} - \mathbf{r}'|} n(\mathbf{r}) + E_{xc}[n] \quad (2.17)$$

where the last term, the exchange correlation energy, contains, by definition, all the contributions not taken into account by the first three terms which represent the kinetic energy-functional of the noninteracting electron gas, the external and the Hartree energy respectively. It is important to note that no approximations have been made so far but moved all the unknown correlations into  $E_{xc}$ , which depends on the density  $n$  rather than on the explicit form of the wave function because all the other terms in (2.17) depend on the density. For the interacting electron gas it is not clear that the kinetic energy and the electron–electron interaction can be written as a sum of two terms depending on the density only; therefore the kinetic functional for noninteracting electrons, which depends only on the density, has been split off and the remaining part of the kinetic energy has been moved into  $E_{xc}$ . Varying this equation with respect to the density, this equation is obtained [44]

$$\frac{\delta T[n]}{\delta n(\mathbf{r})} + \frac{\delta E_{xc}[n]}{\delta n(\mathbf{r})} + \int d^3r' n(\mathbf{r}') \frac{1}{|\mathbf{r} - \mathbf{r}'|} + V_{ext}(\mathbf{r}) = \lambda n(\mathbf{r}) \quad (2.18)$$

This equation has the same form as (2.14), the only difference being the potential replaced by a more complicated one, the ‘effective potential’:

$$V_{eff}(\mathbf{r}) = V(\mathbf{r}) + \frac{\delta E_{xc}[n]}{\delta n(\mathbf{r})} + \int d^3r' n(\mathbf{r}') \frac{1}{|\mathbf{r} - \mathbf{r}'|} \quad (2.19)$$

The analogue of Eq.(2.15) now becomes

$$\left[ -\frac{1}{2} \nabla^2 + V_{eff}(\mathbf{r}) \right] \psi_k(\mathbf{r}) = \varepsilon_k \psi_k(\mathbf{r}) \quad (2.20)$$

Comparing Eqs. (2.20) and (2.17), it is seen that adding the eigenvalues  $\varepsilon_k$  of the occupied states does not lead to the total energy as the Hartree energy is overestimated by a factor of 2, and there is a further difference in the exchange correlation term, so that it is obtained:

$$E = \sum_{k=1}^N \varepsilon_k - \frac{1}{2} \int d^3r \int d^3r' n(\mathbf{r}) \frac{1}{|\mathbf{r} - \mathbf{r}'|} n(\mathbf{r}') + E_{xc}[n] - \int d^3r V_{xc}[n(\mathbf{r})] n(\mathbf{r}) \quad (2.21)$$

where  $V_{xc}$  is defined in (2.4). The density functional procedure is now given by Eqs.(2.16), (2.19), (2.20) and (2.21). These equations were first derived by Kohn and Sham [42].

It has been already mentioned that the exact form of the exchange correlation potential is not known. This energy is a functional of the density, but there may be an additional explicit dependence on the external potential. Such a dependence would imply that each physical system has its own particular exchange correlation energy-functional. That the exchange correlation potential does not have such a dependence follows immediately from the argument given at the beginning of this section (Eqs. (2.8–2.12)) by separating the external potential off the Hamiltonian and taking the remaining contributions to the energy-functional for  $F[n]$ . This shows that the exact exchange correlation potential, which should work for all materials, is simply a functional of the density. In practice approximations are have to be used for  $E_{xc}$ , as the exact form of this functional is unknown, and our approximation might be better for some materials than for others. The final conclusion can then be formulated as follows [44]:

- If the energy-functional is split according to (2.17), the term  $E_{xc}[n]$  into which all the noncontrollable terms have been moved, is independent of the external potential.
- The minimisation problem of the energy-functional can be carried out using the Kohn-Sham equations (2.20) together with the constraint (2.16).

### 2.1.3 The Local Density Approximation

The exchange correlation potential is a functional derivative of the exchange correlation energy with respect to the local density and for a homogeneous electron gas which is a function of electron density. For a nonhomogeneous system, the value of the exchange correlation potential at the point  $\mathbf{r}$  depends not only on the value of the density at  $\mathbf{r}$  but also on its variation close to  $\mathbf{r}$ , and it can therefore be written as an expansion in the gradients to arbitrary order of the density [44]:

$$V_{xc}[n](\mathbf{r}) = V_{xc}[n(\mathbf{r}), \nabla n(\mathbf{r}), \nabla(\nabla n(\mathbf{r})), \dots] \quad (2.22)$$

Apart from the fact that the exact form of the energy-functional is unknown, inclusion of density gradients makes the solution of the DFT equations rather difficult, and

usually the Ansatz is made that the exchange correlation energy leads to an exchange correlation potential depending on the value of the density in  $\mathbf{r}$  only and not on its gradients – this is the local density approximation (LDA) [44]:

$$E_{xc} = \int d^3r \varepsilon_{xc}[n(\mathbf{r})] n(\mathbf{r}) \quad (2.23)$$

where  $\varepsilon_{xc}[n(r)]$  is the exchange correlation energy per particle of a homogeneous electron gas at density  $n$ . The local density approximation is exact for a homogeneous electron gas, so it works well for systems in which the electron density does not vary too rapidly. The various forms used for the exchange correlation energy density in the local density approximation,  $\varepsilon_{xc}[n(r)]$ , will be discussed and refer to the literature for more details [43, 45, 46].

The exchange effects (denoted by the subscript ‘x’) are usually included in a term based on calculations for the homogeneous electron gas [47] giving the following form for the exchange energy in density functional theory [44]:

$$\varepsilon_x[n(\mathbf{r})] = \text{Const.} \times n^{1/3}(\mathbf{r}) \quad (2.24)$$

The value for the constant is found as  $-(3/4)(3/\pi)^{1/3}$ .

For open-shell systems the spin-up and -down densities  $n_+$  and  $n_-$  are usually taken into account as two independent densities in the exchange correlation energy according to a natural extension of the DFT formalism [43]. In local density approximation (now called local spin density approximation), the exchange is given as [44]

$$E_x[n_+, n_-] = -\text{Const.} \int d^3r [n_+^{4/3}(\mathbf{r}) + n_-^{4/3}(\mathbf{r})] \quad (2.25)$$

with  $\text{Const.} = (3/2)(3/4\pi)^{1/3}$  in accordance with the closed-shell prefactor in (2.24), as can be checked by putting  $n_+ = n_- = n/2$ . As is to be expected for an exchange coupling, this expression contains interactions between parallel spin pairs only.

In addition to exchange, there is a contribution from the dynamic correlation effects (due to the Coulomb interaction between the electrons) present in the exchange correlation potential, and several local density parametrisations of this interaction have been proposed. A successful one is a parametrised version of the correlation energy obtained in quantum Monte Carlo simulations of the homogeneous electron gas at different densities [46, 48]. Other parametrisations have been presented by von

Barth and Hedin [49], and Gunnarson and Lundqvist [50]. These dynamic correlations represent couplings between both parallel and opposite spin pairs [44].

### 2.1.4 The Adiabatic Theorem And The Normalisation Conditions

In this section, the details of exchange and correlation term are given. Here, the spin will also be considered as well as spatial coordinates. All spin-space coordinates [44] ( $\mathbf{r}_1, s_1; \dots \mathbf{r}_N, s_N$ ) are denoted by  $X$ . Let us first consider the exact energy-functional (of the spin-orbitals):

$$E_{exact} = \int \Psi_{AS}^*(X) \left( -\frac{1}{2} \sum_i \nabla_i^2 + V_{ext} + V_{ee} \right) \Psi_{AS}(X) dX \quad (2.26)$$

Here,  $\Psi_{AS}(X)$  is a wave function which is antisymmetric in the  $x_i = (\mathbf{r}_i, s_i)$ , but not necessarily a Slater determinant. In below, the exact energy is compared with the Kohn–Sham functional (which should also be exact for the correct exchange-correlation functional) [44]:

$$E_{KS} = - \sum_k \int \psi_k^*(x) \frac{1}{2} \nabla_k^2 \psi_k(x) dx + \sum \int n(\mathbf{r}) V_{ext}(\mathbf{r}) dx + \frac{1}{2} \int n(\mathbf{r}) \frac{1}{|\mathbf{r} - \mathbf{r}'|} n(\mathbf{r}') d^3 r d^3 r' + E_{XC}[n] \quad (2.27)$$

The terms related to  $V_{ext}(\mathbf{r})$  are the same in both cases: the exchange and correlation term  $E_{xc}$  makes up for the difference in the kinetic energies and the difference between the exact Coulomb interaction and the Hartree approximation in the Kohn–Sham scheme [44].

Now, let's see the connection between the exact energy and Kohn-Sham formalism to pinpoint this difference better. This is done in the adiabatic connection procedure, which works as follows. First, introduce a tunable electron–electron interaction [44]

$$V_{c,\lambda} = \sum_{i,j} \frac{\lambda}{|\mathbf{r}_i - \mathbf{r}_j|} = \lambda V_c \quad (2.28)$$

where the subscript C stands for Coulomb and where  $V_c$  is identified with  $V_{c,\lambda=1}$ .

The many-body Hamiltonian is split into that of a homogeneous electron gas with interaction  $V_\lambda$  and the external potential:

$$H_\lambda = H_{0,\lambda} + \sum_i V_{ext}(\mathbf{r}_i) = (T, V_{c,\lambda}) + \sum_i V_{ext}(\mathbf{r}_i) \quad (2.29)$$

and note that for fixed densities  $n(\mathbf{r})$ , the last term will always give the same contribution to the energy. Indeed, this Hamiltonian is minimised for such a fixed

density:

$$E_\lambda[n] = \min_{\Psi|n} \langle \Psi | H_{0,\lambda} | \Psi \rangle + \int V_{ext}(\mathbf{r})n(\mathbf{r})d^3r = F_\lambda[n] + \int V_{ext}(\mathbf{r})n(\mathbf{r})d^3r \quad (2.30)$$

where the definition below has been used

$$F_\lambda[n] = \min_{\Psi|n} \langle \Psi | H_{0,\lambda} | \Psi \rangle \quad (2.31)$$

The minimisation is carried out on the set of wave functions compatible with the given densities  $n(\mathbf{r})$ .

Now, a theorem is needed that plays an important role in the quantum molecular dynamics method : the Hellmann–Feynman theorem. Here this theorem will be proved for the simple case in which a Hamiltonian depending on a single parameter  $\lambda$  is known. The theorem tells us how the energy eigenvalues of a Hamiltonian  $H_\lambda$ , depending on a parameter  $\lambda$ , vary with  $\lambda$ . [44] Differentiating the Schrödinger equation

$$H_\lambda |\psi_\lambda\rangle = E_\lambda |\psi_\lambda\rangle \quad (2.32)$$

with respect to  $\lambda$ , the equation below is obtained (the prime indicates derivative with respect to  $\lambda$ ):

$$H'_\lambda |\psi_\lambda\rangle + H_\lambda |\psi'_\lambda\rangle = E'_\lambda |\psi_\lambda\rangle + E_\lambda |\psi'_\lambda\rangle \quad (2.33)$$

Taking the inner product from the left with  $\langle \psi_\lambda |$  and using the Hermitian conjugate of (2.32), it is seen that

$$\frac{dE_\lambda}{d\lambda} = \frac{\langle \psi_\lambda | dH_\lambda / d\lambda | \psi_\lambda \rangle}{\langle \psi_\lambda | \psi_\lambda \rangle} \quad (2.34)$$

The derivative of  $F_\lambda$  can be written from the Hellmann–Feynman theorem, by realising that, since  $|\psi_\lambda\rangle$  is the variational ground state of  $F_\lambda$ , it must be the lowest eigenstate of  $H_{0,\lambda}$ . Then the equation below is obtained [44]

$$\frac{dF_\lambda}{d\lambda} = \langle \psi_\lambda | V_c | \psi_\lambda \rangle \quad (2.35)$$

From this, and from the fact that for  $\lambda = 0$  noninteracting electron gas is found

$$F_{\lambda=1}[n] = T_{KS}[n] + \int_0^1 \langle \psi_\lambda | V_c | \psi_\lambda \rangle d\lambda \quad (2.36)$$

Now the exchange correlation potential is found as the difference between the interacting and noninteracting electron gas including the Hartree energy  $E_H$ : [44]

$$E_{xc} = F_{\lambda=1}[n] - T_{KS}[n] - \sum \frac{1}{2} \int n(\mathbf{r}) \frac{1}{|\mathbf{r} - \mathbf{r}'|} n(\mathbf{r}') d^3r d^3r' = \int_0^1 \langle \psi_\lambda | V_c | \psi_\lambda \rangle d\lambda - E_H \quad (2.37)$$

The main point of the derivation is that in (2.36), which holds for the interacting gas, the kinetic energy is that of the noninteracting gas; therefore, the exchange correlation correction is found only in terms of the Coulomb interaction. For  $\lambda = 0$ , the XC correction term is nonzero as the Hartree energy does not take the antisymmetry of the full many-body wave function into account: it is the exchange-only part of the correction [44].

There is another fruitful way of looking at the exchange correlation term, which is related to the discussion in Section 2.1.2. There the probability density is considered for finding the particles 1 and 2 with coordinates  $x$  and  $x'$  respectively [44]:

$$P(x, x') = \int |\Psi(x, x', x_3, \dots, x_N)|^2 dx_3 \dots dx_N \quad (2.38)$$

Now this definition is used for a general wave function (not necessarily a Slater determinant).

The single-particle density is given as

$$n(x) = N \int |\Psi(x, x_2, \dots, x_N)|^2 dx_2 \dots dx_N \quad (2.39)$$

Integrating the single-particle density gives the number of particles:

$$\int n(x) dx = N \quad (2.40)$$

From the definition of  $n(x)$  it is immediately seen that

$$N \int P(x, x') dx' = n(x) \quad (2.41)$$

The reason for introducing these quantities is that they give insight in the exchange and correlation energies. To see this, consider the Coulomb energy: [44]

$$E_c = \frac{N(N-1)}{2} \int P(x, x') \frac{1}{|\mathbf{r} - \mathbf{r}'|} dx dx' \quad (2.42)$$

(the prefactor counts the number of particle pairs). Now the exchange correlation hole is defined,  $n_{xc}(x, x')$ , through

$$N(N - 1)P(x, x') = n(x)n(x') + n(x)n_{xc}(x, x') \quad (2.43)$$

The exchange correlation hole indicates how the actual distribution of a second electron, given a first electron at  $x$ , deviates from the average density. Then the equation below can be written [44]

$$E_c = E_H + \frac{1}{2} \int n(x)n_{xc}(x, x') \frac{1}{|\mathbf{r} - \mathbf{r}'|} dx dx' \quad (2.44)$$

Note that the second term can be identified with the exchange correlation energy. The most important consequence of this is that some properties of the exchange correlation hole can be derived, which any exchange correlation energy should satisfy. The first of these properties follows from the normalisation of  $P$ : [44]

$$\int P(x, x') dx dx' = 1 \quad (2.45)$$

which follows directly from the normalisation of the wave function. Furthermore,

$$\int n(x) dx = N \quad (2.46)$$

for the same reason. Integrating Eq. (2.43) now over  $dx'$  (this actually denotes an integration over  $\mathbf{r}'$  and a sum over  $s'$ ), the following result is obtained

$$(N - 1)n(x) = Nn(x) + n(x) \int n_{xc}(x, x') dx' \quad (2.47)$$

in other words,

$$\int n_{xc}(x, x') dx' = -1 \quad (2.48)$$

Realising that the second term in Eq. (2.44) is the exchange correlation correction to the Coulomb energy, it is seen that this correction can be described in terms of a charge distribution which carries a positive unit charge: this is the exchange correlation hole  $n_{xc}$  [44].

Let us summarise the results obtained so far. The first is that the exchange and correlation contribution to the kinetic energy can be removed from the description by applying the adiabatic connection formula. The price has to be paid is that

the Coulombic term due to exchange and correlation has to be integrated over the interaction strength  $\lambda$ . The second result is that this contribution can be described in terms of an exchange and a correlation hole, the first of which integrates up to -1 and the second integrates to 0 [44].

### **2.1.5 The Generalised Gradient Approximation**

The success of LDA can be understood now: the exchange and correlation holes are taken from very accurate quantum Monte Carlo results for the homogeneous electron gas and therefore they satisfy the two normalisation conditions for exchange and correlation just described [44].

It can also be described how a gradient expansion can be constructed: isotropy conditions must be taken into account and then make sure that the exchange and the correlation hole satisfy their respective normalisation conditions. This scheme has been carried out by several groups, and some well known functionals are those of Perdew and Wang of 1986 [51, 52] and 1991 [53] (respectively PW86 and PW91), and of Becke [54], Lee, Yang and Parr [55] (LYP) and Perdew, Burke and Enzerhof [56,57]. These exchange correlation functionals go by the name of generalised gradient approximations (GGAs) [44].

In general, GGA improves on LDA for the quantities which are already successfully treated in LDA: total energies and hence binding energies, bond lengths and angles. Ionisation energies based on Kohn–Sham energy eigenvalues are approximately the same as for LDA. In general, LDA tends to over-estimate the correlation energy and underestimates the exchange energy; these are remedied to some extent in GGA, but as the two corrections are opposite, the net effect is not too spectacular. That does not mean that the improvement is not important: the GGA gives a more accurate description of the many-body electron system than LDA citek1.

One major deficiency which is shared by GGA and LDA is the fact that the exchange correlation correction does not cancel the self-interaction present in the Hartree energy. This in particular affects the interpretation of the highest Kohn Sham energy as the ionisation energy of the system [44].



## **2.2 Crystal Structure Prediction**

Crystal structure information of a material is very important because, if the crystal structure is known many physical properties can be computationally investigated. If the crystal structure of a system is unknown, computational approaches can be used to predict the crystal structures. Crystal structure prediction (CSP) is a very active research area since the 1950s [58]. Until then, many methods have been developed including simulated annealing, evolutionary algorithms, distributed multipole analysis, random sampling, basin hopping, data mining, density functional theory and molecular mechanics [59]. Several crystal prediction codes exist and some of them are listed below.

### **2.2.1 USPEX**

USPEX (Universal Structure Predictor: Evolutionary Xtallography) is developed by Oganov et al. [60]. The USPEX code is based on an efficient evolutionary algorithm and alternative methods such as random sampling, metadynamics, corrected PSO algorithms. USPEX is interfaced with many DFT or classical codes, such as VASP, SIESTA, GULP, Quantum Espresso, CP2K, CASTEP, LAMMPS, and so on [61]. This method allows one to predict the most stable crystal structure and a number of low-energy metastable structures for a given compound at any P-T conditions without requiring any experimental input [62].

### **2.2.2 CALYPSO**

CALYPSO (Crystal structure AnaLYsis by Particle Swarm Optimization) is developed by Wang et al. to predict the energetically stable/metastable crystal structures of materials at a given chemical compositions and external conditions (e.g., pressure). The CALYPSO method is based on several major techniques (e.g. particle-swarm optimization algorithm, symmetry constraints on structural generation, bond characterization matrix on elimination of similar structures, partial random structures per generation on enhancing structural diversity, and penalty function, etc.) for global structural minimization from scratch. [62]

### **2.2.3 XtalOpt**

XtalOpt [63] is a free and truly open source evolutionary algorithm designed to predict crystal structures. It is implemented as an extension to the Avogadro molecular editor.

### **2.2.4 GASP**

The Genetic algorithm for structure prediction – GASP – is developed by Tipton et al. [64] and it predicts the structure and composition of stable and metastable phases of crystals, molecules, atomic clusters and defects from first-principles. The GASP program is interfaced to many energy codes including: VASP, LAMMPS, MOPAC, Gulp, JDFTx and can efficiently run on parallel architectures.

### **2.2.5 CASPESA**

CrystAl Structure Prediction via Simulated Annealing (CASPESA) is being developed by Adem Tekin and its details is explained in the previous chapter.

## **2.3 Simulated Annealing**

Simulated annealing is a global optimization method mimicking the process of physical annealing with solids, in which a crystalline solid is heated and then allowed to cool very slowly until it achieves its most regular possible crystal lattice configuration (i.e., its minimum lattice energy state), and thus is free of crystal defects. If the cooling schedule is sufficiently slow, the final configuration results in a solid with such superior structural integrity. Simulated annealing establishes the connection between this type of thermodynamic behaviour and the search for global minima for a discrete optimization problem. Furthermore, it provides an algorithmic means for exploiting such a connection. [65]

At each iteration of a simulated annealing algorithm applied to a discrete optimization problem, the objective function generates values for two solutions (the current solution and a newly selected solution) and these are compared. Improved solutions are always accepted, while a fraction of non-improved (inferior) solutions are accepted not to be trapped in a local minimum. The probability of accepting non-improved solutions depends on a temperature parameter, which is typically non-increasing with each

iteration of the algorithm. [65]

The key algorithmic feature of simulated annealing is that it provides a means to escape local optima by allowing hill-climbing moves (i.e., moves which worsen the objective function value). As the temperature parameter is decreased to zero, hill-climbing moves occur less frequently, and the solution distribution associated with the inhomogeneous Markov chain that models the behaviour of the algorithm converges to a form in which all the probability is concentrated on the set of globally optimal solutions (provided that the algorithm is convergent; otherwise the algorithm will converge to a local optimum, which may or not be globally optimal). [65]

Simulated annealing is outlined in the following pseudo-code (Eglese, 1990).

Select an initial solution  $\omega \in \Omega$

Select the temperature change counter  $k = 0$

Select a temperature cooling schedule,  $t_k$

Select an initial temperature  $T = t_0 \geq 0$

Select a repetition schedule,  $M_k$  that defines the number of iterations executed at each temperature,  $t_k$

Repeat

Set repetition counter  $m = 0$

Repeat

Generate a solution  $\omega' \in N(\omega)$

Calculate  $\Delta_{\omega, \omega'} = f(\omega') - f(\omega)$

If  $\Delta_{\omega, \omega'} \leq 0$ , then  $\omega \leftarrow \omega'$

If  $\Delta_{\omega, \omega'} > 0$ , then  $\omega \leftarrow \omega'$  with probability  $e^{\Delta_{\omega, \omega'} / t_k}$

$m \leftarrow m + 1$

Until  $m = M_k$

$k \leftarrow k + 1$

Until stopping criterion is met

This simulated annealing formulation results in  $M_0 + M_1 + \dots + M_k$  total iterations being executed, where  $k$  corresponds to the value for  $t_k$  at which the stopping criteria is met. In addition, if  $M_k = 1$  for all  $k$ , then the temperature changes at each iteration. [65]



### 3. RESULTS AND DISCUSSION

#### 3.1 Finding Model Structures

The first step of the study is to find model structures which are used in the screening process. There are ten different complexes with various  $\text{BH}_4$  and  $\text{NH}_3$  contents, For an AMB complex which is in the form  $\text{M}_1\text{M}_2(\text{BH}_4)_x(\text{NH}_3)_y$   $x=3, 5$   $y=2, 3, 4, 5, 6$ . Crystal structures of all these different complexes were predicted by CASPESA and minimum energy crystal structures were found. Results are presented in below.

##### 3.1.1 Crystal Structure Prediction for $\text{M}_1\text{M}_2(\text{BH}_4)_3(\text{NH}_3)_2$

Sun et al. [2] reported that crystal structure of  $\text{LiMg}(\text{BH}_4)_3(\text{NH}_3)_2$  at  $50^\circ\text{C}$  is hexagonal P63 (space group 173) and cell parameters are  $a = 8.0002 \text{ \AA}$  and  $c=8.3944 \text{ \AA}$ . When they optimized this experimental structure with DFT, smaller unit cell was obtained with cell parameters  $a=7.8658 \text{ \AA}$  and  $c=8.3944 \text{ \AA}$ . This crystal structure is shown in figure 3.1. In this structure, coordination number of Mg is five, with these five neighbouring groups Mg atom form a trigonal bipyramidal geometry. In this structure, Mg atoms share a plane with three B atoms which are at  $120^\circ$  angles to each other (equatorial positions), and there are two N atoms above and below the plane (axial positions) with Mg – N distances of  $2.04 - 2.20 \text{ \AA}$  and Mg – B distances of  $2.58 \text{ \AA}$ . In this structure, Li atoms with neighbouring 6 B atoms form a distorted octahedral geometry with Li – B distances of  $2.85 \text{ \AA}$  and  $3.31 \text{ \AA}$ . Here, Li atoms are separated by  $4.2 \text{ \AA}$ . In the experimental structure,  $\text{Li}(\text{BH}_4)_6$  groups are parallel to [001] plane forms a chain. In particular, each Li shares its 3  $\text{BH}_4$  groups residing in the same plane with other Li. In this structure, dihydrogen bonds,  $\text{N-H} \cdots \text{H-B}$ , are in between  $2.2 \text{ \AA} - 2.3 \text{ \AA}$ . The reason for existence of dihydrogen bonds is this, since H atoms in ammonia molecules are partially positive, and H atoms in borohydride molecules are partially negative dihydrogen bonds form. Therefore, a weak interaction occurs between these

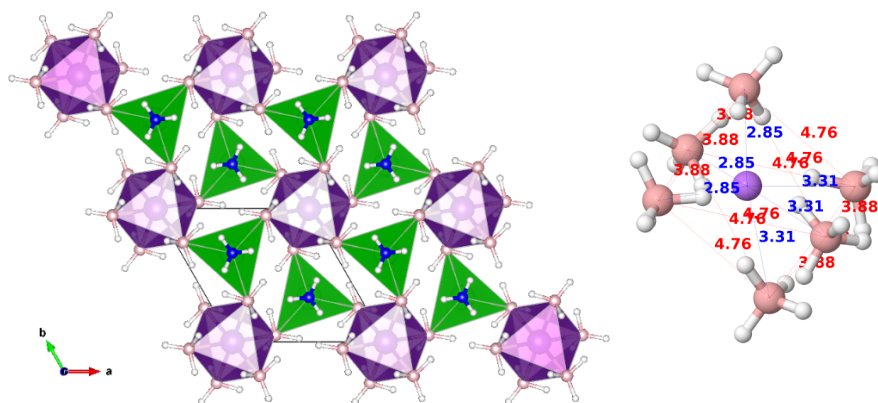


**Figure 3.1:** Crystal structure of  $\text{LiMg}(\text{BH}_4)_3(\text{NH}_3)_2$  found by Sun et. al. [2]

two H atoms. Even though, this interaction is weak, it plays a very important role in the stabilization of the structure.

20 different crystal structures were obtained by CASPESA, including the experimental crystal structure.  $M_1$  is Li in 8 of these structures, and that is K and Na for 5 and 7 of the remaining structures, respectively. Interatomic distances mentioned above vary with respect to  $M_1$  metal as expected. In the DFT relaxations of the template structures, if  $M_1$  is Li and the template was produced for  $M_1$  as Na or K, these  $M_1$  metal type was replaced with Li. Two of the structures obtained by CASPESA are shown in figure 3.2. These two structures are very similar to the experimental one. In both structures, Li atoms are parallel to [001] plane and form a chain, three  $\text{BH}_4$  groups are shared by two neighbouring Li atoms. Unit cell of B3N2\_1 is hexagonal with P63mmc (symmetry no: 194) symmetry and unit cell of B3N2\_3 is hexagonal with P63m (symmetry no: 176) symmetry. In B3N2\_1, Li–B distances are in between 3.19 Å – 3.24 Å and the octahedral coordination around Li atoms are less distorted compared to the experimental structure. Similarly, Li–B distances are between 3.15Å – 3.25Å in B3N2\_3 and the coordination around Li atoms are again less distorted octahedral compared to the experimental structure. In B3N2\_1, Mg–N distance is 2.20 Å and Mg–B distance (2.58 Å) is equal to the distance in the experimental structure. Mg–N and Mg–B distances are 2.19 Å and 2.59 Å respectively in B3N2\_3. In both structures, Li–Li distances are equal to the Li–Li distances (4.20 Å) in the experimental structure. In B3N2\_3, the minimum dihydrogen bond length is 2.80 Å and it is weaker compared to the experimental structure. Same situation is observed

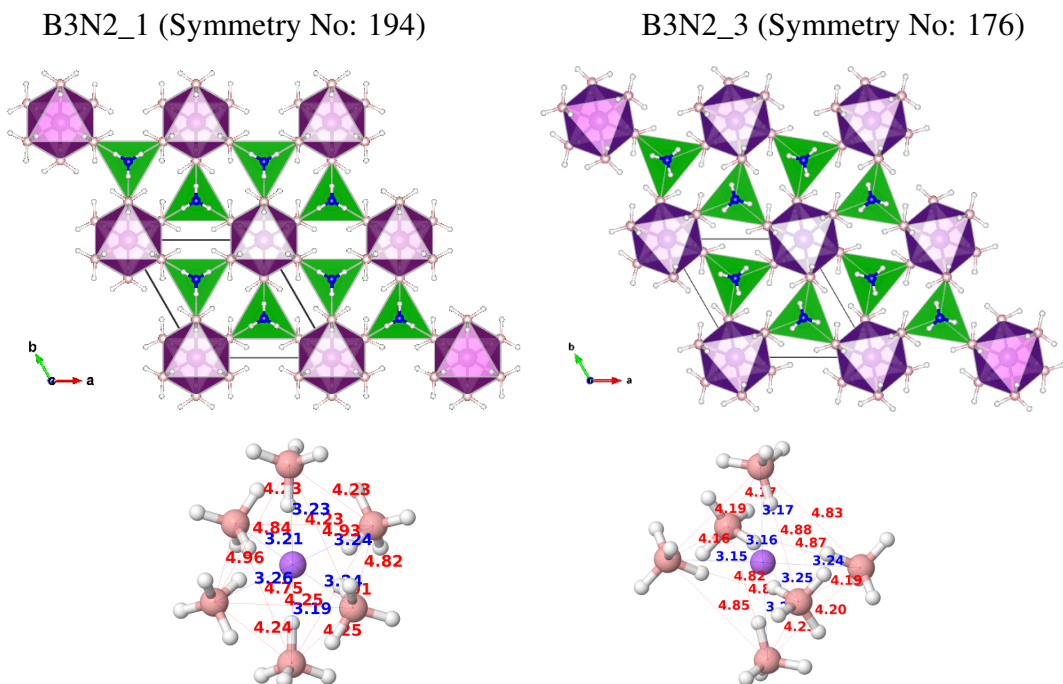


**Figure 3.2:** Two crystal structures found by CASPESA. B3N2\_1, B3N2\_3 and the coordination around Li atoms are shown at the left and right sides, respectively.

in B3N2\_1 and the minimum dihydrogen bond length is 2.77 Å. There is a similar structure to B3N2\_1 and B3N2\_3, which is B3N2\_10 and M<sub>1</sub> atom is K in this structure. Symmetry number of this structure is 1 and Mg–N, Mg–B, K–B, K–K, and N–H···H–B distances are 2.11 Å, 2.43 Å, 3.15 Å, 3.75 Å and 1.85 Å respectively.

As it can be seen, changing Li atom with K results in reduced distances of Mg–N and Mg–B and this leads to a decrease in N–H···H–B distances. N–H···H–B distance in B3N2\_10 is 1 Å shorter compared to B3N2\_1 and B3N2\_3, and it is 0.35 Å shorter compared to the experimental structure. Another structure which contains six BH<sub>4</sub> molecules around Li atom is B3N2\_12. In this structure, some of BH<sub>4</sub> groups are shared by Li atoms. CASPESA also found crystal structures which are different from the experimental structure. For example, in B3N2\_2, B3N2\_4, B3N2\_5, B3N2\_6 and B3N2\_8, coordination number of Li atoms is three, Li and three BH<sub>4</sub> groups form a trigonal planar geometry. In these structures Li atoms are layered instead of forming a chain as in B3N2\_1, B3N2\_3, B3N2\_10 and the experimental structure. Crystal structures and Li coordination of B3N2\_2 and B3N2\_4 is shown in figure 3.3. In structures shown in this figure, Li layers are parallel to [010] plane. In both structures,

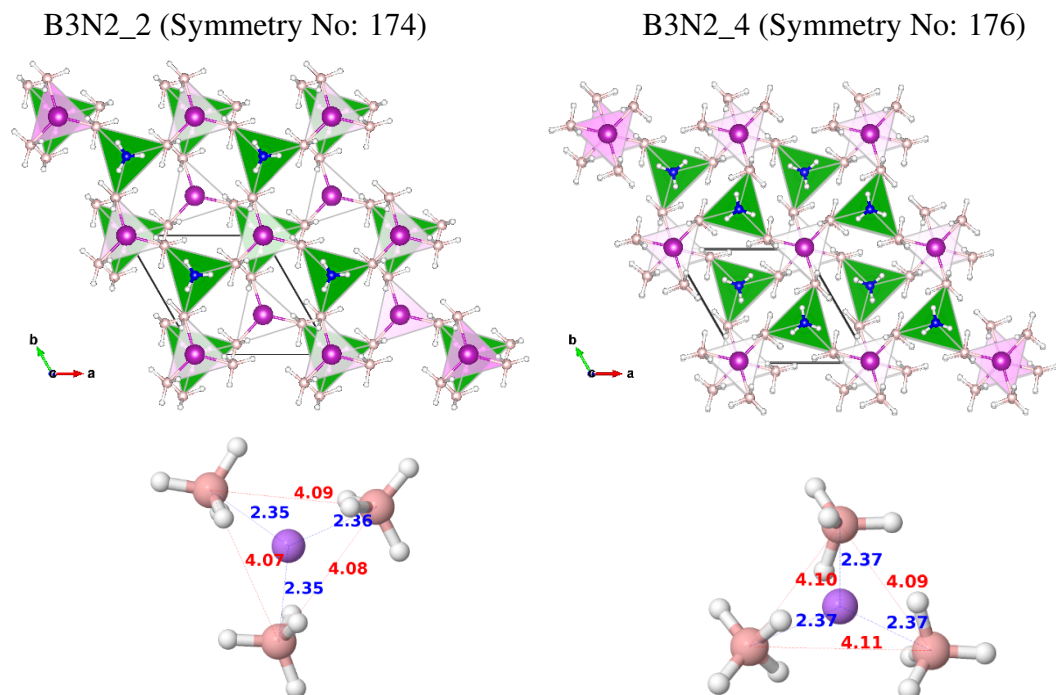


**Figure 3.3:** On the left crystal structure and Li coordination of B3N2\_2 (symmetry no: 174), and on the right crystal structure and Li coordination in B3N2\_4 (symmetry no: 176)

Li–B and B–B distances are close to each other and they are approximately 2.36 Å and 4.10 Å, respectively.

Mg–N distances are similar to other structures and they are 2.21 Å. Mg–B distance in B3N2\_2 is 2.53 Å, which is slightly longer in B3N2\_4 to be 2.56 Å. In both structures, Li–B distances are close to each other and they are approximately 2.35 Å. The minimum dihydrogen bond length is 2.76 Å and 2.66 Å for B3N2\_2 and B3N2\_4, respectively. These distances are quite long compared to the experimental structure. In one of the structure which is obtained by CASPESA, B3N2\_7, the coordination number around Li is 5. 2 of these 5 BH<sub>4</sub> molecules are shared by Li atoms which form a chain parallel to [100] plane. The minimum dihydrogen bond length in this structure is 2.51 Å. Another interesting structure is B3N2\_13. In this structure, M<sub>1</sub> atom is K and the coordination number is 7. In fact, one of these seven BH<sub>4</sub> groups is quite far from K atom (3.74 Å) and other six Li–B distances are in between 2.95 Å – 3.49 Å. In B3N2\_13, K atoms form a chain parallel to [001] plane. Similar to B3N2\_10, in this structure there are strong dihydrogen bonds, and the minimum N–H···H–B distance is 1.84 Å. In other structures obtained by CASPESA (B3N2\_9, B3N2\_11, B3N2\_14,



B3N2\_15, B3N2\_16, B3N2\_17, B3N2\_18, B3N2\_19 ve B3N2\_20),  $M_1$  atoms and  $BH_4$  groups form a tetrahedral geometry.  $M_1$  atom is Na in B3N2\_14 and B3N2\_18, and their crystal structures are shown in the figure 3.4. Tetrahedral geometry is a little distorted because of the varying Na–B distances which are in between 2.60 Å and 3.05 Å. In both of these structures Mg–N distances are approximately 2.17 Å. As a result, Mg–N distance is obtained in the following order  $d_{Mg-N}^K < d_{Mg-N}^{Na} < d_{Mg-N}^{Li}$ . Mg–B distances are different in both structures and they are 2.54 Å, 2.55 Å and 2.57 Å in B3N2\_14, 2.53 Å, 2.59 Å and 2.49 Å in B3N2\_18. The order in Mg–B distance is obtained to be  $d_{Mg-B}^K < d_{Mg-B}^{Na} < d_{Mg-B}^{Li}$ . When  $M_1$  (Li, Na, K) – B distances are considered, the following order is obtained  $d_{Na-B} < d_{K-B} < d_{Li-B}$ . In B3N2\_14 and B3N2\_18, minimum dihydrogen bond distance is 1.91 Å. The shortest dihydrogen bonds are appeared in when  $M_1=K$ , and the minimum dihydrogen bond is longer in  $M_1=Na$  compared to  $M_1=Li$ .

### 3.1.2 Crystal Structure Prediction for $M_1M_2(BH_4)_3(NH_3)_3$

To use CASPESA for crystal structure prediction, it is required to define the minimum inter-atomic distances and objective functions. For the previous system,  $M_1M_2(BH_4)_3(NH_3)_2$ , there is structural information about a complex,  $LiMg(BH_4)_3(NH_3)_2$ , in the literature and this was used at the beginning. In contrast, there is no any reported crystal structure information for  $M_1M_2(BH_4)_3(NH_3)_3$  system in the literature. Therefore, structural information used in the previous system was also employed here. As being different from the previous system, various coordinations can be formed around  $M_2$  atom as shown in the figure 3.5. For model1, a tetrahedral geometry with 3  $NH_3$  and 1  $BH_4$  is used, other 2  $BH_4$  are allowed to move independently and the objective function keeps them close to  $M_1$  atom. For model2, model3 and model5, 3  $NH_3$  groups and 2  $BH_4$  groups create a trigonal bipyramidal geometry around  $M_2$  atom and there is one free  $BH_4$  group. The main difference in these three models is the position of the groups around  $M_2$  metal. In model4,  $M_2$  atom forms an octahedral with 3  $BH_4$  and  $NH_3$  groups. In model6 and model7,  $M_2$  atom forms a trigonal prism with three  $BH_4$  and  $NH_3$  groups. In model8,  $M_2$  atom forms a capped tetrahedral geometry with three  $BH_4$  and  $NH_3$  groups.

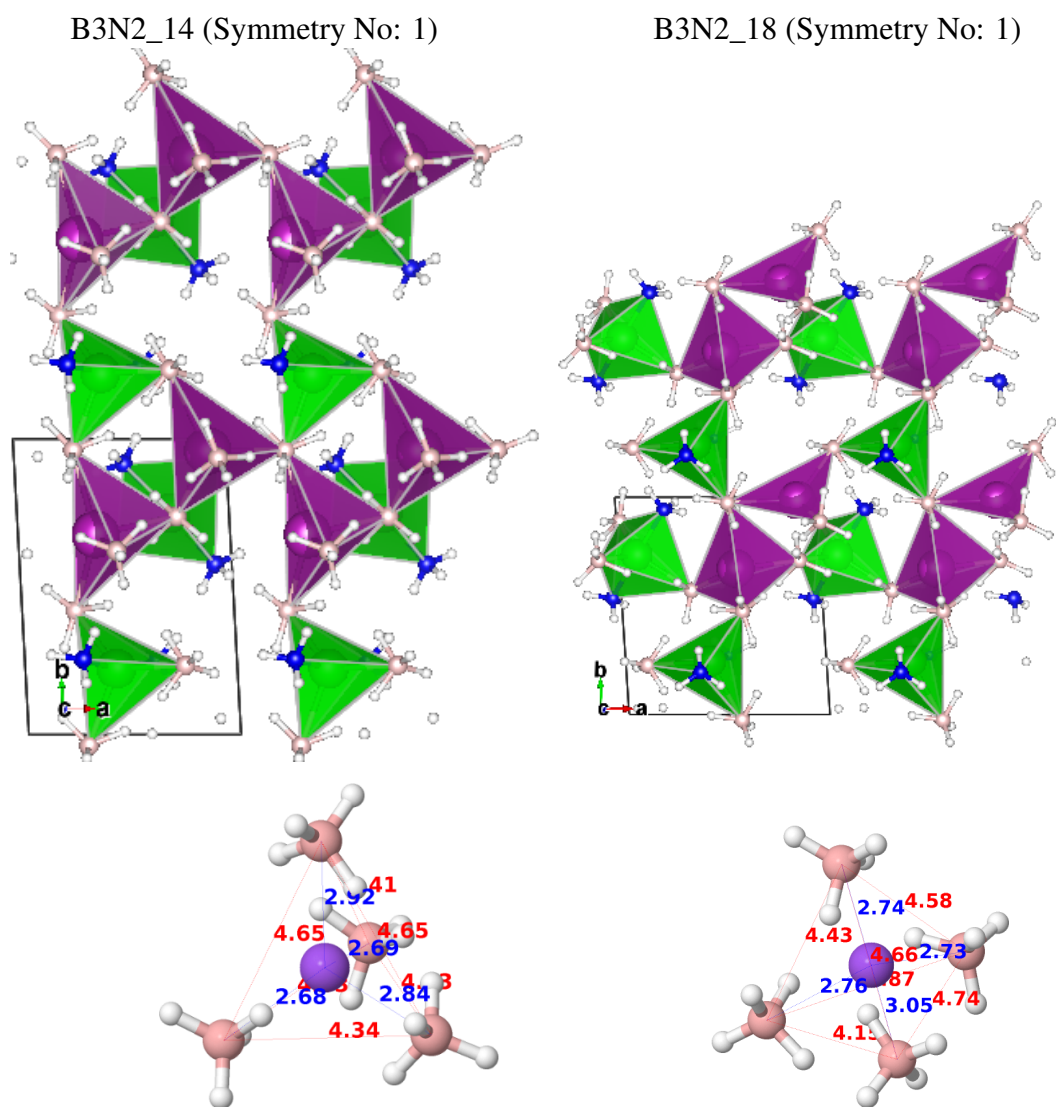


**Figure 3.4:** Crystal structure and Li coordination in B3N2\_14 (symmetry no: 1) (on the left), and B3N2\_18 (symmetry no: 1) (on the right).

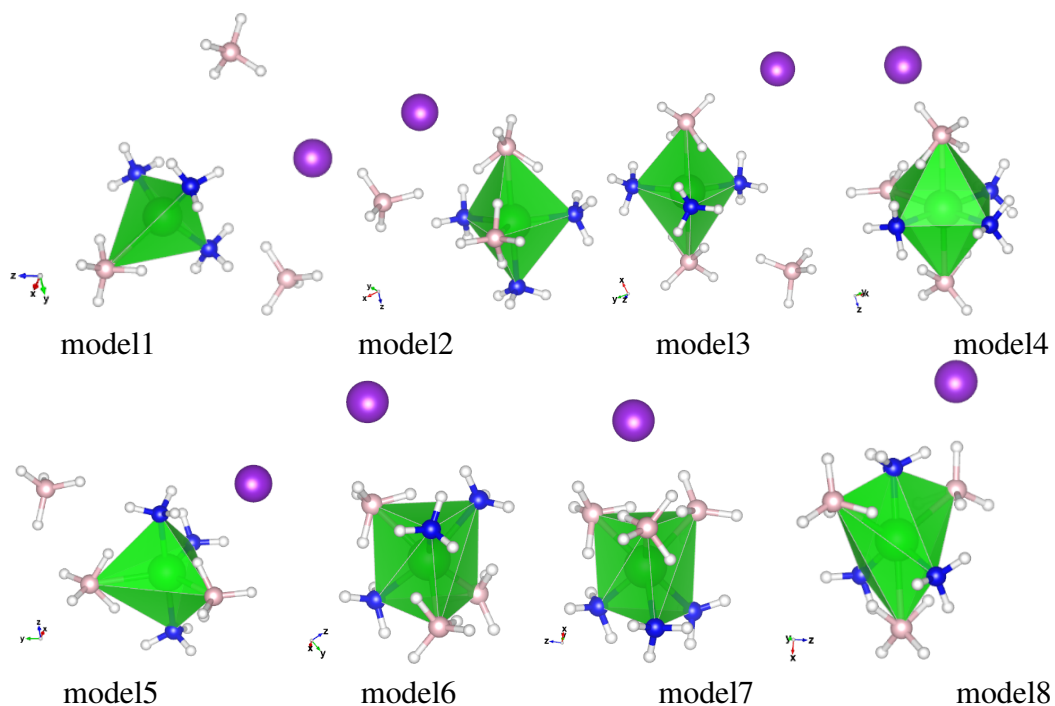


**Figure 3.5:** 8 different coordination model for  $M_1M_2(BH_4)_3(NH_3)_3$  system.

All these models were used in CASPESA to predict crystal structures, and the best results were obtained using model2, model3 and model5. Crystal structures which were obtained by using model4, model6, model7 and model8 turn into model5 after the DFT relaxation. This shows that,  $M_2$  does not prefer an octahedral arrangement. After DFT optimization, 11 crystal structures were selected as template in the screening study and some of them are shown in the figure 3.6.

In all selected structures, 2  $BH_4$  and 3  $NH_3$  groups are coordinated to  $M_2$  metal and form a trigonal bipyramidal geometry. In B3N3\_1, 3  $BH_4$  are coordinated to Li metal and form a trigonal planar geometry. Each Li atom shares a  $BH_4$  group and these Li atoms create a chain which is parallel to [001] plane. In B3N3\_4, 4  $BH_4$  groups have a tendency to be located close to Li atom and form a tetrahedral geometry and each Li atom shares 2  $BH_4$  groups and creates a chain parallel to [010] plane. In B3N3\_5, as being different from other structures, 5  $BH_4$  groups coordinated to Li atom and form a trigonal bipyramidal geometry. In this structure, each Li atom shares 3  $BH_4$  groups and a chain of Li parallel to [001] plane is formed. Similar to B3N3\_4, in B3N3\_8, 4  $BH_4$  groups are coordinated to Li atom to form a tetrahedral structure but in this structure Li atoms do not create a chain. Similar to B3N3\_5, in B3N3\_9 Li atom and 3  $BH_4$  groups constitute a trigonal planar geometry but it differs from B3N3\_5, in terms of the

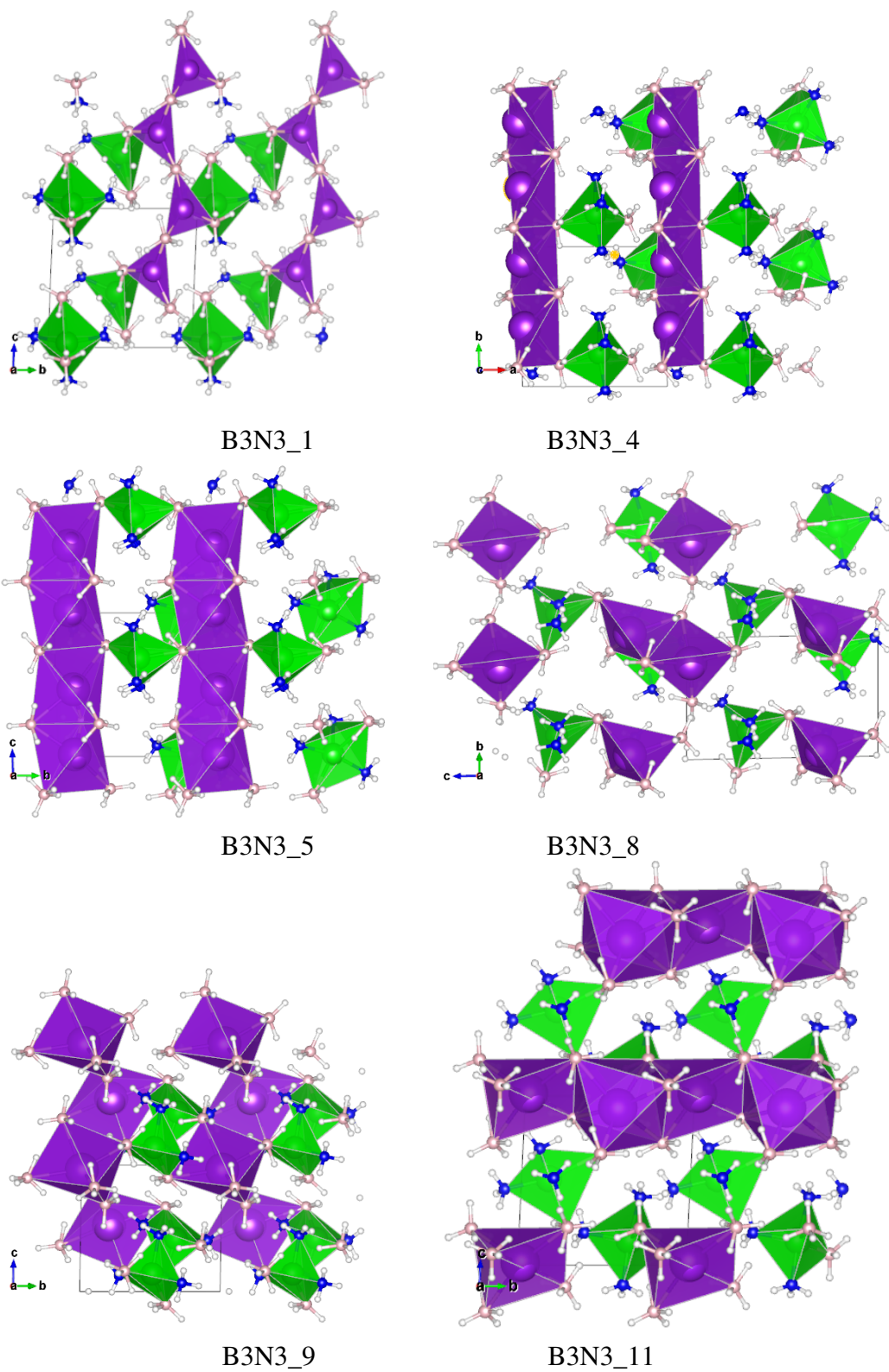


**Figure 3.6:** Some template structures for screening  $M_1M_2(BH_4)_3(NH_3)_3$  system.

number of shared  $\text{BH}_4$  groups (two in this case) and the Li chain formation parallel to [001]. In figure 3.6, the last structure B3N3\_11 is shown and it is quite different from other structures. Whereas one Li forms an octahedral arrangement with  $\text{BH}_4$  groups, the other one constitutes a distorted square pyramid. Each Li atoms shares  $\text{BH}_4$  groups and create a chain parallel to [010] plane. As a summary, 11 crystal structure with different atomic arrangements were predicted by CASPESA and these were used in the subsequent screening. Considering these 11 structures it can be said that  $\text{M}_1$  metals have a tendency to create a chain by sharing  $\text{BH}_4$  groups.

### 3.1.3 Crystal Structure Prediction for $\text{M}_1\text{M}_2(\text{BH}_4)_3(\text{NH}_3)_4$

Three similar models were used for this system and these are shown in figure 3.7. In model1 and model2,  $\text{M}_2$  metal forms an octahedral arrangement with 2  $\text{BH}_4$  and 4  $\text{NH}_3$  groups. In model1,  $\text{M}_2$  atom shares a plane with 4  $\text{NH}_3$  groups which are 90 degrees angles to each other (equatorial positions), and 2  $\text{BH}_4$  groups located above and below the plane (axial positions). In model2, 1  $\text{NH}_3$  and 1  $\text{BH}_4$  groups are in the axial position, and 2  $\text{NH}_3$  and 1  $\text{BH}_4$  groups are in the equatorial positions. Model2 is based on  $\text{Y}(\text{BH}_4)_3(\text{NH}_3)_4$  crystal structure which is discovered by Yuan et al. [39]. In this experimental structure, a  $\text{BH}_4$  group is not bound to Y atom instead it has been located close to  $\text{NH}_3$  groups to make dihydrogen bonds. The minimum bond length of these dihydrogen bonds is 2 Å. In the presence of a second metal, these independent  $\text{BH}_4$  groups bind to this second metal. In the experimental structure, the octahedral geometry is quite distorted. Y–N interatomic distances are 2.36 Å, 2.42 Å, 2.78 Å, 3.04 Å and Y–B distances are approximately 2.42 Å. In an undistorted octahedral coordination geometry, N–Y–N angle is equal to  $90^\circ$ , however in the experimental structure, one of these angles is  $119.81^\circ$ . In the last model, model3,  $\text{M}_2$  metal forms a trigonal bipyramid with 4  $\text{NH}_3$  and 1  $\text{BH}_4$  groups and there are two free  $\text{BH}_4$  groups.

By using these three models in CASPESA, 11 different crystal structures were found for  $\text{M}_1\text{M}_2(\text{BH}_4)_3(\text{NH}_3)_4$ , and some of these crystal structures are shown in the figure 3.8. In B3N4\_1, 4  $\text{NH}_3$  and 1  $\text{BH}_4$  groups bind to  $\text{M}_2$  metal to form a trigonal bipyramidal geometry. Li atom forms a tetrahedral coordination with nearby 4  $\text{BH}_4$  groups. Each Li atom shares 2  $\text{BH}_4$  groups and create a chain. In B3N4\_6, similar to

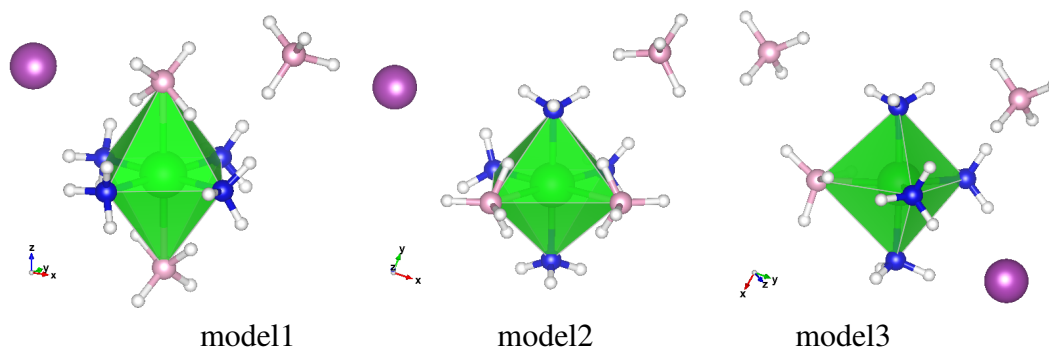


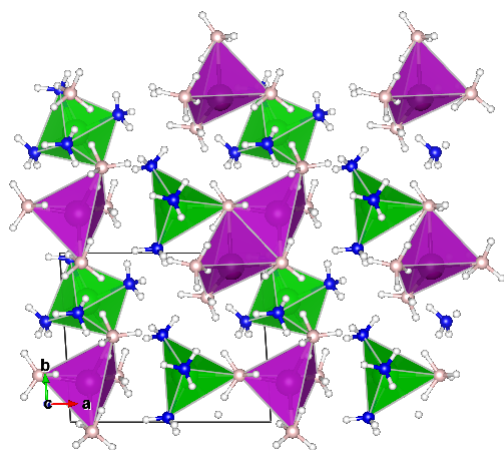
**Figure 3.7:** Three different coordination geometries for  $M_1M_2(BH_4)_3(NH_3)_4$ .

B3N4\_1, Li atoms form a tetrahedral coordination or a trigonal planar structure with the neighbouring  $BH_4$  groups. Each Li atom shares a  $BH_4$  group and create a chain which is parallel to  $[001]$  plane. In B3N4\_7, as being different from other structures,  $M_2$  metal forms an octahedral coordination with neighbouring 4  $NH_3$  and 2  $BH_4$  groups. In this structure, Li atoms form a tetrahedral coordination with neighbouring 4  $BH_4$  groups and each Li atom shares 2  $BH_4$  groups and creates a chain which is parallel to  $[001]$  plane. The most interesting structure is B3N4\_8. In this structure  $M_2$  atom forms a trigonal bipyramidal geometry. The interesting thing about this structure is that Li atom forms a tetrahedral geometry with 4  $BH_4$  groups, and each Li atom shares 2  $BH_4$  groups leading to a layer structure expanding in a and b directions. These Li layers are located in between two layers of  $M_2(BH_4)(NH_3)_4$ . This structure also contains one free  $BH_4$  group. This group which is close to 6  $NH_3$  groups and forms dihydrogen bonds with a minimum bond length of 1.89 Å. In addition, distances between Li atoms located in a and b directions are 3.42 Å, 4.85 Å, 4.60 Å and these Li atoms create a hexagon. In B3N4\_10, while  $M_2$  forms an octahedral, Li constitutes a tetrahedral or a trigonal planar coordination. Each Li atom shares a  $BH_4$  group and creates a chain. In the last structure in figure 3.8, B3N4\_11,  $M_2$  forms a trigonal bipyramidal, and Li atoms form a trigonal planar coordination. Each Li atoms create a chain parallel to  $[001]$  plane by sharing a  $BH_4$  group.

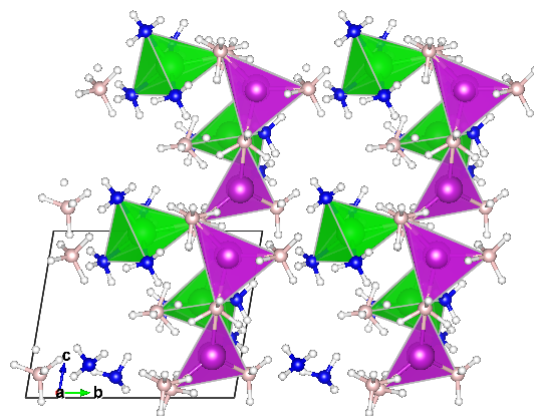
### 3.1.4 Crystal Structure Prediction for $M_1M_2(BH_4)_3(NH_3)_5$

As shown in figure 3.9, only one model was used in CASPESA to predict crystal structures of  $M_1M_2(BH_4)_3(NH_3)_5$ . In this model,  $M_2$  atom forms an octahedral orientation with 5  $NH_3$  and 1  $BH_4$  groups and there are two free  $BH_4$  groups.

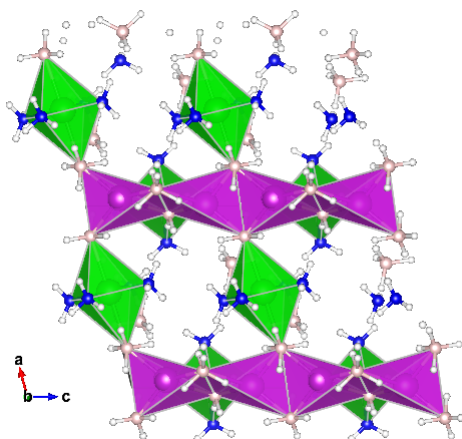




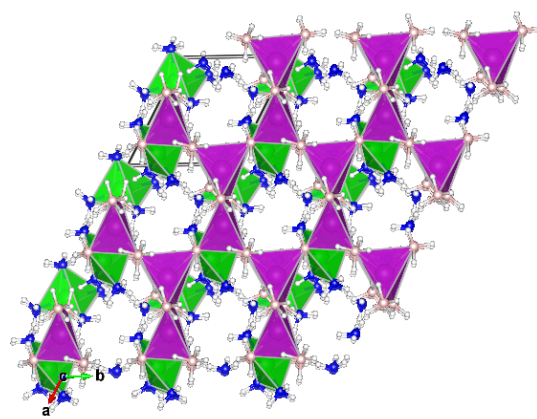
B3N4\_1



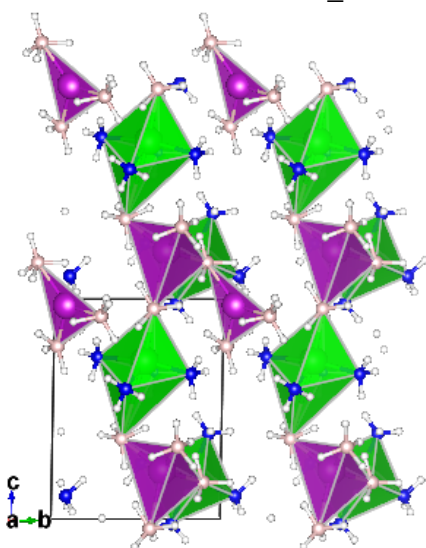
B3N4\_6



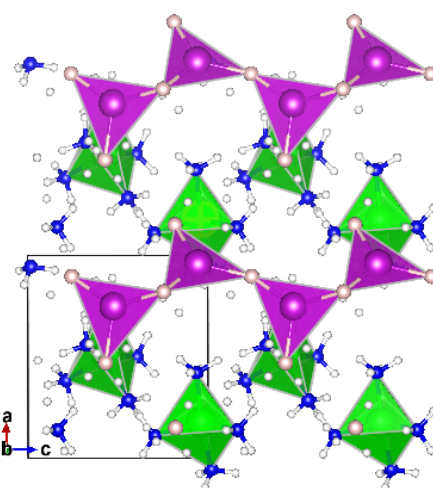
B3N4\_7



B3N4\_8



B3N4\_10



B3N4\_11

Figure 3.8: Different crystal structures of  $M_1M_2(BH_4)_3(NH_3)_4$  found by CASPESA.

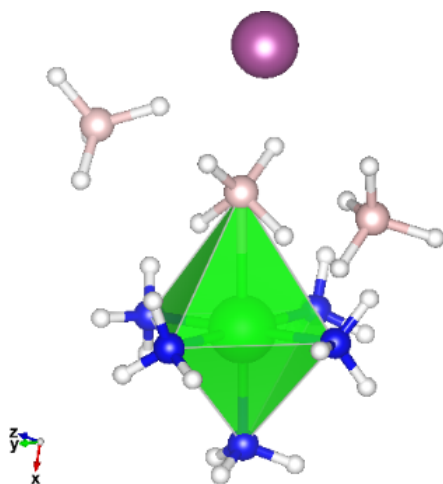
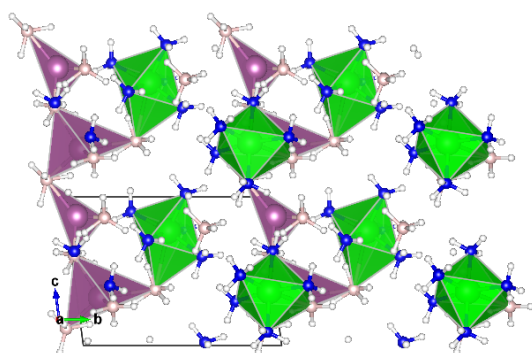


**Figure 3.9:** Coordination model for  $M_1M_2(BH_4)_3(NH_3)_5$ .

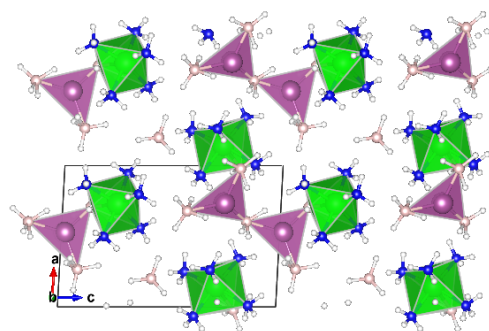
9 different crystal structures found by CASPESA and some of them are shown in the figure 3.10. Among them, the first one is B3N5\_2, in which  $M_2$  constitutes an octahedral arrangement with 5  $NH_3$  and 1  $BH_4$  groups. While some of Li atoms are surrounded by 4  $BH_4$  groups, others are surrounded by 3  $BH_4$  groups. Each Li atom shares a  $BH_4$  group which yields a chain parallel to  $[001]$  plane. In structure B3N5\_6,  $M_2$  metal forms a octahedral geometry with nearby groups and Li atom form a trigonal planar geometry with nearby  $BH_4$  groups. Even though two Li atoms share a  $BH_4$  group, there is not a chain formation. In addition, this structure contains free  $BH_4$  groups which are located close to  $NH_3$  groups to make dihydrogen bonds (the minimum one is 2 Å). In B3N5\_7,  $M_2$  forms both of an octahedral and trigonal bipyramid coordinations.  $M_2$ -N distances in trigonal bipyramidal geometry are in between 2.15 Å – 2.23 Å and this becomes 2.21 Å – 2.26 Å in the octahedral one. Coordination of Li atoms in this structure is similar to B3N5\_2, and Li atoms create a chain which is parallel to  $[100]$  plane. The last structure in figure 3.10 is B3N5\_9 in which  $M_2$  and Li prefer an octahedral and a trigonal planar coordination, respectively. Li atoms in this structure do not share any  $BH_4$  group and hence there is no chain formation.

### 3.1.5 Crystal Structure Prediction for $M_1M_2(BH_4)_3(NH_3)_6$

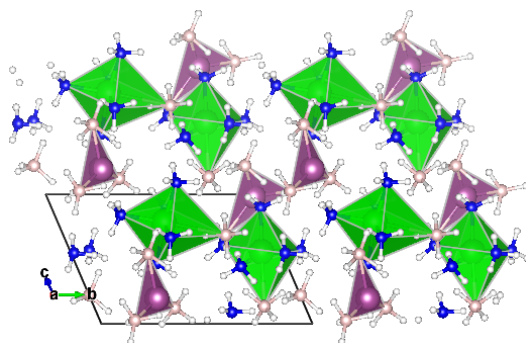




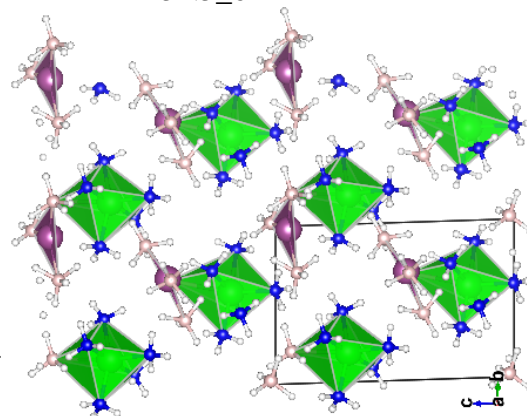
B3N5\_2



B3N5\_6



B3N5\_7



B3N5\_9

**Figure 3.10:** Different crystal structures of  $M_1M_2(BH_4)_3(NH_3)_5$  found by CASPESA.

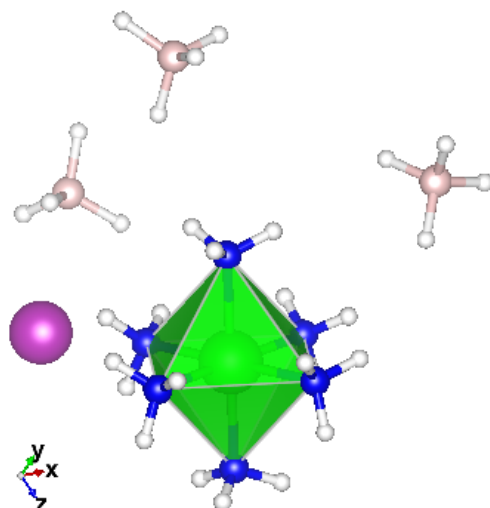


**Figure 3.11:** Coordination model for  $M_1M_2(BH_4)_3(NH_3)_6$ .

To predict crystal structure of system  $M_1M_2(BH_4)_3(NH_3)_6$ , one model shown in figure 3.11 was employed in CASPESA. In this model,  $M_2$  metal forms a octahedral geometry with nearby 6  $NH_3$  groups and the remaining 3  $BH_4$  groups move freely.

Predicted crystal structures are shown in the figure 3.12. In all these structures,  $M_2$  is surrounded by 6  $NH_3$  groups to form an octahedral geometry. The coordination of Li atom is either trigonal planar or tetrahedral in these structures. In B3N6\_1, Li atom is surrounded by 3  $BH_4$  groups and each Li atom shares a  $BH_4$  group leading to a chain which is parallel to [100] plane. Similarly, in B3N6\_2 and B3N6\_3 the coordination of Li atoms is trigonal planar but they do not share any  $BH_4$  group. In B3N6\_4, Li forms either a trigonal planar or a tetrahedral orientation which does not lead to a chain formation.

### 3.1.6 Crystal Structure Prediction for $M_1M_2(BH_4)_5(NH_3)_2$

Three different models to predict crystal structure of  $M_1M_2(BH_4)_5(NH_3)_2$  are shown in the figure 3.13. In model1,  $M_2$  metal is surrounded by 4  $BH_4$  and 2  $NH_3$  groups to form an octahedral arrangement. In this model,  $NH_3$  groups reside in the axial positions, and  $BH_4$  groups in the equatorial positions. This model also contains one free  $BH_4$  group. Model2 is similar to model1 with a difference of binding positions of  $NH_3$  and  $BH_4$  groups. In model3, there is a trigonal bipyramid around  $M_2$  atom with 3  $BH_4$  and 2  $NH_3$  groups positioned at the equatorial and axial, respectively. In addition,

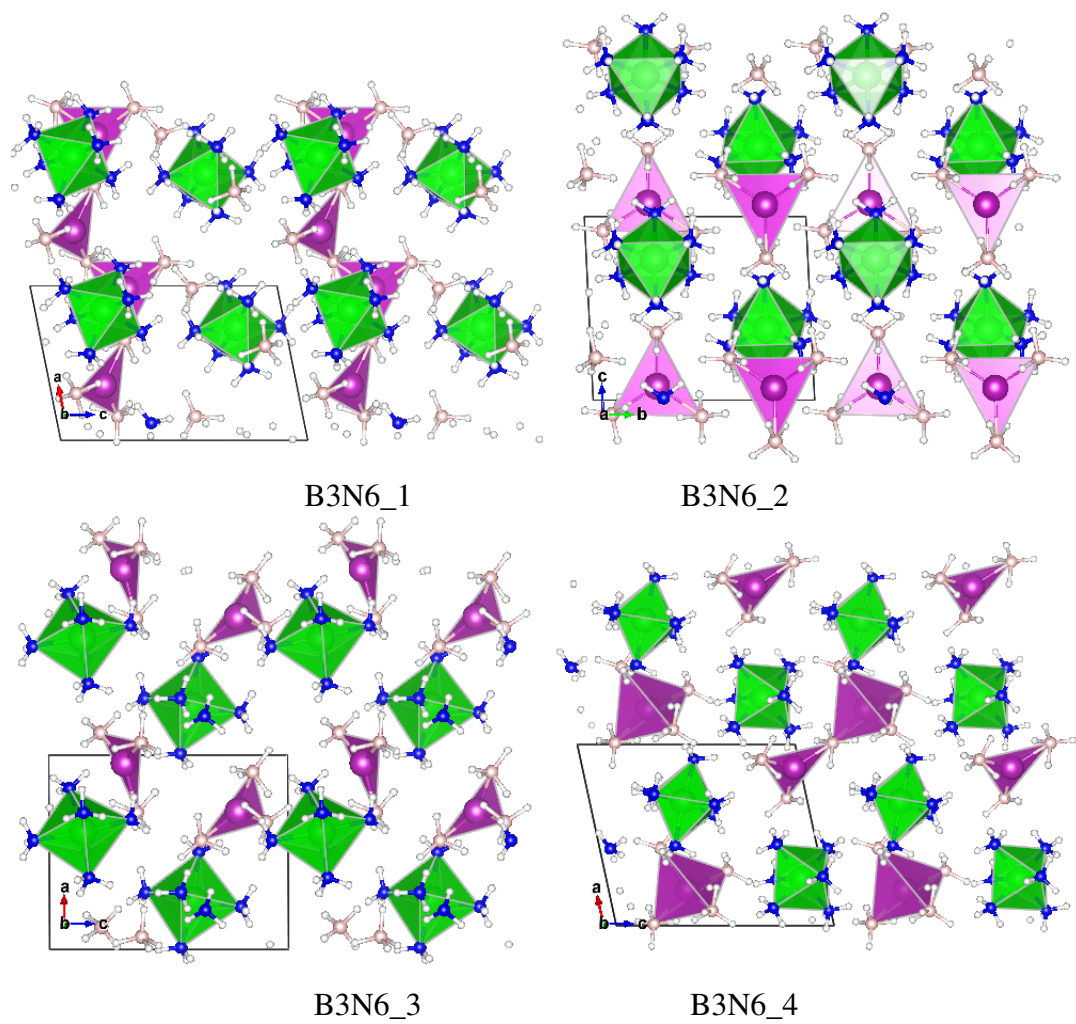


**Figure 3.12:** Different crystal structures of  $M_1M_2(BH_4)_3(NH_3)_6$  found by CASPESA.

there are two free  $\text{BH}_4$  groups in this model.

Figure 3.14 shows 8 different crystal structures obtained by CASPESA. In B5N2\_1, Li atoms constitute a trigonal planar orientation with three  $\text{BH}_4$  groups one of which is shared by two Li atoms leading to a chain formation parallel to [001] plane. Ti atom forms a distorted octahedral coordination with 4  $\text{BH}_4$  and 2  $\text{NH}_3$  groups. In this coordination, Ti–B distances are in between 2.4 Å – 2.5 Å and Ti–N distances are in between 2.2 Å – 2.3 Å. In B5N2\_2, Li atoms create a chain which is parallel to [001] plane. In this structure, one Li atom forms a trigonal planar geometry with neighbouring 3  $\text{BH}_4$  groups and other Li atom forms a tetrahedral geometry with neighbouring 4  $\text{BH}_4$  groups. Each Li atom shares a  $\text{BH}_4$  group. The coordination of Ti atom is similar to that of B5N2\_1, and it is octahedral. Ti atoms share a  $\text{BH}_4$  group with tetrahedrally coordinated Li atoms. As being different from other structures, in B5N2\_3, the coordination of Li atoms is trigonal planar and each 2 Li atoms share a  $\text{BH}_4$  group and form a short chain. These short chains are connected to each other by sharing a  $\text{BH}_4$  group in the octahedrally coordinated Ti atom. In addition to the octahedrally coordinated Ti, this structure also contains a distorted trigonal bipyramidal which is composed of 2  $\text{NH}_3$  and 3  $\text{BH}_4$  groups. This distorted trigonal bipyramid contains shorter Ti–B distances compared to the octahedrally coordinated Ti. In B5N2\_4, Li atom forms a tetrahedral coordination with 4  $\text{BH}_4$  groups and each 2 Li atoms are connected to each other by sharing a  $\text{BH}_4$  group. Similar to B5N2\_3, coordination around Ti are either octahedral or trigonal bipyramid. Ti atoms with trigonal pyramid coordination are positioned parallel to [100] plane. On the other hand, octahedrally coordinated Ti atoms share a  $\text{BH}_4$  group with short Li chains and position parallel to [100] plane. As being different from other structures, in B5N2\_5, all Ti atoms have a trigonal bipyramidal coordination and all Li atoms have a trigonal planar coordination. This structure also contains a free  $\text{BH}_4$  group. In B5N2\_6, while Ti has either an octahedral or a trigonal bipyramid coordination, Li prefers a trigonal planar arrangement. Octahedrally coordinated Ti atoms do not share any group and lay parallel to [100] plane. Two Li atoms forms a short chain by sharing a  $\text{BH}_4$  group and one of  $\text{BH}_4$  group in this chain is further shared with trigonal pyramidal coordinated Ti atom leading to a zig-zag shaped chain. In B5N2\_7, each Li atom has a trigonal planar coordination. Two Li atoms forms a short chain by sharing two  $\text{BH}_4$  groups.

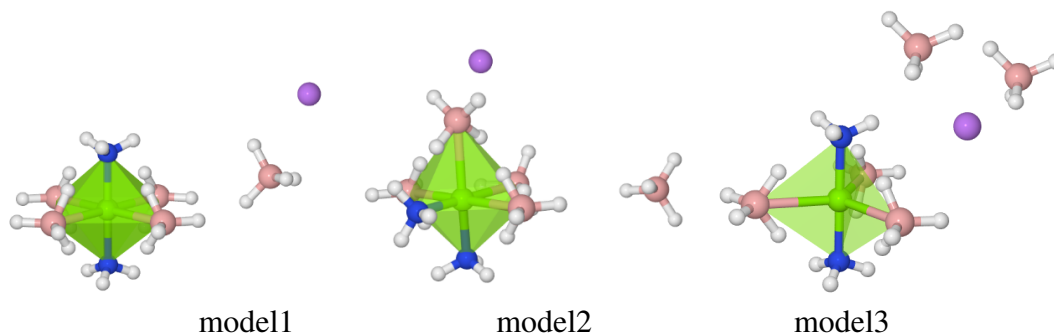


**Figure 3.13:** Three different coordination geometries for  $M_1M_2(BH_4)_5(NH_3)_2$ .

This structure also contains a Li chain which is parallel to [001] plane. In this structure the distance between closest two Li atoms is only 3 Å. Ti atoms in this structure have a trigonal bipyramidal coordination and these groups do not connect any other group but lay parallel to [001] plane. This structure also contain free  $BH_4$  groups. The last structure in figure 3.14 is B5N2\_8. The distinctive feature of this structure is that some Ti atoms forms a tetrahedral coordination geometry with 2  $NH_3$  and  $BH_4$  groups. There are also other Ti atoms having trigonal bipyramid orientation. Tetrahedrally coordinated Ti atoms do not share any groups and hence they are disconnected. In the case of Li atoms, they form both trigonal planar and distorted tetrahedral arrangements. Two Li atoms having different coordination creates a short chain by sharing a  $BH_4$  group. One of the  $BH_4$  group in this short chain is further shared with a trigonal bipyramidally coordinated Ti atom leading to chain involving three parts.

### 3.1.7 Crystal Structure Prediction for $M_1M_2(BH_4)_5(NH_3)_3$

Two different models used for  $M_1M_2(BH_4)_5(NH_3)_3$  are shown in the figure 3.15. In model1,  $M_2$  metal is surrounded by 3  $NH_3$  and  $BH_4$  groups forming an octahedral coordination. In addition, there are two free  $BH_4$  groups in this model. In model2, while  $M_2$  forms a trigonal bipyramid with  $BH_4$  groups,  $M_1$  constitutes a trigonal planar coordination with 3  $NH_3$  groups.

By using these two models in CASPESA five crystal structures shown in figure 3.16 were obtained. In B5N3\_1, coordination around  $M_2$  and bound groups to  $M_2$  are similar to model1 with  $M_2-B$  and  $M_2-N$  distances of 2.4 Å and 2.2 Å, respectively. Here, each  $M_1$  metal are surrounded by 3  $BH_4$  groups and each  $M_1$  metal shares one  $BH_4$  group to create a chain parallel to [001] plane. In B5N3\_2, while  $M_2$  forms a

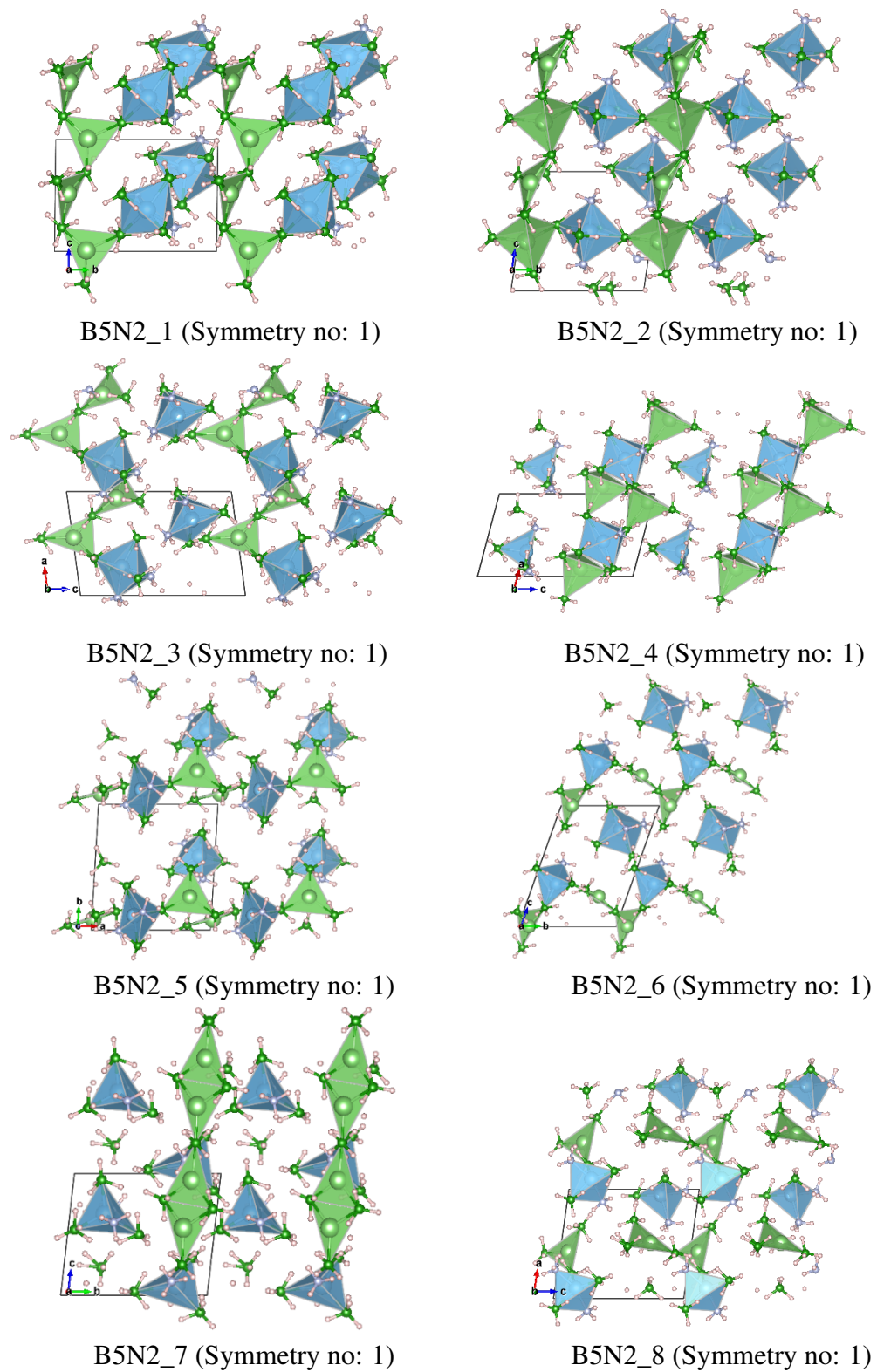


**Figure 3.14:** Different crystal structures of  $M_1M_2(BH_4)_5(NH_3)_2$  found by CASPESA.

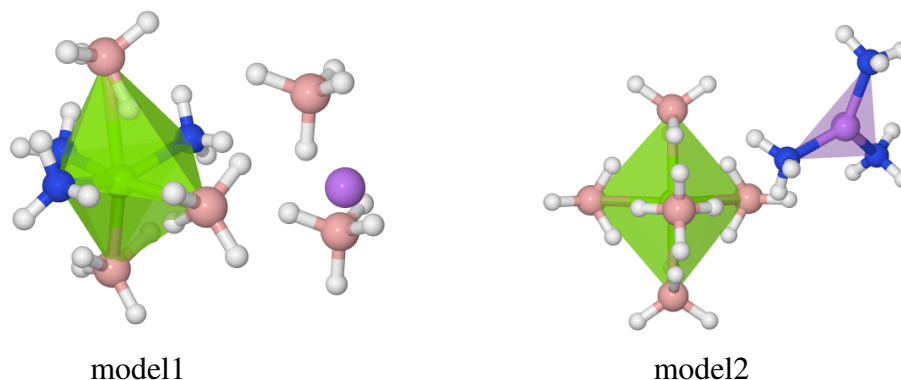


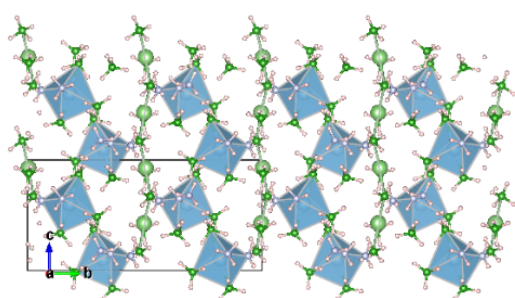
**Figure 3.15:** Different coordination models for  $M_1M_2(BH_4)_5(NH_3)_3$ .

distorted octahedral,  $M_1$  constitutes a trigonal planar orientation with neighbouring 3  $BH_4$  groups. Each two  $M_1$  metals are connected to each other by sharing 2  $BH_4$  groups. As being different from other two structures, in B5N3\_3,  $M_2$  forms a trigonal bipyramid with neighbouring 5  $BH_4$  groups. In this geometry, four  $M_2-B$  distances are in between 2.44 Å – 2.48 Å and the remaining one is 2.17 Å. Moreover,  $M_1$  forms a trigonal planar structure with three  $NH_3$  groups having  $M_1-N$  distances of 2 Å. One of each  $M_1$  metal is connected to  $M_2$  metal by sharing a  $BH_4$  group. B5N3\_4 is a similar to structure B5N3\_3. The only difference is the coordination around  $M_1$  metal: 3  $NH_3$  and 1  $BH_4$  groups form a tetrahedral geometry. B5N3\_5 is similar to the previous two structures. However, there are three  $NH_3$  molecules around  $M_1$  forming a trigonal planar orientation.

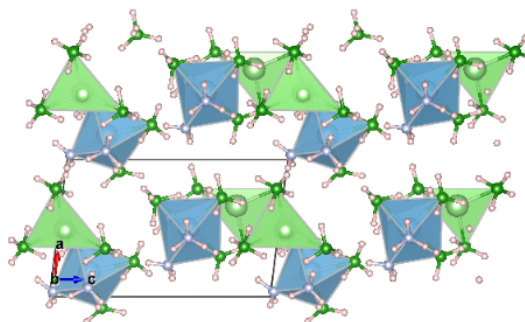
### 3.1.8 Crystal Structure Prediction for $M_1M_2(BH_4)_5(NH_3)_4$

Six different models shown in figure 3.17 were used for  $M_1M_2(BH_4)_5(NH_3)_4$ . In model1,  $M_2$  metal is surrounded by 4  $NH_3$  (in the equatorial position) and 2  $BH_4$  groups (in the axial position) to form an octahedral coordination. In addition, 3  $BH_4$  groups move independently in this model. In model2, there is an octahedral structure around  $M_2$  containing three  $NH_3$  and  $BH_4$  groups. This model also contains free 1  $NH_3$  and two  $BH_4$  groups. Model3 is quite similar to model2 except the coordination (trigonal bipyramid) adopted by  $M_2$ . In model4, there is a distorted octahedral geometry around  $M_2$  containing 3  $NH_3$  and  $BH_4$  groups. In all models except model5 and model6, there are free  $BH_4$  and  $NH_3$  groups. In model5, while  $M_2$  forms a trigonal bipyramid with five  $BH_4$  groups, there is a tetrahedral arrangement

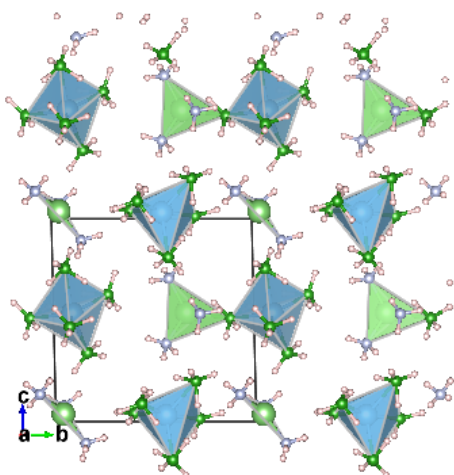




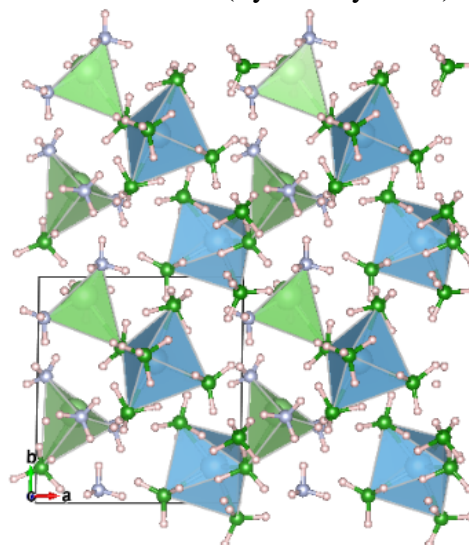
B5N3\_1 (Symmetry no: 9)



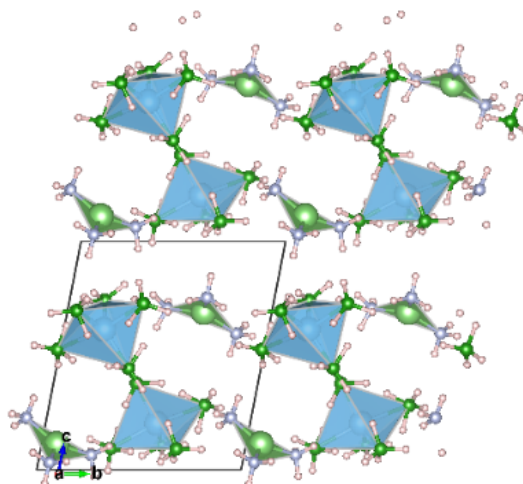
B5N3\_2 (Symmetry no: 1)



B5N3\_3 (Symmetry no: 1)



B5N3\_4 (Symmetry no: 1)



B5N3\_5 (Symmetry no: 1)

**Figure 3.16:** Different crystal structures of  $M_1M_2(BH_4)_5(NH_3)_3$  found by CASPESA.



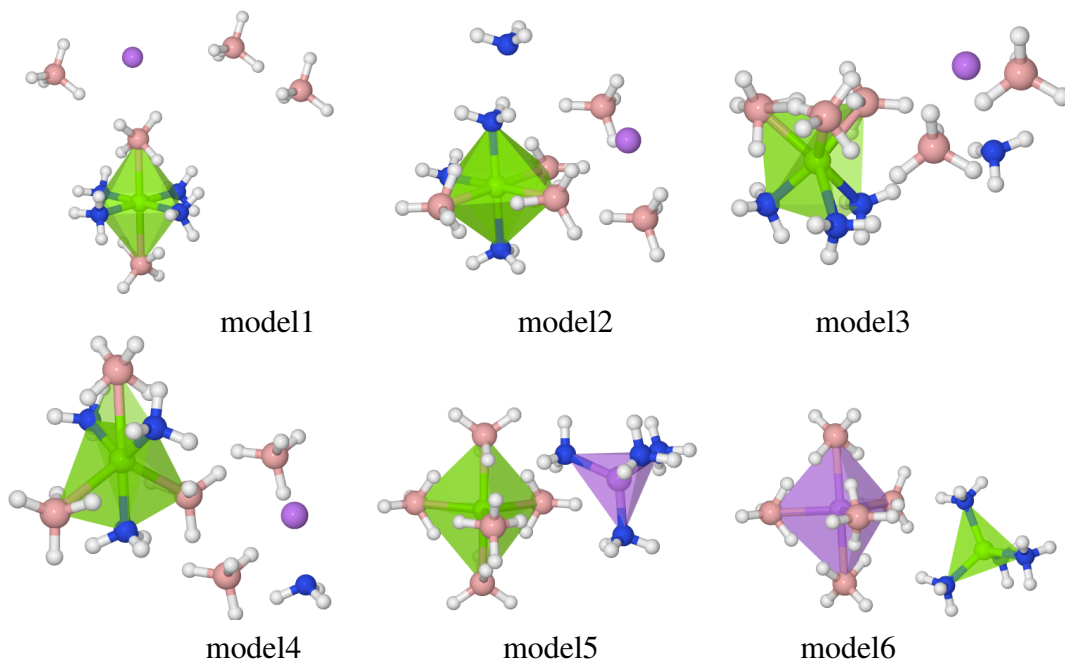
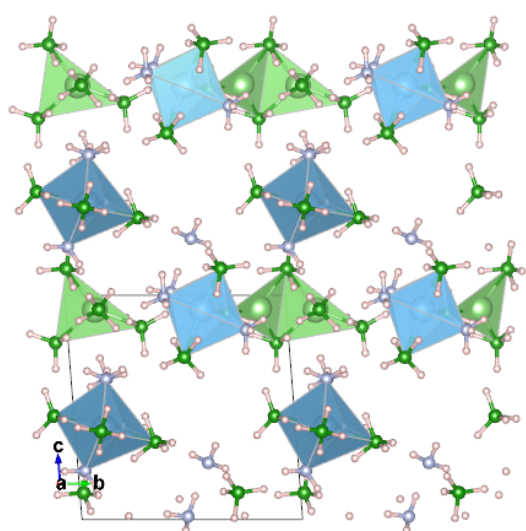


**Figure 3.17:** Coordination models for  $M_1M_2(BH_4)_5(NH_3)_4$ .

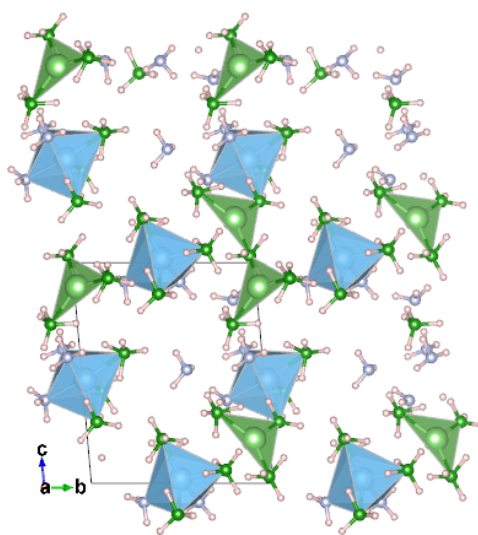
containing four  $NH_3$  molecules around  $M_1$ . Just in contrast to model5, arrangements around  $M_1$  and  $M_2$  are reversed in model6.

Template crystal structures found with DFT relaxations are shown in figure 3.18. Among them, in B5N4\_1, there is a distorted octahedral structure containing three  $NH_3$  and  $BH_4$  groups around  $M_2$ . Each Li atom is surrounded by 3  $BH_4$  groups to form a trigonal planar geometry. One free  $NH_3$  group also exists in this model. B5N4\_2 is very similar to B5N4\_1. B5N4\_3 is different from previous two structures and it was obtained by using model5. In this structure, while there is a trigonal bipyramid formed by five  $BH_4$  groups around  $M_2$ , a tetrahedral containing four  $NH_3$  molecules is located around  $M_1$ . In B5N4\_4,  $M_2$  metal has two different coordinations; one of these coordinations is a trigonal bipyramidal which is composed of 4  $NH_3$  and 1  $BH_4$  groups and the other coordination is distorted octahedral which is composed of 4  $NH_3$  and 2  $BH_4$  groups. It is also worth to mention that some of the  $BH_4$  groups in this structure is not connected to any metal atom. Moreover,  $M_1$  prefers to construct a trigonal planar orientation with three  $BH_4$  groups.

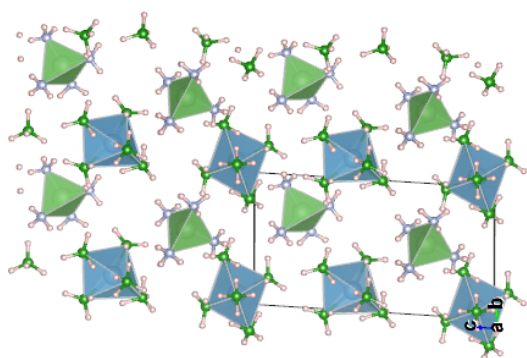
### 3.1.9 Crystal Structure Prediction for $M_1M_2(BH_4)_5(NH_3)_5$



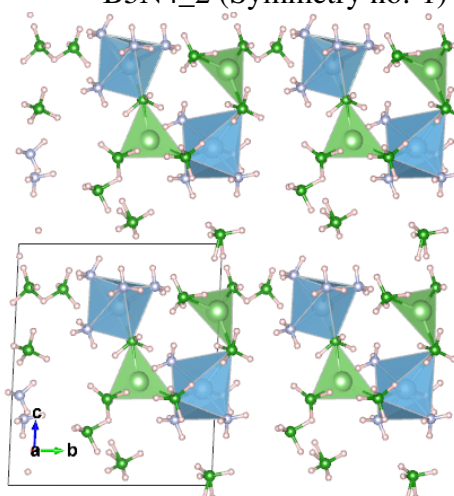
B5N4\_1 (Symmetry no: 1)



B5N4\_2 (Symmetry no: 1)



B5N4\_3 (Symmetry no: 1)



B5N4\_4 (Symmetry no: 1)

**Figure 3.18:** Different crystal structures of  $M_1M_2(BH_4)_5(NH_3)_4$  found by CASPESA.

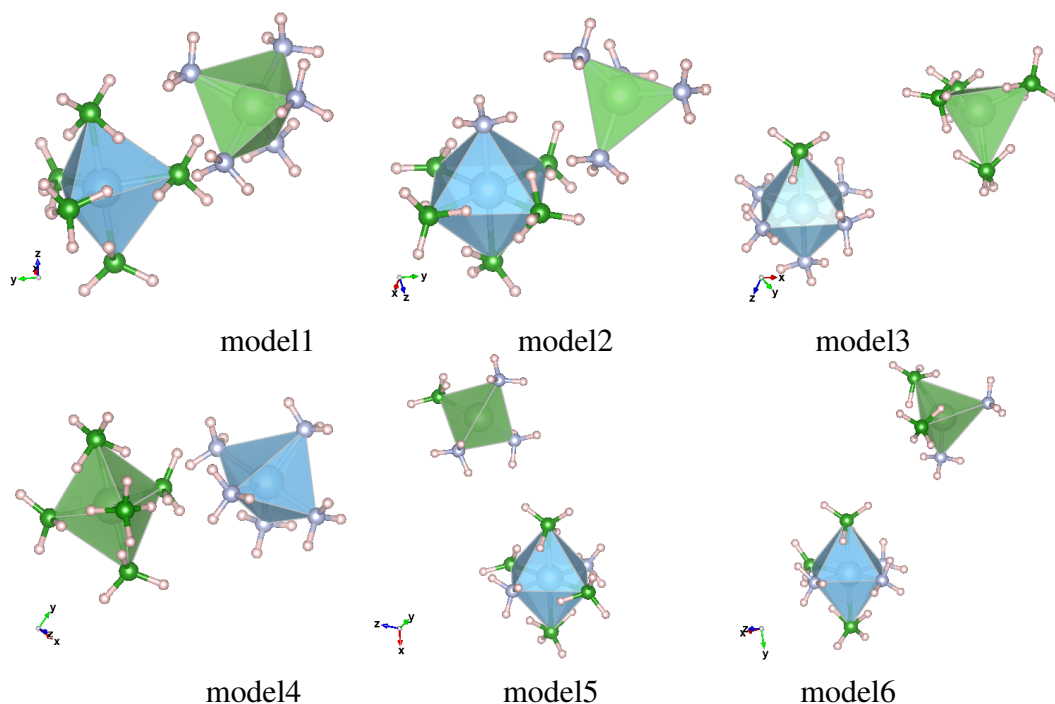


**Figure 3.19:** Coordination model for  $M_1M_2(BH_4)_5(NH_3)_5$ .

To predict the crystal structures of  $M_1M_2(BH_4)_5(NH_3)_5$  system, six different models shown in figure 3.19 were employed. In model1, there are trigonal bipyramid coordinations around  $M_1$  and  $M_2$  containing five  $NH_3$  and  $BH_4$  groups, respectively. In model2, while  $M_2$  forms an octahedral arrangement with five  $BH_4$  and one  $NH_3$  groups,  $M_1$  prefers a tetrahedral consisting of four  $NH_3$  molecules. Model3 is very similar to model2. It only differs from model2 regarding the coordinations around  $M_1$  and  $M_2$ . Model4 was obtained by swapping the coordination around  $M_1$  and  $M_2$  in model1. In model5,  $M_1$  metal has a tetrahedral coordination geometry composed of 3  $NH_3$  and 1  $BH_4$  groups.  $M_2$  prefers an octahedral coordination with four  $BH_4$  and two  $NH_3$  groups. In the last model,  $M_1$  metal has a tetrahedral coordination geometry composed of 2  $BH_4$  and  $NH_3$  groups. In this structure,  $M_2$  forms an octahedral with three  $BH_4$  and  $NH_3$  groups

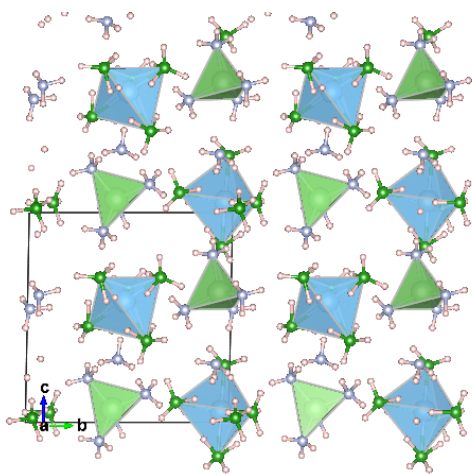
The Crystal structure templates found for  $M_1M_2(BH_4)_5(NH_3)_5$  system are shown in the figure 3.20. In B5N5\_1, while  $M_2$  has a trigonal bipyramid coordination containing five  $BH_4$  groups,  $M_1$  prefers a tetrahedral consisting of four  $NH_3$  molecules. This structure also includes a free  $NH_3$  molecule. Structure B5N5\_2 is same as model2. In B5N5\_3, all  $M_1$  metal has a trigonal planar coordination with 3  $BH_4$  groups. However,

$M_2$  prefers either an octahedral or a capped octahedral coordination with five  $NH_3$  and one  $BH_4$  groups. In this structure,  $M_2-B$  and  $M_2-N$  distances are in between 2.46 Å - 3.01 Å and 2.25 Å, respectively. B5N5\_4 was obtained to be similar to model5. In the last structure, B5N5\_5, coordinations around metals are similar to model6 with a difference of  $M_1$  which prefers a trigonal planar orientation containing two  $NH_3$  and one  $BH_4$  groups. This structure also contains a free  $BH_4$  group.

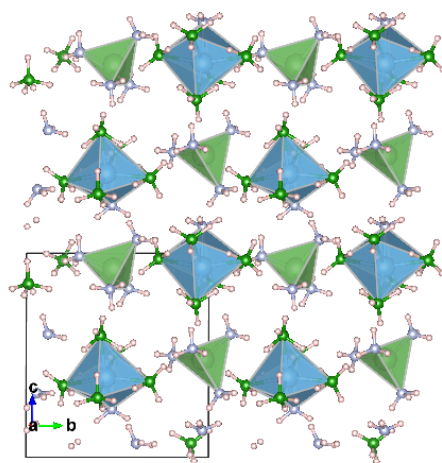
### 3.1.10 Crystal Structure Prediction for $M_1M_2(BH_4)_5(NH_3)_6$

To predict the crystal structures of  $M_1M_2(BH_4)_5(NH_3)_6$  system, six different models shown in figure 3.21 were used. In model1, while  $M_2$  prefers a trigonal bipyramid coordination with five  $BH_4$  groups,  $M_1$  forms an octahedral containing six  $NH_3$  molecules. In model2,  $M_1$  and  $M_2$  prefers a trigonal bipyramid containing five  $NH_3$  molecules and an octahedral with five  $BH_4$  and one  $NH_3$  groups, respectively. Model3 was generated by swapping coordinations around  $M_1$  and  $M_2$  in model1. In model4,  $M_2$  has an octahedral coordination geometry composed of 4  $BH_4$  and 2  $NH_3$  groups and  $M_1$  metal forms a trigonal bipyramidal with 4  $NH_3$  and one  $BH_4$  groups. In model5,  $M_1$  and  $M_2$  forms a trigonal bipyramid with two  $BH_4$  and three  $NH_3$  groups and an octahedral containing three  $BH_4$  and  $NH_3$  groups, respectively. In the last model,  $M_1$  metal has a trigonal bipyramidal coordination geometry composed of 3  $BH_4$  and 2  $NH_3$  groups and  $M_2$  metal forms an octahedral coordination with 2  $BH_4$  and 4  $NH_3$  groups.

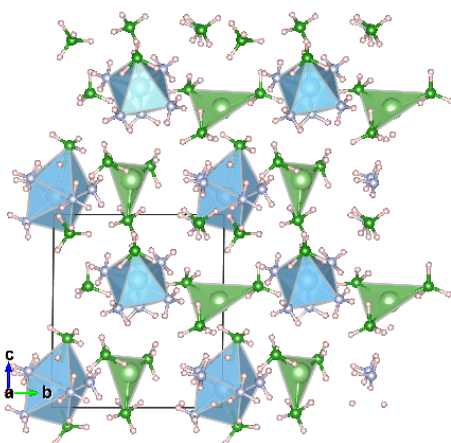
The template crystal structures obtained for  $M_1M_2(BH_4)_5(NH_3)_6$  system are shown in figure 3.22. In B5N6\_1, while  $M_2$  has a distorted octahedral coordination with four  $BH_4$  and two  $NH_3$  groups,  $M_1$  prefers a tetrahedral orientation with four  $NH_3$  molecules. There is also a free  $BH_4$  group in this structure. This structure shows a layered arrangement:  $M_1$  metals reside in one layer and  $M_2$  metals reside in another layer. In B5N6\_2,  $M_2$  metals have a distorted octahedral coordination geometry similar to B5N6\_1.  $M_1$  forms a tetrahedral either with four  $NH_3$  or three  $NH_3$  and one  $BH_4$  groups. This structure has also a layered arrangement similar to B5N6\_1. In the last structure,  $M_2$  metal forms a distorted octahedral with 2  $BH_4$  and 4  $NH_3$  groups and  $M_1$  metal has either a tetrahedral coordination containing 2  $BH_4$  and 2  $NH_3$  groups, or



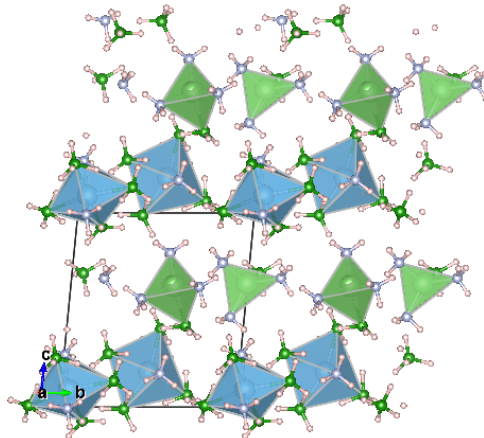
B5N5\_1 (Symmetry no: 1)



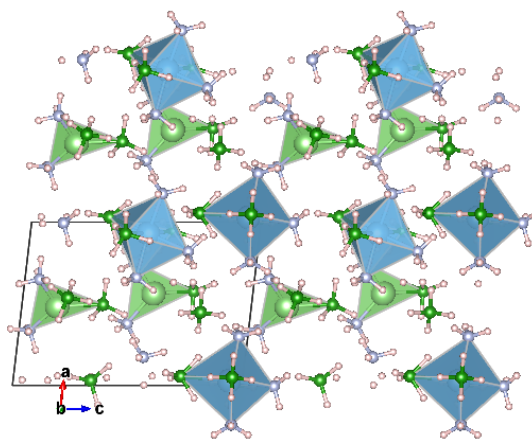
B5N5\_2 (Symmetry no: 1)



B5N5\_3 (Symmetry no: 1)



B5N5\_4 (Symmetry no: 1)



B5N5\_5 (Symmetry no: 1)

**Figure 3.20:** Different crystal structures of  $M_1M_2(BH_4)_5(NH_3)_5$  found by CASPESA.

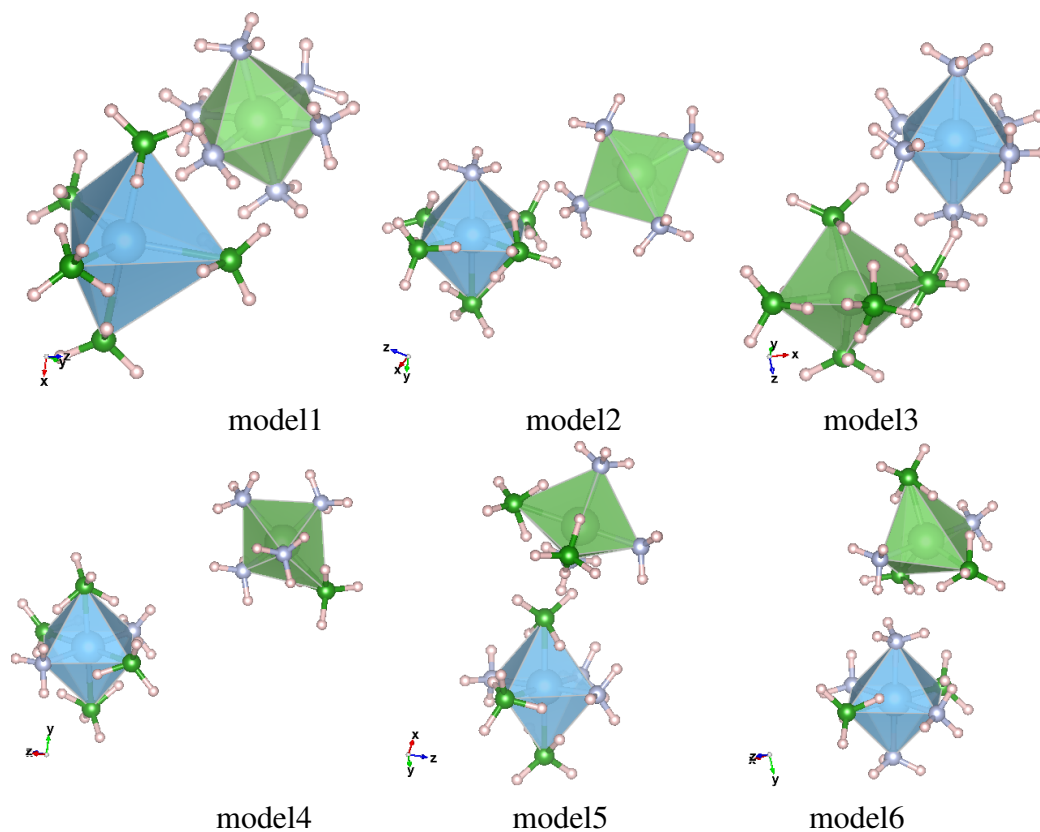


**Figure 3.21:** Coordination model for  $M_1M_2(BH_4)_5(NH_3)_6$ .

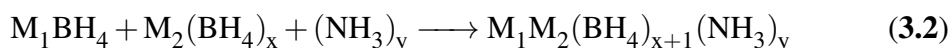
a trigonal planar coordination which is composed of 1  $BH_4$  group and 2  $NH_3$  groups. This structure also includes a free  $BH_4$  group.

### 3.2 Computational Screening

The template crystal structures introduced in the previous sections were employed for the computational screening. Alloying, formation, and decomposition energies were considered for the evaluation of AMB complexes. In particular, three different alloying energies were utilized. The first reaction was inspired from the synthesis reaction of  $Mg(BH_4)_2 \cdot 6 NH_3$  [26].



This reaction is actually modified as described in the following. In this new form, the alloy forms from the reaction between two borohydrides and ammonia.



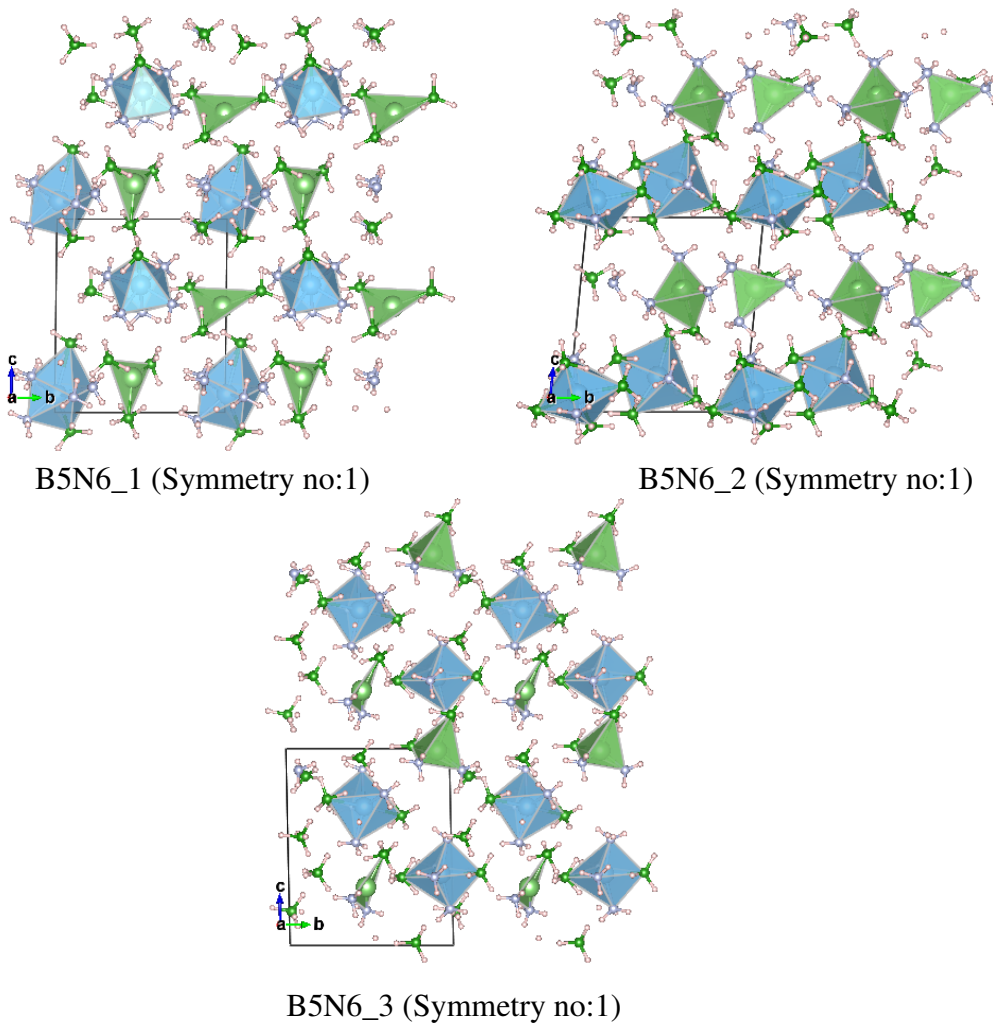


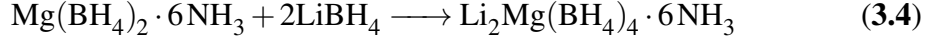
**Figure 3.22:** Different crystal structures of  $M_1M_2(BH_4)_5(NH_3)_6$  found by CASPESA.



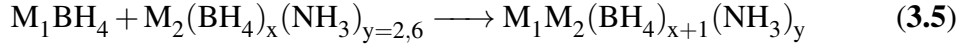
For this reaction, the alloying energy can be calculated as described below:

$$\Delta E_{alloy} = E_{M_1M_2(BH_4)_{x+1}(NH_3)_y} - (E_{M_1BH_4} + E_{M_2(BH_4)_x} + yE_{NH_3}) \quad (3.3)$$

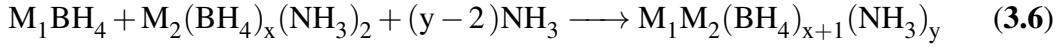
Recently, Yang et al. [27] synthesized  $Li_2Mg(BH_4)_4 \cdot 6NH_3$  complex using the reaction shown in below:



This reaction was rearranged as a reaction of an alkali metal borohydride and alkali/transition metal ammine borohydride as shown below, then it was used in the computational screening.



In this reaction, crystal structures are known only for  $M_2(BH_4)_x(NH_3)_y$ ,  $y=2, 6$ . For other values for  $y$ , even they have been synthesized, their crystal structure details were not reported. Therefore, for  $y=3,4,5$  the following reaction is considered:



For these two reactions, alloying energies are calculated as described below:

$$\Delta E_{alloy2} = E_{M_1M_2(BH_4)_{x+1}(NH_3)_y} - (E_{M_1BH_4} + E_{M_2(BH_4)_x(NH_3)_y}), \text{ for } y = 2 \text{ and } y = 6 \quad (3.7)$$

$$\Delta E_{alloy2} = E_{M_1M_2(BH_4)_{x+1}(NH_3)_y} - (E_{M_1BH_4} + E_{M_2(BH_4)_x(NH_3)_2} + (y-2)E_{NH_3}), \text{ for } y = 3, 4, 5 \quad (3.8)$$

Actually, to calculate  $\Delta E_{alloy2}$ , the energy of  $M_2(BH_4)_x(NH_3)_y$  complex is required. Therefore, crystal structure of this complex was also predicted using CASPESA. For this purpose,  $M_2$  metal is set to Mg, and crystal structures for other  $M_2$  metals were obtained by swapping Mg with the corresponding metal species. Recently, Chen et al. [66] have reported experimental and theoretical crystal structures of  $M(BH_4)_2(NH_3)_2$  ( $M=Mg, Ca$  and  $Zn$ ). These structures were also employed to calculate the energy of the complex including metal atoms except Mg, Ca and Zn. The energy of the structures obtained by CASPESA were compared with that of experimental structures and the lowest energy structure is considered for the calculation of the alloying energy.



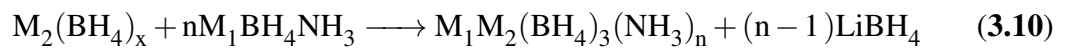
Unfortunately, there is no any crystal structure information about  $M_2(BH_4)_x(NH_3)_2$ ,  $x=3,4$  in the literature so CASPESA was also used for these systems with  $M_2 = Sc$  and  $Zr$ . Six different structures were found for  $Sc(BH_4)_3(NH_3)_2$  and they are shown in the figure 3.23. Among them, ScB3N2\_5 was obtained to be the lowest energy structure. All structures are stabilized by dihydrogen bonds (N-H  $\cdots$  H-B) which are in between 2.10 Å – 2.47 Å. The total energy of  $M_2(BH_4)_3(NH_3)_2$  ( $M_2=Al, Y, Sc, Mo, Co, Ti$ ) complexes are calculated by swapping metal atom in the crystal structure ScB3N2\_5 with one of the metal atom listed above.

Seven different crystal structures were found for  $Zr(BH_4)_4(NH_3)_2$  and they are shown in the figure 3.24. In all these structures, Zr has an octahedral coordination geometry composed of 4  $BH_4$  and 2  $NH_3$  groups and similar to the previous complex, these structures are stabilized by dihydrogen bonds. ZrB4N2\_4 was obtained as the lowest energy structure and it contains dihydrogen bonds in between 2.10 Å – 2.26 Å. This crystal structure was used to calculate the energy of  $M_2(BH_4)_4(NH_3)_2$  ( $M_2 = Zr, Ti, Mn, Mo, Co$ ). The total energies of the other complexes including metal atoms except Zr were obtained by swapping Zr by one of the metals listed in the following: Ti, Mn, Mo and Co

Sun et al. [2] synthesized  $LiMg(BH_4)_3(NH_3)_2$  using the following reaction:



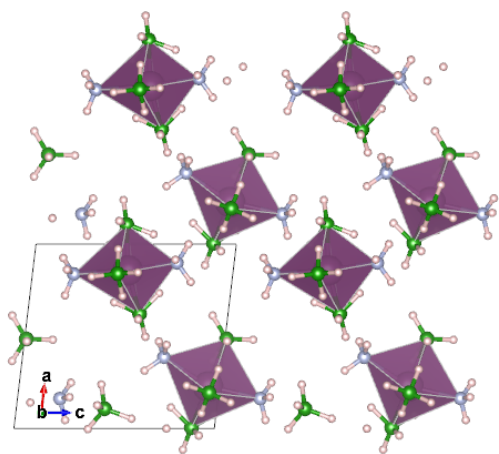
This reaction was rearranged as shown below and then it was used in the computational screening:



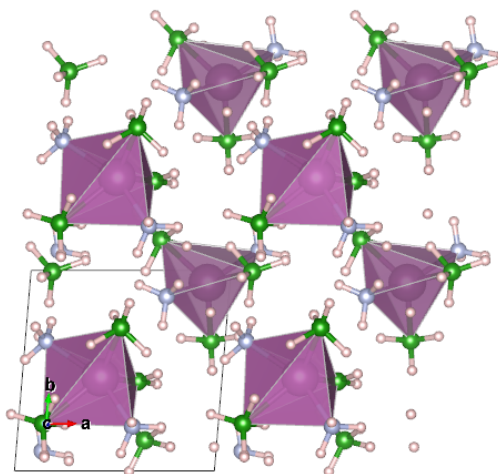
The alloying energy  $\Delta E_{alloy3}$  for this reaction is calculated as described below:

$$\Delta E_{alloy3} = (E_{M_1M_2(BH_4)_{x+1}(NH_3)_n} + (n-1)E_{LiBH_4}) - (E_{M_2(BH_4)_x} + nE_{M_1BH_4NH_3}) \quad (3.11)$$

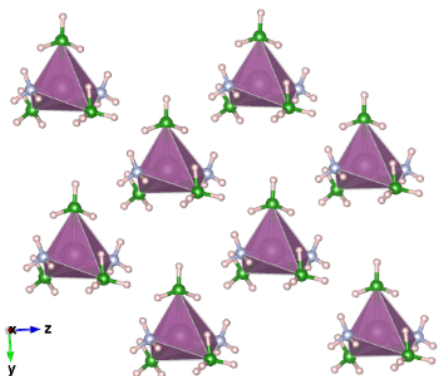
According to this calculation,  $E_{M_1BH_4NH_3}$  is required to obtain  $\Delta E_{alloy3}$ . Guo et al. [1] have recently discovered that crystal structure of  $LiBH_4NH_3$  is orthorhombic Pnma (symmetry no: 62). The cell parameters of this structure are  $a=5.97$  Å,  $b=4.64$  Å and  $c=14.35$  Å and each Li atom has a tetrahedral coordination geometry composed of



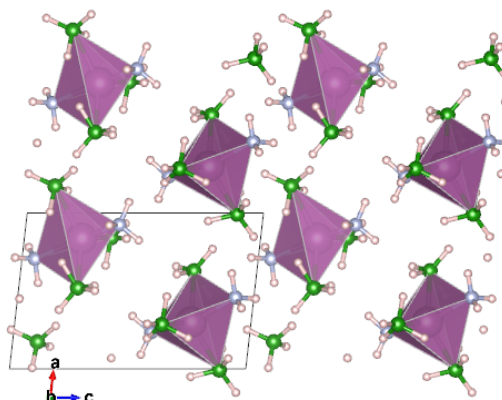
ScB3N2\_1 (Symmetry no: 1)



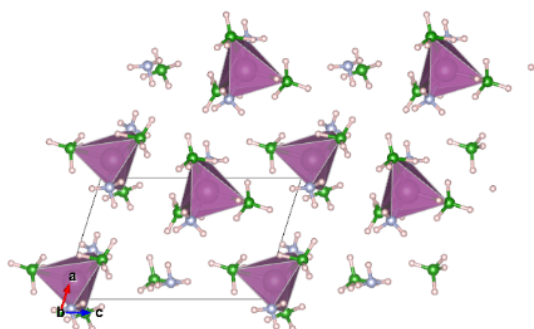
ScB3N2\_2 (Symmetry no: 1)



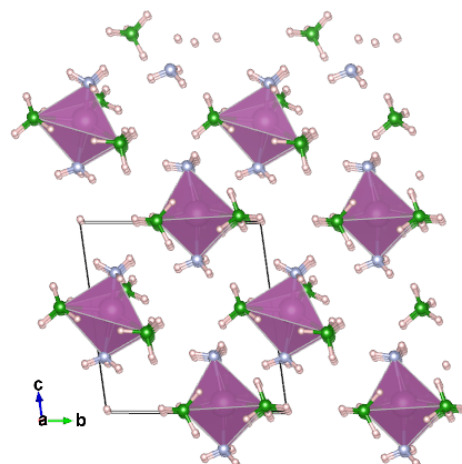
ScB3N2\_3 (Symmetry no: 1)



ScB3N2\_4 (Symmetry no: 1)

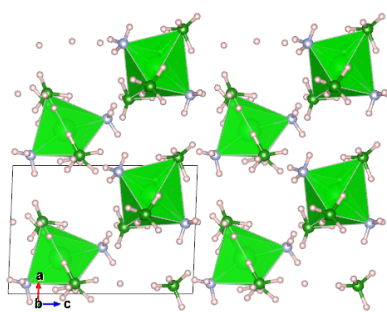


ScB3N2\_5 (Symmetry no: 1)

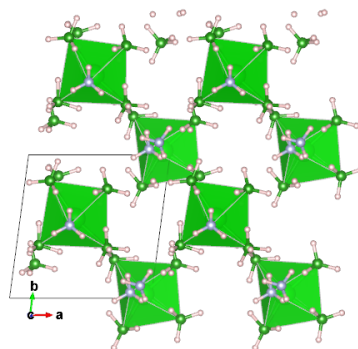


ScB3N2\_6 (Symmetry no: 1)

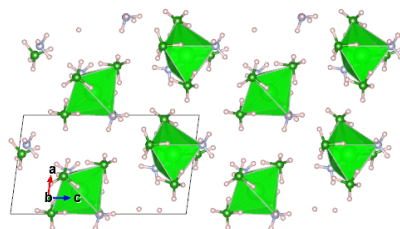
**Figure 3.23:** Different crystal structures of  $\text{Sc}(\text{BH}_4)_3(\text{NH}_3)_2$  found by CASPESA.



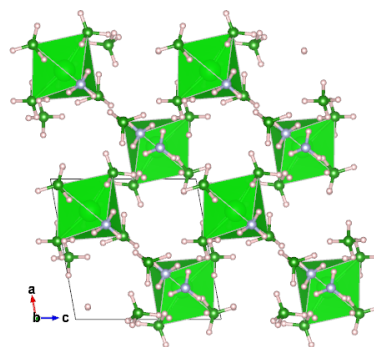
ZrB4N2\_1 (Symmetry no: 1)



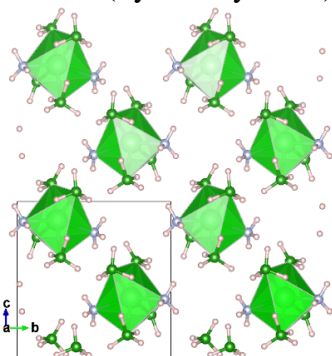
ZrB4N2\_2 (Symmetry no: 1)



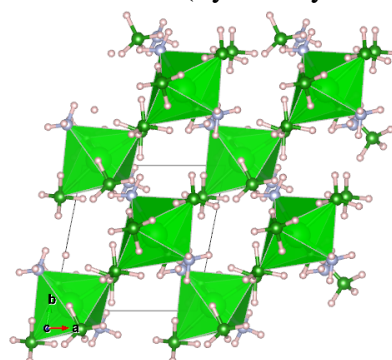
ZrB4N2\_3 (Symmetry no: 1)



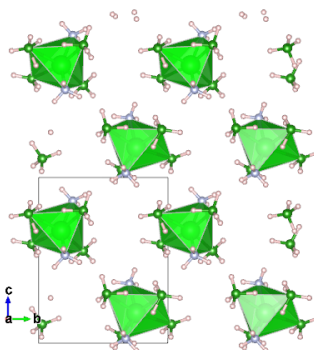
ZrB4N2\_4 (Symmetry no: 4)



ZrB4N2\_5 (Symmetry no: 7)



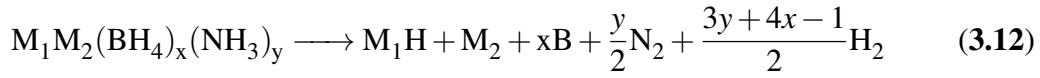
ZrB4N2\_6 (Symmetry no: 1)



ZrB4N2\_7 (Symmetry no: 1)

**Figure 3.24:** Different crystal structures of  $\text{Zr}(\text{BH}_4)_4(\text{NH}_3)_2$  found by CASPESA.

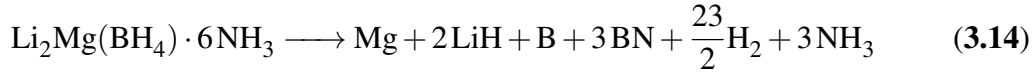
3 BH<sub>4</sub> and 1 NH<sub>3</sub> groups. 2 BH<sub>4</sub> groups are shared by 2 Li atoms leading to a Li chain formation parallel to [010] plane. Unfortunately, there is no any experimental information about the crystal structures of NaBH<sub>4</sub>NH<sub>3</sub> and KBH<sub>4</sub>NH<sub>3</sub>. In order to calculate energies of this systems, crystal structure of LiBH<sub>4</sub>NH<sub>3</sub> was used by substituting Li with Na and K and then all atomic coordinates and cell parameters were optimized with DFT. AMBs follow very diverse reaction paths to decompose into various products (such as diborane, dodecaborane, ammonia, BN<sub>3</sub>, HBN<sub>2</sub>, borazine (HNBH<sub>3</sub>) and release hydrogen. The simplest decomposition reaction that can be regarded is shown below. In this reaction, only stable alkali metal borohydride, alkaline earth metal/transition metal, boron, nitrogen and hydrogen are produced.



Decomposition energy ( $\Delta E_{decomp1}$ ) for this reaction is calculated as follows:

$$\Delta E_{decomp1} = E_{M_1M_2(BH_4)_x(NH_3)_y} - (E_{M_1H} + E_{M_2} + xE_B + \frac{y}{2}E_{N_2} + \frac{3y+4x-1}{2}E_{H_2}) \quad (3.13)$$

In addition, decomposition reaction of Li<sub>2</sub>Mg(BH<sub>4</sub>)<sub>4</sub>(NH<sub>3</sub>)<sub>6</sub>, which is reported by Yang et al. [27], was also considered as an alternative decomposition reaction.



The general form of this reaction, as described below, was used in the screening:

$$\Delta E_{decomp2} = E_{M_1M_2(BH_4)_x(NH_3)_y} - (E_{M_1H} + E_{M_2} + \frac{y}{2}E_{NH_3} + \frac{y}{2}E_{BN} + (x - \frac{y}{2})E_B + ((3y+5x) - (\frac{3y}{2} + 1))E_{H_2}) \quad (3.15)$$

In addition to the decomposition energy, the formation energy ( $\Delta E_{form}$ ) is calculated by subtracting the energy of individual atoms from the energy of the AMB.

$$\Delta E_{form} = E_{M_1M_2(BH_4)_x(NH_3)_y} - (E_{M_1} + E_{M_2} + xE_B + \frac{y}{2}E_{N_2} + \frac{3y+4x}{2}E_{H_2}) \quad (3.16)$$

As it can be seen from these reactions, to know the energy of AMB ( $E_{M_1M_2(BH_4)_x(NH_3)_y}$ ) is not enough to calculate these corresponding energies. For this purpose energies of alkali metal borohydrides, earth alkaline/transition metal borohydrides ( $E_{M_1BH_4}$  and  $E_{M_2(BH_4)_x}$ ), ammonia ( $E_{NH_3}$ ), alkali metal hydrides ( $E_{M_1H}$ ), elemental metals, boron, nitrogen and hydrogen are also required. To calculate the energy of gaseous N<sub>2</sub>, H<sub>2</sub>

and  $\text{NH}_3$ , they were placed in a cubic unit cell with a cell parameter of  $a=10 \text{ \AA}$ . Due to the employment of a such big cell parameter, the interactions between molecules in the neighbouring cells are eliminated. Ca, Sr and Ni metals have face centered cubic unit cell, Mn, Li, Na, and K have body centered cubic unit cell, Mg and Zn have hexagonal close-packed unit cell. Alfa rhombohedral structure is used for boron. All alkali metal borohydrides ( $\text{LiH}$ ,  $\text{NaH}$ ,  $\text{KH}$ ) have a crystal structure similar to  $\text{NaCl}$  and this crystal structure has a cubic  $\text{Fm-3m}$  symmetry. For metal borohydrides, crystal structures reported in the literature were used to calculate the energy. For example, the minimum energy structure, orthorhombic  $\text{I-4m2}$  (symmetry no: 119) found by Tekin et al. [20], was used to calculate energy of  $\text{LiBH}_4$ . Similarly, for  $\text{NaBH}_4$  and  $\text{Mg}(\text{BH}_4)_2$ , Caputo et al. [19, 21] discovered their crystal structures to be tetragonal  $\text{P42/nmc}$  (symmetry no: 137) and orthorhombic  $\text{I-4m2}$  (symmetry no: 119), respectively, and these crystal structures were used in calculation of energies.  $\text{KBH}_4$  has a tetragonal  $\text{P4}_2/\text{nmc}$  (symmetry no: 137) symmetry [29]. Miwa et al. [67] have discovered that  $\text{Ca}(\text{BH}_4)_2$  has an orthorhombic  $\text{Fddd}$  (symmetry no: 70) symmetry and this structure was utilized in the calculations. The crystal structure of  $\text{Sr}(\text{BH}_4)_2$  (orthorhombic  $\text{Pbcn}$  (symmetry no: 60) was obtained from the experimental study of Ravnsbaek et al. [68]. There is no any information about the crystal structure of  $\text{Ni}(\text{BH}_4)_2$ , therefore the crystal structure of  $\text{Mg}(\text{BH}_4)_2$  (tetragonal  $\text{I-4m2}$  (symmetry no: 119)) was used. Firstly, Mg is substituted with Ni and then atomic coordinates and cell parameters were optimized. After the optimization, a triclinic  $\text{P1}$  (symmetry no:1) structure was obtained. A lot of information about the crystal structure of  $\text{Zn}(\text{BH}_4)_2$  can be found in the literature and all of these information were used in this study. In particular, five different structures ( $\text{Pmc2}_1$  (no: 26),  $\text{F222}$  (no: 22),  $\text{I-4m2}$  (no: 119),  $\text{I4}_1\text{22}$  (no: 98) and  $\text{P-1}$  (no: 2)) reported by Huan et al. [69] , were considered. The crystal structure of  $\text{Mn}(\text{BH}_4)_2$  (trigonal  $\text{P31}_1\text{2}$  (no: 151)) was reported by Cerny et al. [70]. In addition to these structures, the crystal structure of BN which is used in the calculation of  $E_{\text{decomp2}}$  , was obtained from the study of Kurakevych and Solozhenko [71]. This structure has a hexagonal  $\text{P-6m2}$  (symmetry no: 187) symmetry unit cell. The details about all structures are shown in table 3.1. As can be seen from the table, all cell parameters, which were obtained from the literature, changed after DFT optimization.

**Table 3.1:** The cell parameters of the structures used in the study.

| Metal             | a     | b     | c     | $\alpha$ | $\beta$ | $\gamma$ | Symmetry             | Reference |
|-------------------|-------|-------|-------|----------|---------|----------|----------------------|-----------|
| Li                | 3.44  |       |       |          |         |          | Pm $\bar{3}$ m(221)  |           |
| Na                | 4.23  |       |       |          |         |          | Pm $\bar{3}$ m(221)  |           |
| K                 | 5.16  |       |       |          |         |          | Pm $\bar{3}$ m(221)  |           |
| Ca                | 5.53  |       |       |          |         |          | Pm $\bar{3}$ m(221)  |           |
| Sr                | 5.94  |       |       |          |         |          | Pm $\bar{3}$ m(221)  |           |
| Ni                | 3.54  |       |       |          |         |          | Pm $\bar{3}$ m(221)  |           |
| Mn                | 8.74  |       |       |          |         |          | P $\bar{4}$ 3m(215)  |           |
| Mg                | 3.83  | 3.83  | 4.03  | 90       | 90      | 120      | P6 $_3$ /mmc(194)    |           |
| Zn                | 3.20  | 3.20  | 3.41  | 90       | 90      | 120      | P6 $_3$ /mmc(194)    |           |
| B                 | 4.89  | 4.89  | 12.44 | 90       | 90      | 120      | R $\bar{3}$ m(166)   |           |
| Co                | 3.20  | 3.77  | 3.81  | 90       | 90      | 90       | Cmcm(63)             |           |
| Mo                | 3.16  | 3.16  | 3.16  | 90       | 90      | 90       | Pm $\bar{3}$ m(221)  |           |
| Ti                | 2.36  | 2.36  | 6.23  | 90       | 90      | 120      | P6 $_3$ /mmc(194)    |           |
| Zr                | 2.58  | 2.58  | 6.77  | 90       | 90      | 120      | P6 $_3$ /mmc(194)    |           |
| LiH               | 4.04  |       |       |          |         |          | Fm $\bar{3}$ m(225)  |           |
| NaH               | 4.80  |       |       |          |         |          | Fm $\bar{3}$ m(225)  |           |
| KH                | 5.46  |       |       |          |         |          | Fm $\bar{3}$ m(225)  |           |
| LiBH $_4$         | 8.48  | 4.35  | 5.75  | 90       | 90      | 90       | Pnma(62)             | [20]      |
| NaBH $_4$         | 4.36  | 4.36  | 5.90  | 90       | 90      | 90       | P4 $_2$ /nmc(137)    | [21]      |
| KBH $_4$          | 4.75  | 4.75  | 6.66  | 90       | 90      | 90       | P4 $_2$ /nmc(137)    | [29]      |
| Ca(BH $_4$ ) $_2$ | 8.79  | 13.14 | 7.50  | 90       | 90      | 90       | Fddd(70)             | [67]      |
| Sr(BH $_4$ ) $_2$ | 7.02  | 8.51  | 7.62  | 90       | 90      | 90       | Pbcn(60)             | [68]      |
| Ni(BH $_4$ ) $_2$ | 7.23  | 7.23  | 10.05 | 88.24    | 91.79   | 87.04    | P1(1)                | [8]       |
| Mn(BH $_4$ ) $_2$ | 10.43 | 10.43 | 10.83 | 90       | 90      | 90       | P3 $_1$ 12(151)      | [70]      |
| Mg(BH $_4$ ) $_2$ | 8.18  | 8.18  | 10.07 | 90       | 90      | 90       | I $\bar{4}$ m2(119)  | [8]       |
| Zn(BH $_4$ ) $_2$ | 4.12  | 4.86  | 7.92  | 90       | 90      | 90       | Pmc2 $_1$ (26)       | [69]      |
| Zn(BH $_4$ ) $_2$ | 9.93  | 11.18 | 11.89 | 90       | 90      | 90       | F222(22)             | [69]      |
| Zn(BH $_4$ ) $_2$ | 8.30  | 8.30  | 9.34  | 90       | 90      | 90       | I $\bar{4}$ m2(119)  | [69]      |
| Zn(BH $_4$ ) $_2$ | 6.99  | 6.99  | 12.19 | 90       | 90      | 90       | I4 $_1$ 22(98)       | [69]      |
| Zn(BH $_4$ ) $_2$ | 6.88  | 5.44  | 7.84  | 89.50    | 76.15   | 89.98    | P $\bar{1}$ (2)      | [69]      |
| Co(BH $_4$ ) $_3$ | 34.48 | 11.78 | 12.05 | 90       | 90      | 90       | Pna2 $_1$ (33)       | [72]      |
| Mo(BH $_4$ ) $_3$ | 6.93  | 12.14 | 8.67  | 90       | 90      | 90       | P2 $_1$ 2 $_1$ 2(18) | [73]      |
| Ti(BH $_4$ ) $_3$ | 8.85  | 12.56 | 7.17  | 90       | 90      | 90       | P222 $_1$ (17)       | [73]      |
| Co(BH $_4$ ) $_4$ | 5.71  |       |       |          |         |          | P $\bar{4}$ 3m(215)  | [74]      |
| Mn(BH $_4$ ) $_4$ | 6.02  |       |       |          |         |          | P $\bar{4}$ 3m(215)  | [74]      |
| Mo(BH $_4$ ) $_4$ | 6.20  |       |       |          |         |          | P $\bar{4}$ 3m(215)  | [74]      |
| Ti(BH $_4$ ) $_4$ | 6.10  |       |       |          |         |          | P $\bar{4}$ 3m(215)  | [74]      |
| Zr(BH $_4$ ) $_4$ | 6.34  |       |       |          |         |          | P $\bar{4}$ 3m(215)  | [74]      |
| BN                | 2.53  | 2.53  | 6.96  | 90       | 90      | 120      | P6 $_3$ /mmc(194)    | [71]      |
| LiBH $_4$ NH $_3$ | 6.13  | 4.39  | 13.41 | 90       | 90      | 90       | Pnma(62)             | [1]       |
| NaBH $_4$ NH $_3$ | 6.42  | 4.72  | 14.54 | 90       | 90      | 90       | Pnma(62)             | [1]       |
| KBH $_4$ NH $_3$  | 6.83  | 5.03  | 14.83 | 90       | 90      | 90       | Pnma(62)             | [1]       |

In the computational screening study, the promising dual cation AMBs were screened according to these two criteria:  $\Delta E_{alloy} < 0.0$  eV/f.u. and  $0.0 \leq \Delta E_{decomp} \leq -0.8$  eV/H<sub>2</sub>. The negative alloying energy means that elements of the compound prefer to be in the form of M<sub>1</sub>M<sub>2</sub>(BH<sub>4</sub>)<sub>x</sub>(NH<sub>3</sub>)<sub>y</sub> instead of being individual. The positive decomposition energy means that AMB does not require an external energy to decompose, in other words, the alloy is not stable. Therefore, for a promising AMB, the decomposition energy must be negative but not too negative, because in the latter case, AMB requires very high temperatures for the decomposition. The ideal decomposition energy was reported to be -0.2 eV / H<sub>2</sub> [5]. The considered decomposition reaction, which is mentioned before, may not fit for all the dual cation AMBs that are screened, therefore the ideal decomposition energy is assumed to be in between -0.8 eV / H<sub>2</sub> - -0.2 eV / H<sub>2</sub>.

### 3.2.1 Screening Results for M<sub>1</sub>M<sub>2</sub>(BH<sub>4</sub>)<sub>3</sub>(NH<sub>3</sub>)<sub>y</sub>

Screening results for 90 different M<sub>1</sub>M<sub>2</sub>(BH<sub>4</sub>)<sub>3</sub>(NH<sub>3</sub>)<sub>y</sub> are shown in the figure 3.25. In this figure, the x-axis represents decomposition energy ( $\Delta E_{decomp2}$ ) and the y-axis represents alloying energy ( $\Delta E_{alloy1}$ ). There are lots of complexes residing in the target region. Among these complexes, LiMg(BH<sub>4</sub>)<sub>3</sub>(NH<sub>3</sub>)<sub>2</sub> and NaZn(BH<sub>4</sub>)<sub>3</sub>(NH<sub>3</sub>)<sub>2</sub> were synthesized experimentally. Especially, the complexes in the form M<sub>1</sub>Ni(BH<sub>4</sub>)<sub>3</sub>(NH<sub>3</sub>)<sub>y</sub> and M<sub>1</sub>Mn(BH<sub>4</sub>)<sub>3</sub>(NH<sub>3</sub>)<sub>y</sub> are located in the target region and there is no any experimental study about these complexes in the literature. The most of the complexes which contain Mg or Sr are on the border of the target region. The complexes which contain Ca or Sr metals have very low decomposition energies. The interesting thing about this plot is that complexes containing Zn are only stable when the complex also includes Na and an ammonia content of 2, 3 or 6. In other words, Zn does not want to be together with Li or K. Gu et al. [75] recently tried to synthesize LiZn(BH<sub>4</sub>)<sub>3</sub>(NH<sub>3</sub>)<sub>2</sub> but they observed that resulting structure has 58.6 wt % Zn(BH<sub>4</sub>)<sub>2</sub>(NH<sub>3</sub>)<sub>2</sub> and 39.4 wt % LiCl. This shows that LiZn(BH<sub>4</sub>)<sub>3</sub>(NH<sub>3</sub>)<sub>2</sub> can not be synthesized experimentally and this fact is consistent with our screening results.

The plot in figure 3.26 presents wt % H of these structures versus decomposition energy. The complexes which contain Li metal have the highest hydrogen content

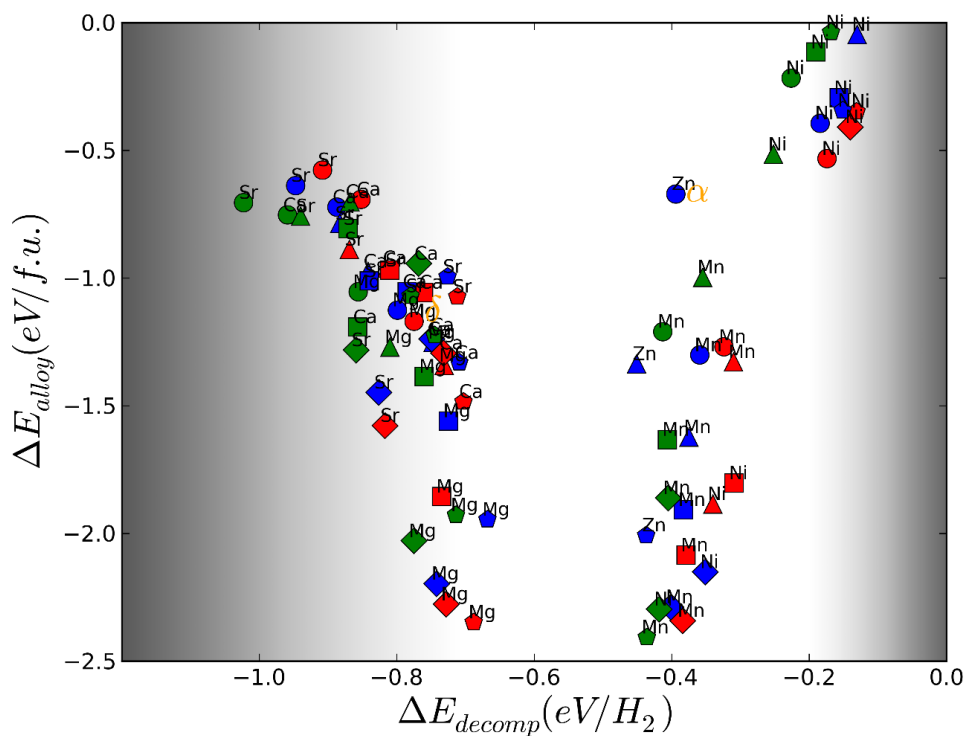


**Figure 3.25:** The alloying energies,  $\Delta E_{alloy}$ , are plotted against to the decomposition energies,  $\Delta E_{decomp}$  for  $M_1M_2(BH_4)_3(NH_3)_y$   $y=2,3,4,5,6$ . Representing colours: Li (Red), Na (Blue), K (Green).  $NH_3$  content:  $x=2$  (circle),  $x=3$  (triangle),  $x=4$  (square),  $x=5$  (diamond) and  $x=6$  (pentagon). Experimental observations:  $\alpha = NaZn(BH_4)_3(NH_3)_2$  [3] ,  $\delta = LiMg(BH_4)_3(NH_3)_2$  [2].



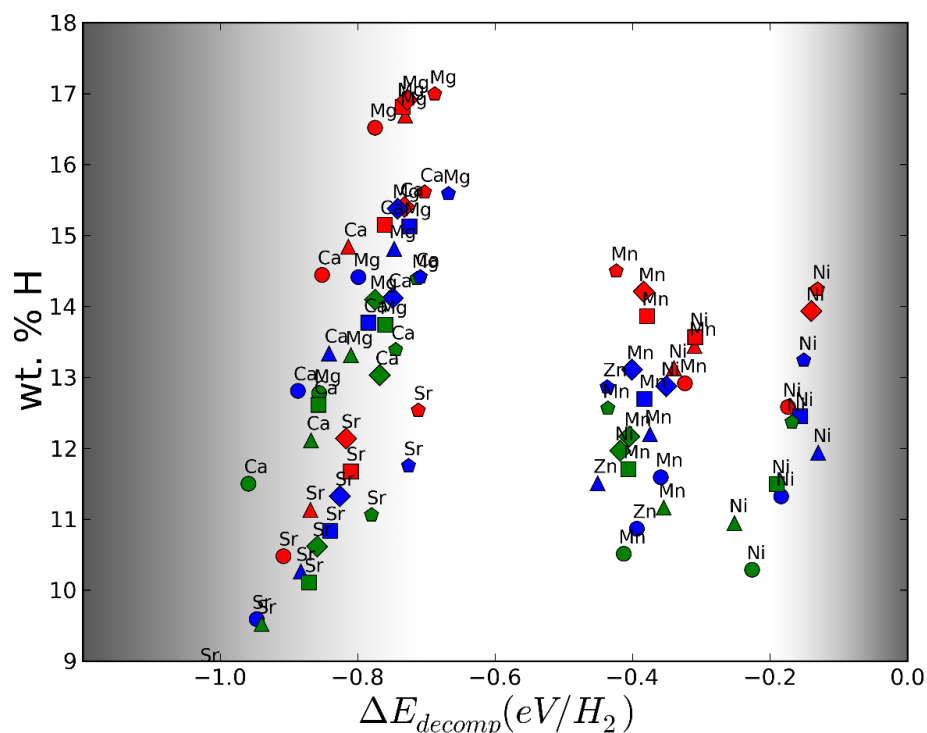


**Figure 3.26:** Hydrogen capacity is plotted against to the decomposition energy for  $M_1M_2(BH_4)_3(NH_3)_y$   $y=2,3,4,5,6$ . Representing colours: Li (Red), Na (Blue), K (Green).  $NH_3$  content:  $x=2$  (circle),  $x=3$  (triangle),  $x=4$  (square),  $x=5$  (diamond) and  $x=6$  (pentagon).

as expected. The most of the complexes are above the wt % 9 which is the DOE 2015 target [18].

In figure 3.27, the alloying energies are shown against to  $M_2$  metals. According to this plot, complexes containing Zn, are unstable except  $NaZn(BH_4)_3(NH_3)_2$ ,  $NaZn(BH_4)_3(NH_3)_3$  and  $NaZn(BH_4)_3(NH_3)_6$ . The remaining complexes are stable for all  $NH_3$  content.

Recently, it was reported that the decomposition temperature and the average Pauling electronegativity of cations in AMB have a linear relation [28,29]. This relation shown in figure 3.18 is in agreement with the experimental expectations except the complexes containing Zn. The average electronegativity for the stable complexes were found in between 0.9 and 1.5.

### 3.2.2 Screening Results for $M_1M_2(BH_4)_5(NH_3)_y$

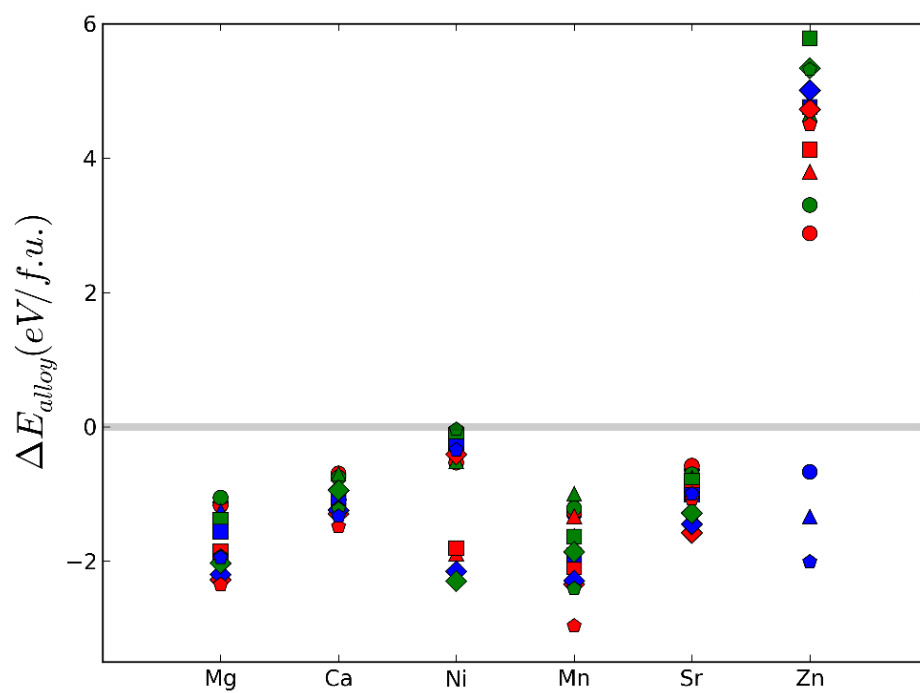


**Figure 3.27:** The alloying energies,  $\Delta E_{alloy}$ , are plotted against to  $M_2$  metal species for  $M_1M_2(BH_4)_3(NH_3)_y$   $y=2,3,4,5,6$ . Representing colours: Li (Red), Na (Blue), K (Green).  $NH_3$  content:  $x=2$  (circle),  $x=3$  (triangle),  $x=4$  (square),  $x=5$  (diamond) and  $x=6$  (pentagon).

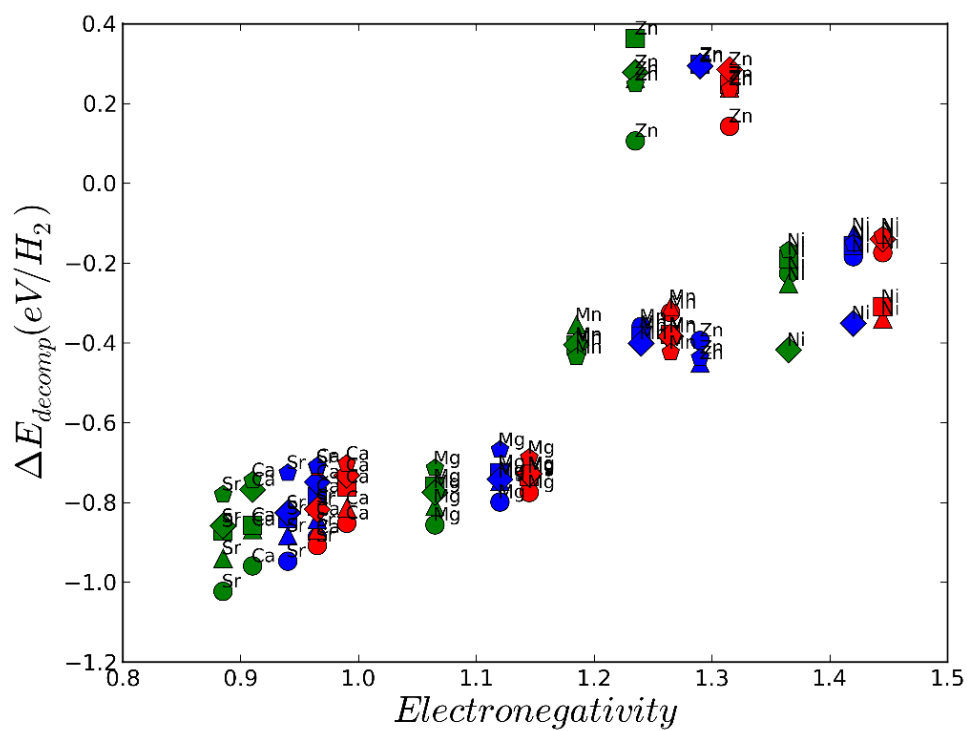


**Figure 3.28:** The decomposition energy,  $\Delta E_{decomp}$ , is plotted against to the average Pauling electronegativity of cations. Representing colours: Li (Red), Na (Blue), K (Green). NH<sub>3</sub> content: x=2 (circle), x=3 (triangle), x=4 (square), x=5 (diamond) and x=6 (pentagon).

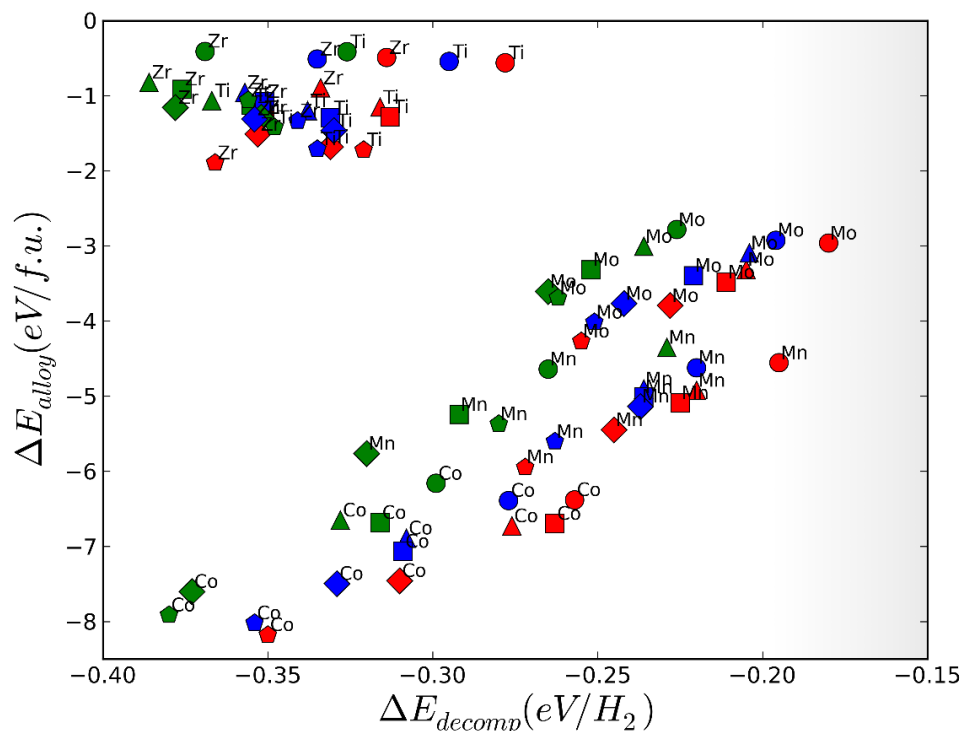


**Figure 3.29:** The alloying energies,  $\Delta E_{alloy}$ , are plotted against to the decomposition energies,  $\Delta E_{decomp}$  for  $M_1M_2(BH_4)_5(NH_3)_y$   $y=2,3,4,5,6$ . Representing colours: Li (Red), Na (Blue), K (Green).  $NH_3$  content:  $x=2$  (circle),  $x=3$  (triangle),  $x=4$  (square),  $x=5$  (diamond) and  $x=6$  (pentagon).

Screening results for 75 different  $M_1M_2(BH_4)_5(NH_3)_y$  are shown in figure 3.29. In this plot, the x-axis represents the decomposition energy  $\Delta E_{decomp2}$  and the y-axis represents the alloying energy  $\Delta E_{alloy1}$ . All complexes were found to be residing in the targeted region.

Complexes containing Co have the lowest alloying energy ( $\Delta E_{alloy1}$ ). For  $M_1M_2(BH_4)_5(NH_3)_y$ , there is no any synthesized complex reported in the literature.

The hydrogen content of these systems are shown in figure 3.30. The hydrogen capacity of all of the complexes are above the DOE 2015 target [18]. LiTi and LiCo compounds have the highest hydrogen content ( $\sim 16.5$  wt % H and  $\sim 15.5$  wt % H, respectively). In figure 3.31, the alloying energies are plotted against to the  $M_2$  metal species. It is clear from this figure that all the alloying energies of the complexes are negative. More specifically, complexes containing Co have lower alloying energies

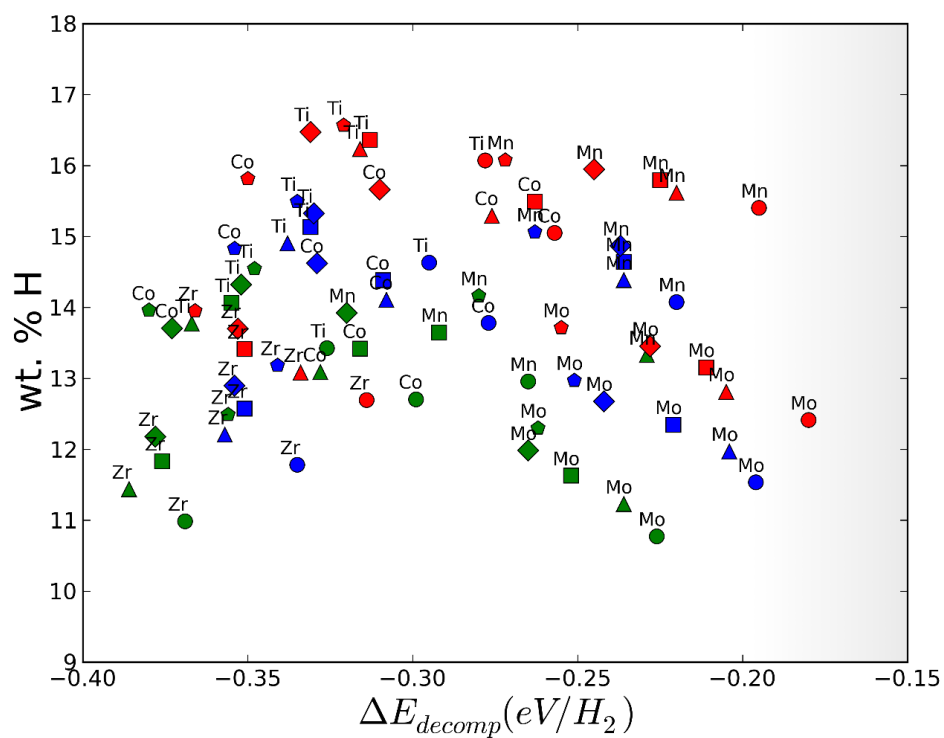


**Figure 3.30:** Hydrogen capacity is plotted against to the decomposition energy for  $M_1M_2(BH_4)_5(NH_3)_y$   $y=2,3,4,5,6$ . Representing colours: Li (Red), Na (Blue), K (Green).  $NH_3$  content:  $x=2$  (circle),  $x=3$  (triangle),  $x=4$  (square),  $x=5$  (diamond) and  $x=6$  (pentagon).

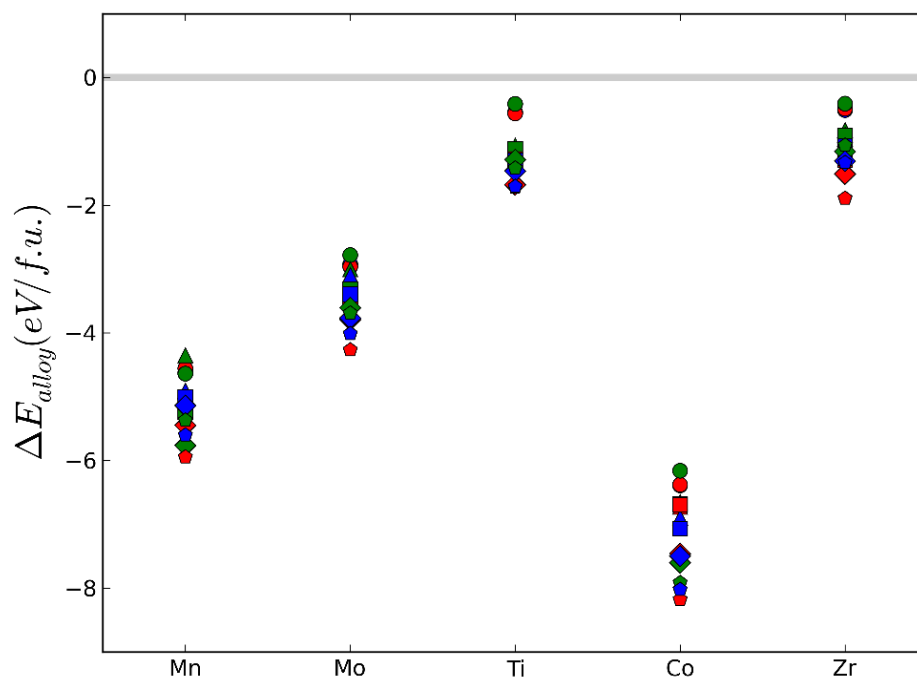


**Figure 3.31:** The alloying energies,  $\Delta E_{alloy}$ , are plotted against to  $M_2$  metal species for  $M_1M_2(BH_4)_5(NH_3)_y$   $y=2,3,4,5,6$ . Representing colours: Li (Red), Na (Blue), K (Green).  $NH_3$  content:  $x=2$  (circle),  $x=3$  (triangle),  $x=4$  (square),  $x=5$  (diamond) and  $x=6$  (pentagon).

compared to other complexes. In addition, for all complexes, the alloying energy decreases when  $NH_3$  content increases.

In figure 3.32, the average cation electronegativity versus decomposition energy is shown. All complexes except the ones containing Mn exhibit a linear trend.

### 3.2.3 Conclusions

The main purpose of this thesis is to find the most stable dual cation AMBs with a general formula of  $M_1M_2(BH_4)_x(NH_3)_y$ . The first step is the prediction of the crystal structures of dual cation AMBs. During this prediction process, reported crystal structure data in the literature were used. However, crystal structures of very limited number of AMBs are only known. The predicted crystal structures were used in the computational screening process and subsequently the most promising alloys were identified. The crystal structure prediction step was quite successful: for example the crystal structure of  $LiMg(BH_4)_3(NH_3)_2$ , which is experimentally known was

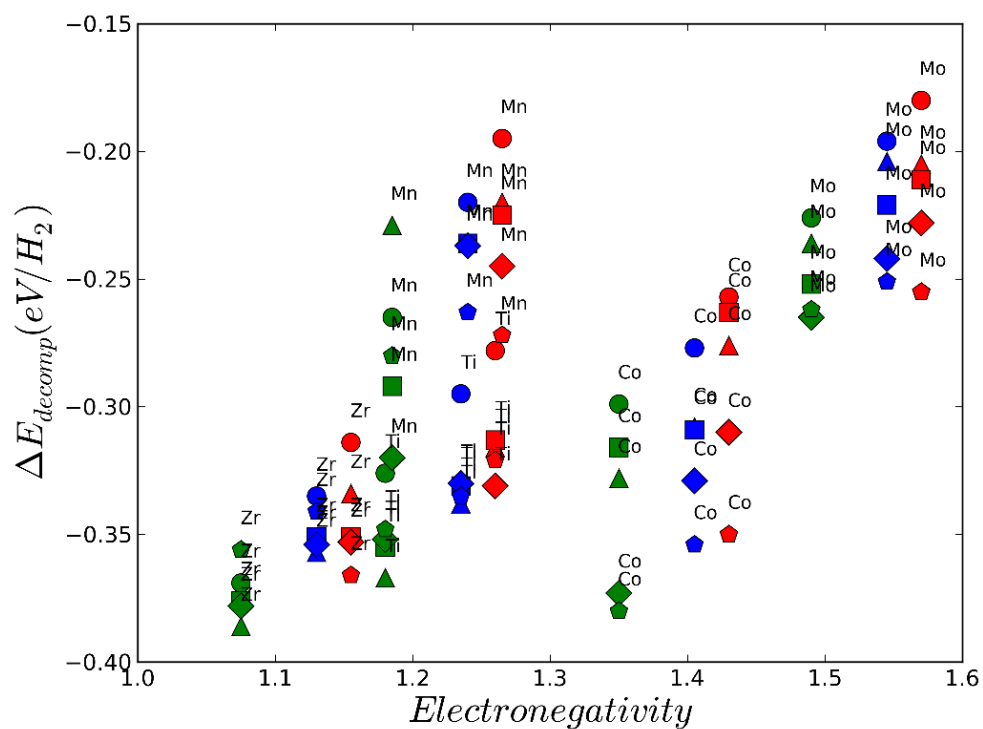


**Figure 3.32:** The decomposition energy,  $\Delta E_{decomp}$ , is plotted against to the average Pauling electronegativity of cations. Representing colours: Li (Red), Na (Blue), K (Green). NH<sub>3</sub> content: x=2 (circle), x=3 (triangle), x=4 (square), x=5 (diamond) and x=6 (pentagon).

reproduced. Even a new crystal structure was found which has lower in energy than the experimental one. The computational screening was carried out employing DFT. The evaluation of the screening was performed with the help of alloying and decomposition reactions reported in the literature. Among dual cation AMBs which are in the scope of this thesis, only  $\text{LiMg}(\text{BH}_4)_3(\text{NH}_3)_2$ ,  $\text{NaZn}(\text{BH}_4)_3(\text{NH}_3)_2$  and  $\text{LiSc}(\text{BH}_4)_4(\text{NH}_3)_4$  were experimentally synthesized. In the screening, these AMBs reside in the targeted region. For  $\text{M}_1\text{M}_2(\text{BH}_4)_3(\text{NH}_3)_y$  system, especially complexes containing Ni, Mg and Sr were found to be promising. In the case of  $\text{M}_1\text{M}_2(\text{BH}_4)_5(\text{NH}_3)_y$  system, almost all of the considered systems were placed in the targeted region. As a summary, after the screening, experimentally synthesized complexes were found to be appearing in the targeted area and many new AMBs which have not been synthesized yet were found to be promising. This ultimately opens new opportunities for the experimentalists.



## REFERENCES

- [1] Guo, Y., Jiang, Y., Xia, G. and Yu, X., 2012. Ammine aluminium borohydrides: an appealing system releasing over 12 wt % pure H<sub>2</sub> under moderate temperature, *Chemical communications*, **48**(37), 4408–10.
- [2] Sun, W.W., Chen, X.W., Gu, Q.F., Wallwork, K.S., Tan, Y.B., Tang, Z.W. and Yu, X.B., 2012. A New Ammine Dual-Cation (Li, Mg) Borohydride: Synthesis, Structure, and Dehydrogenation Enhancement, *Chem-Eur J*, **18**(22), 6825–6834.
- [3] Xia, G.L., Gu, Q.F., Guo, Y.H. and Yu, X.B., 2012. Ammine bimetallic (Na, Zn) borohydride for advanced chemical hydrogen storage, *J Mater Chem*, **22**(15), 7300–7307.
- [4] Guo, Y.H., Wu, H., Zhou, W. and Yu, X.B., 2011. Dehydrogenation Tuning of Ammine Borohydrides Using Double-Metal Cations, *Journal of the American Chemical Society*, **133**(13), 4690–4693.
- [5] Hummelshoj, J.S., Landis, D.D., Voss, J., Jiang, T., Tekin, A., Bork, N., Dulak, M., Mortensen, J.J., Adamska, L., Andersin, J., Baran, J.D., Barmparis, G.D., Bell, F., Bezanilla, A.L., Bjork, J., Bjorketun, M.E., Bleken, F., Buchter, F., Burkle, M., Burton, P.D., Buus, B.B., Calborean, A., Calle-Vallejo, F., Casolo, S., Chandler, B.D., Chi, D.H., Czekaj, I., Datta, S., Datye, A., DeLaRiva, A., Despoja, V., Dobrin, S., Engelund, M., Ferrighi, L., Frondelius, P., Fu, Q., Fuentes, A., Furst, J., Garcia-Fuente, A., Gavnholt, J., Goeke, R., Gudmundsdottir, S., Hammond, K.D., Hansen, H.A., Hibbitts, D., Hobi, E.J., Howalt, J.G., Hruby, S.L., Huth, A., Isaeva, L., Jelic, J., Jensen, I.J., Kacprzak, K.A., Kelkkanen, A., Kelsey, D., Kesanakurthi, D.S., Kleis, J., Klupfel, P.J., Konstantinov, I., Korytar, R., Koskinen, P., Krishna, C., Kunkes, E., Larsen, A.H., Lastra, J.M., Lin, H., Lopez-Acevedo, O., Mantega, M., Martinez, J.I., Mesa, I.N., Mowbray, D.J., Myrdal, J.S., Natanzon, Y., Nistor, A., Olsen, T., Park, H., Pedroza, L.S., Petzold, V., Plaisance, C., Rasmussen, J.A., Ren, H., Rizzi, M., Ronco, A.S., Rostgaard, C., Saadi, S., Salguero, L.A., Santos, E.J., Schoenhalz, A.L., Shen, J., Smedemand, M., Stausholm-Moller, O.J., Stibius, M., Strange, M., Su, H.B., Temel, B., Toftelund, A., Tripkovic, V., Vanin, M., Viswanathan, V., Vojvodic, A., Wang, S., Wellendorff, J., Thygesen, K.S., Rossmeisl, J., Bligaard, T., Jacobsen, K.W., Norskov, J.K. and Vegge, T., 2009. Density functional theory based screening of ternary alkali-transition metal borohydrides: a computational material design project, *The Journal of chemical physics*, **131**(1), 014101.

- [6] Tekin, A., Hummelshoj, J.S., Jacobsen, H.S., Sveinbjornsson, D., Blanchard, D., Norskov, J.K. and Vegge, T., 2010. Ammonia dynamics in magnesium ammine from DFT and neutron scattering, *Energy and Environmental Science*, (4), 448–456.
- [7] Churchard, A.J., Banach, E., Borgschulte, A., Caputo, R., Chen, J.C., Clary, D., Fijalkowski, K. J. and Geerlings, H., Genova, R.V., Grochala, W., Jaron, T., Juanes-Marcos, J.C., Kasemo, B., Kroes, G. J. and Ljubic, I., Naujoks, N., Norskov, J.K., Olsen, R.A., Pendolino, F., Remhof, A., Romaszki, L., Tekin, A., Vegge, T., Zach, M. and Zuttel, A., 2011. A multifaceted approach to hydrogen storage, *Physical chemistry chemical physics : PCCP*, (13), 16955–16972.
- [8] Caputo, R., Tekin, A., Sikora, W. and Zuttel, A., 2009. First-principles determination of the ground-state structure of Mg(BH<sub>4</sub>)(2), *Chemical Physics Letters*, **480(4-6)**, 203–209.
- [9] Tekin, A., Caputo, R. and Zuttel, A., 2010. First-principles determination of the ground-state structure of LiBH<sub>4</sub>, *Physical Review Letters*, **104(21)**, 215501.
- [10] Caputo, R. and Tekin, A., 2011. Ab-initio crystal structure prediction. A case study: NaBH<sub>4</sub>, *J. Solid State Chem.*, **184(7)**, 1622–1630.
- [11] Caputo, R. and Tekin, A., 2012. Lithium dihydroborate: first-principles structure prediction of LiBH<sub>2</sub>, *Inorg. Chem.*, **51(18)**, 9757–9765.
- [12] Andreasen, A., Sorensen, M.B., Burkarl, R., Moller, B., Molenbroek, A.M., Pedersen, A.S., Vegge, T. and Jensen, T.R., 2006. Dehydrogenation kinetics of air-exposed MgH<sub>2</sub>/Mg<sub>2</sub>Cu and MgH<sub>2</sub>/MgCu<sub>2</sub> studied with in situ X-ray powder diffraction, *Applied Physics A*, **82(3)**, 515–521.
- [13] Lee, S.L. and Lee, Y.H., 2000. Hydrogen storage in single-walled carbon nanotubes, *Appl. Phys. Lett.*, **76**, 2887.
- [14] Liu, Y., Kabbour, H., Brown, C.M., Neumann, D.A. and Ahn, C.C., 2008. Increasing the Density of Adsorbed Hydrogen with Coordinatively Unsaturated Metal Centers in Metal-Organic Frameworks, *Langmuir*, **24(9)**, 4772–4777.
- [15] Rude, L.H., Nielsen, T.K., Ravnsbaek, D.B., Bosenberg, U., Ley, M.B., Richter, B., Arnbjerg, L.M., Dornheim, M., Filinchuk, Y., Besenbacher, F. and Jensen, T.R., 2011. Tailoring properties of borohydrides for hydrogen storage: A review, *physica status solidi (a)*, **208(8)**, 1754–1773.
- [16] Feaver, A., Sepehri, S., Shamberger, P., Stowe, A., Autrey, T. and Cao, G., 2007. Coherent carbon cryogel-ammonia borane nanocomposites for H<sub>2</sub> storage, *The journal of physical chemistry. B*, **111(26)**, 7469–72.
- [17] Lohstroh, W. and Fichtner, M., 2007. Reaction steps in the Li-Mg-N-H hydrogen storage system, *J Alloy Compd*, **446**, 332–335.

- [18] **Url-1**, "[http://www1.eere.energy.gov/hydrogenandfuelcells/pdfs/freedomcar\\_targets\\_explanations.pdf](http://www1.eere.energy.gov/hydrogenandfuelcells/pdfs/freedomcar_targets_explanations.pdf)", 30.04.2015.
- [19] **Caputo, R., Tekin, A., Sikora, W. and Zuttel, A.**, 2009. First-principles determination of the ground-state structure of  $\text{Mg}(\text{BH}_4)_2$ , *Chem Phys Lett*, **480(4-6)**, 203–209.
- [20] **Tekin, A., Caputo, R. and Zuttel, A.**, 2010. First-principles determination of the ground-state structure of  $\text{LiBH}_4$ , *Physical review letters*, **104(21)**, 215501.
- [21] **Caputo, R. and Tekin, A.**, 2011. Ab-initio crystal structure prediction. A case study:  $\text{NaBH}_4$ , *J Solid State Chem*, **184(7)**, 1622–1630.
- [22] **Caputo, R. and Tekin, A.**, 2012. Lithium dihydroborate: first-principles structure prediction of  $\text{LiBH}_2$ , *Inorg. Chem.*, **51(18)**, 9757–65.
- [23] **Caputo, R., Kupczak, A., Sikora, W. and Tekin, A.**, 2013. Ab initio crystal structure prediction by combining symmetry analysis representations and total energy calculations. An insight into the structure of  $\text{Mg}(\text{BH}_4)_2$ , *Physical Chemistry Chemical Physics*, **15(5)**, 1471–1480.
- [24] **Tekin, A., Hummelshoj, J.S., Jacobsen, H.S., Sveinbjornsson, D., Blanchard, D., Norskov, J.K. and Vegge, T.**, 2010. Ammonia dynamics in magnesium ammine from DFT and neutron scattering, *Energ. Environ. Sci.*, **3(4)**, 448–456.
- [25] **Churchard, A.J., Banach, E., Borgschulte, A., Caputo, R., Chen, J.C., Clary, D., Fijalkowski, K.J., Geerlings, H., Genova, R.V., Grochala, W., Jaron, T., Juanes-Marcos, J.C., Kasemo, B., Kroes, G.J., Ljubic, I., Naujoks, N., Norskov, J.K., Olsen, R.A., Pendolino, F., Remhof, A., Romaszki, L., Tekin, A., Vegge, T., Zach, M. and Zuttel, A.**, 2011. A multifaceted approach to hydrogen storage, *Physical chemistry chemical physics : PCCP*, **13(38)**, 16955–72.
- [26] **Soloveichik, G., Her, J.H., Stephens, P.W., Gao, Y., Rijssenbeek, J., Andrus, M. and Zhao, J.C.**, 2008. Ammine magnesium borohydride complex as a new material for hydrogen storage: Structure and properties of  $\text{Mg}(\text{BH}_4)_2 \cdot 2\text{NH}_3$ , *Inorganic Chemistry*, **47(10)**, 4290–4298.
- [27] **Yang, Y., Liu, Y., Wu, H., Zhou, W., Gao, M. and Pan, H.**, 2014. An ammonia-stabilized mixed-cation borohydride: synthesis, structure and thermal decomposition behavior, *Physical chemistry chemical physics : PCCP*, **16(1)**, 135–43.
- [28] **Nickels, E.A., Jones, M.O., David, W.I., Johnson, S.R., Lowton, R.L., Sommariva, M. and Edwards, P.P.**, 2008. Tuning the decomposition temperature in complex hydrides: synthesis of a mixed alkali metal borohydride, *Angewandte Chemie*, **47(15)**, 2817–9.

- [29] Nakamori, Y., Miwa, K., Ninomiya, A., Li, H.W., Ohba, N., Towata, S.I., Zuttel, A. and Orimo, S.I., 2006. Correlation between thermodynamical stabilities of metal borohydrides and cation electronegativities: First-principles calculations and experiments, *Phys Rev B*, **74**(4).
- [30] Gratzel, M., 2001. Photoelectrochemical cells, *Nature*, **414**(6861), 338–44.
- [31] 2007, British Petroleum statistical review of world energy.
- [32] Christensen, C.H., Sorensen, R.Z., Johannessen, T., Quaade, U.J., Honkala, K., Elmoe, T.D., Kohler, R. and Norskov, J.K., 2005. Metal ammine complexes for hydrogen storage, *J Mater Chem*, **15**(38), 4106–4108.
- [33] Sorensen, R.Z., Hummelshoj, J.S., Klerke, A., Reves, J.B., Vegge, T., Norskov, J.K. and Christensen, C.H., 2008. Indirect, reversible high-density hydrogen storage in compact metal ammine salts, *Journal of the American Chemical Society*, **130**(27), 8660–8.
- [34] Klerke, A., Christensen, C.H., Norskov, J.K. and Vegge, T., 2008. Ammonia for hydrogen storage: challenges and opportunities, *J Mater Chem*, **18**(20), 2304–2310.
- [35] Zuttel, A., Rentsch, S., Fischer, P., Wenger, P., Sudan, P., Mauron, P. and Emmenegger, C., 2003. Hydrogen storage properties of LiBH<sub>4</sub>, *J Alloy Compd*, **356**, 515–520.
- [36] Chlopek, K., Frommen, C., Leon, A., Zabara, O. and Fichtner, M., 2007. Synthesis and properties of magnesium tetrahydroborate, Mg(BH<sub>4</sub>)<sub>2</sub>, *J Mater Chem*, **17**(33), 3496–3503.
- [37] Hagemann, H., Longhini, M., Kaminski, J.W., Wesolowski, T.A., Cerny, R., Penin, N., Sorby, M.H., Hauback, B.C., Severa, G. and Jensen, C.M., 2008. LiSc(BH<sub>4</sub>)<sub>4</sub>: a novel salt of Li<sup>+</sup> and discrete Sc(BH<sub>4</sub>)<sub>4</sub><sup>-</sup> complex anions, *The journal of physical chemistry A*, **112**(33), 7551–5.
- [38] Chu, H.L., Wu, G.T., Xiong, Z.T., Guo, J.P., He, T. and Chen, P., 2010. Structure and Hydrogen Storage Properties of Calcium Borohydride Diammoniate, *Chem Mater*, **22**(21), 6021–6028.
- [39] Yuan, F., Gu, Q.F., Guo, Y.H., Sun, W.W., Chen, X.W. and Yu, X.B., 2012. Structure and hydrogen storage properties of the first rare-earth metal borohydride ammoniate: Y(BH<sub>4</sub>)<sub>3</sub> · 4NH<sub>3</sub>, *J Mater Chem*, **22**(3), 1061–1068.
- [40] Perdew, J.P., Burke, K. and Ernzerhof, M., 1997. Generalized Gradient Approximation Made Simple, *Phys. Rev. Lett.*, **78**(7), 1396.
- [41] Hohenberg, P. and Kohn, W., 1964. Inhomogeneous electron gas, *Phys. Rev.*, **136**, B864–71.
- [42] Kohn, W. and Sham, L.J., 1965. Self-consistent equations including exchange and correlation effects, *Phys. Rev.*, **140**, A1133.

- [43] **Jones, R.O. and Gunnarsson, O.**, 1989. The density functional formalism, its applications and prospects, *Rev. Mod. Phys.*, **61**, 689–746.
- [44] **Thijssen, J.**, 2007. Computational Physics, Cambridge University Press.
- [45] **Langreth, D.C. and Mehl, M.J.**, 1981. Easily implementable nonlocal exchange-correlation energy functional, *Phys. Rev. Lett.*, **47**, 446–50.
- [46] **Perdew, J.P. and Zunger, A.**, 1981. Self-interaction correction to density-functional approximations for many-electron systems, *Phys. Rev. B*, **23**, 5048–79.
- [47] **Slater, J.C.**, 1982. Quantum Theory of Molecules and Solids, McGraw-Hill.
- [48] **Ceperley, D.M.**, 1978. Ground state of the fermion one-component plasma – a Monte Carlo study in two and three dimensions, *Phys. Rev. B*, **18**, 3126–38.
- [49] **Barth, U. and Hedin, L.**, 1972. A local exchange-correlation potential for the spin-polarized case, *J. Phys. C*, **5**, 1629–42.
- [50] **Gunnarsson, O. and Lundqvist, B.I.**, 1976. Exchange and correlation in atoms, molecules and solids by the spin-density-functional formalism, *Phys. Rev. B*, **13**, 4274–98.
- [51] **Perdew, J.P. and Wang, Y.**, 1986. Accurate and simple density functional for the electronic exchange energy: Generalized gradient approximation, *Phys. Rev. B*, **33**, 8800–2.
- [52] **Perdew, J.P.**, 1986. Density-functional approximation for the correlation energy of the inhomogeneous electron gas, *Phys. Rev. B*, **33**, 8822–4.
- [53] **Wang, Y. and Perdew, J.P.**, 1991. Correlation hole of the spin-polarized electron gas, with exact small-wave-vector and high-density scaling, *Phys. Rev. B*, **44**, 13298–307.
- [54] **Becke, A.D.**, 1988. Density functional exchange energy approximation with correct asymptotic behaviour, *Phys. Rev. A*, **38**, 3098–100.
- [55] **Lee, C., Yang, W. and Parr, R.G.**, 1988. Development of the Colle–Salvetti correlation-energy formula into a functional of the electron density, *Phys. Rev. B*, **37**, 785–9.
- [56] **Perdew, J.P., Burke, K. and Enzerhof, M.**, 1996. Generalized gradient approximation made simple, *Phys. Rev. Lett.*, **77**, 3865–86.
- [57] **Perdew, J.P., Burke, K. and Enzerhof, M.**, 1997. Generalized gradient approximation made simple (Erratum), *Phys. Rev. Lett.*, **78**, 1396.
- [58] **Desiraju, G.R.**, 2002. *Nature Materials*, **1**, 77–79.
- [59] **Woodley, S.M. and Catlow, R.**, 2008. *Nature Materials*, **7**, 937 – 946.

- [60] **Oganova, A.R. and Glass, C.W.**, 2006. Crystal structure prediction using ab initio evolutionary techniques: Principles and applications, *THE JOURNAL OF CHEMICAL PHYSICS*, **124**, 244704.
- [61] **Url-2**, "<http://uspex.stonybrook.edu/uspex.html>", 11.05.2015.
- [62] **Wang, Y., Lv, J., Zhu, L. and Ma, Y.**, 2012. CALYPSO: A method for crystal structure prediction, *Computer Physics Communications*, **183(10)**, 2063–2070.
- [63] **Lonie, D.C. and Zurek, E.**, 2011. XtalOpt: An Open-Source Evolutionary Algorithm for Crystal Structure Prediction, *Computer Physics Communications*, **182**, 372–387.
- [64] **Url-3**, "<http://gasp.mse.ufl.edu/>", 11.05.2015.
- [65] **Henderson, D.H., Jacobson, S.H. and Johnson, A.W.**, 2003. The Theory and Practice of Simulated Annealing, *Handbook of Metaheuristics*, **57**, 287–319.
- [66] **Chen, X.W. and Yu, X.B.**, 2012. Electronic Structure and Initial Dehydrogenation Mechanism of  $M(\text{BH}_4)_2 \cdot 2\text{NH}_3$  ( $M = \text{Mg}, \text{Ca}, \text{and Zn}$ ): A First-Principles Investigation, *J Phys Chem C*, **116(22)**, 11900–11906.
- [67] **Miwa, K., Aoki, M., Noritake, T., Ohba, N., Nakamori, Y., Towata, S., Zuttel, A. and Orimo, S.**, 2006. Thermodynamical stability of calcium borohydride  $\text{Ca}(\text{BH}_4)_2$ , *Phys Rev B*, **74(15)**.
- [68] **Ravnsbaek, D.B., Nickels, E.A., Cerny, R., Olesen, C.H., David, W.I., Edwards, P.P., Filinchuk, Y. and Jensen, T.R.**, 2013. Novel alkali earth borohydride  $\text{Sr}(\text{BH}_4)_2$  and borohydride-chloride  $\text{Sr}(\text{BH}_4)\text{Cl}$ , *Inorg Chem*, **52(19)**, 10877–85.
- [69] **Huan, T.D., Amsler, M., Tuoc, V.N., Willand, A. and Goedecker, S.**, 2012. Low-energy structures of zinc borohydride  $\text{Zn}(\text{BH}_4)_2$ , *Phys Rev B*, **86(22)**.
- [70] **Cerny, R., Penin, N., Hagemann, H. and Filinchuk, Y.**, 2009. The First Crystallographic and Spectroscopic Characterization of a 3d-Metal Borohydride:  $\text{Mn}(\text{BH}_4)_2$ , *J. Phys. Chem. C*, **113(20)**, 9003–9007.
- [71] **Kurakevych, O.O. and Solozhenko, V.L.**, 2007. Rhombohedral boron subnitride,  $\text{B}_3\text{N}_2$ , by X-ray powder diffraction, *Acta crystallographica. Section C, Crystal structure communications*, **63(Pt 9)**, i80–2.
- [72] **Miwa, K., Ohba, N., Towata, S., Nakamori, Y., Zuttel, A. and Orimo, S.**, 2007. First-principles study on thermodynamical stability of metal borohydrides: Aluminum borohydride  $\text{Al}(\text{BH}_4)_3$ , *J Alloy Compd*, **446**, 310–314.

- [73] **Kim, C., Hwang, S.J., Bowman, R.C., Reiter, J.W., Zan, J.A., Kulleck, J.G., Kabbour, H., Majzoub, E.H. and Ozolins, V.**, 2009. LiSc(BH<sub>4</sub>)(4) as a Hydrogen Storage Material: Multinuclear High-Resolution Solid-State NMR and First-Principles Density Functional Theory Studies, *J Phys Chem C*, **113(22)**, 9956–9968.
- [74] **Rude, L.H., Corno, M., Ugliengo, P., Baricco, M., Lee, Y.S., Cho, Y.W., Besenbacher, F., Overgaard, J. and Jensen, T.R.**, 2012. Synthesis and Structural Investigation of Zr(BH<sub>4</sub>)(4), *J Phys Chem C*, **116(38)**, 20239–20245.
- [75] **Gu, Q.F., Gao, L., Guo, Y.H., Tan, Y.B., Tang, Z.W., Wallwork, K.S., Zhang, F.W. and Yu, X.B.**, 2012. Structure and decomposition of zinc borohydride ammonia adduct: towards a pure hydrogen release, *Energ Environ Sci*, **5(6)**, 7590–7600.





## CURRICULUM VITAE



**Name Surname:** Yusuf Kışlak

**Place and Date of Birth:** İstanbul, 15-11-1984

**E-Mail:** yusufkislak@gmail.com

**B.Sc.:** Physics Engineering, Istanbul Technical University

**M.Sc.:** Computational Science and Engineering, Istanbul Technical University

### List of Publications and Patents:

Şaziye Uğur, Atilla K. Dinç , **Yusuf Kışlak**, Effect of molecular weight on the dissolution properties of polystyrene latex films. *Journal Of Polymer Research*, Volume: 19, Issue: 9, Page: 1-10, 2012.

Şaziye Uğur, **Yusuf Kışlak**, Film Formation From PS/AL<sub>2</sub>O<sub>3</sub> Nanocomposites Prepared by Dip-Drawing Method, *Polymer Composites* , Volume 33 Issue 8, pages 1274-1287, August 2012

### PUBLICATIONS/PRESENTATIONS ON THE THESIS

- **Kışlak Y.**, Tekin A.: First-principles Structure Prediction Of Ammine Dual Cation Borohydrides:  $\text{LiTi}(\text{BH}_4)_3(\text{NH}_3)_x$  *International Congress on Energy Efficiency and Energy Related Materials*, October 9-12, 2013 Antalya, Turkey.
- **Kışlak Y.**, Tekin A.: Computational Design of Dual Cation Ammine Metal Borohydrides:  $\text{LiTi}(\text{BH}_4)_5(\text{NH}_3)_x$  *International Congress on Energy Efficiency and Energy Related Materials*, October 16-19, 2014 Muğla, Turkey.
- **Kışlak Y.**, Tekin A.: Computational Screening of Dual Cation Ammine Metal Borohydrides *The Energy & Materials Research Conference*, February 25-27, 2015 Madrid, Spain.